MILLIMETER AND SUBMILLIMETER-WAVE INTEGRATED HORN ANTENNA SCHOTTKY RECEIVERS

WALID YOUSSEF ALI-AHMAD

1993

MILLIMETER AND SUBMILLIMETER-WAVE INTEGRATED HORN ANTENNA SCHOTTKY RECEIVERS

by

Walid Youssef Ali-Ahmad

A dissertation submitted in partial fulfillment
of the requirements for the degree of
Doctor of Philosophy
(Electrical Engineering)
in The University of Michigan
1993

Doctoral Committee:

Associate Professor Gabriel M. Rebeiz, Chairperson
Associate Professor Joel N. Bregman
Research Scientist Jack R. East
Associate Professor Linda P.B. Katehi
Professor Fawwaz T. Ulaby
Associate Professor Andrew E. Yagle

To a village in southern Lebanon
where grapevines are sweet and generous,
where houses embrace the mountain,
and where a village proud of its people
looks forward to a better day ...

To a city which wore a dress of sadness
for a father who never came back home
and for brothers intoxicated with metal and fire,
To a city dreaming of its new dress
sewn with peace and love
by people with pride and faith
by people who know
that the alphabet is stronger than the bullet

To my father's village, Roum,
and to my mother's city, Beirut,
I dedicate this work

ACKNOWLEDGEMENTS

"If he is indeed wise he does not bid you enter the house of his wisdom, but rather leads you to the threshold of your mind."

The prophet, Gibran Khalil Gibran

I dedicate these words to my advisor Prof. Gabriel Rebeiz to express my deep appreciation for his technical advices during the course of the Ph. D. and for the challenges that he faced me with, in order to teach me the essence of doing research. I sincerely thank him for his patience and tolerance with me and for his continuous encouragement throughout my graduate studies. Our close friendship has been very important to me because he was always there to help me with personal and professional matters, and even to listen to my sorrows! I am very grateful for the financial support he obtained through the NASA/Center for Space Terahertz Technology during the past four years.

I am indebted to Prof. Fawwaz T. Ulaby, who gave me the opportunity to come to the University of Michigan to work in one of the best research graduate schools in the nation. I will always remember his repeated words "Keep up the good work!" and I highly appreciate his advice throughout my graduate years. Furthermore, I would like to express my sincere gratitude to Prof. Linda Katehi for her confidence in me, her continuous support, and her friendship during the past four years. I would like to extend my sincere thanks to Dr. Jack East, Prof. Joel Bregman, and Prof. Andrew Yagle for being part of my thesis committee, for their patience, and for their advice

that was essential for making this work complete.

I would like to acknowledge Prof. Paul Goldsmith at Cornell University, Dr. Anthony Kerr at NRAO, and Dr. Neal Erickson at Millitech Corp. for their technical advice related to my research work. I am very thankful to Mr. Bill Bishop and Dr. Tom Crowe at the University of Virginia for providing us with the planar GaAs Scottky diodes. I also thank the NRAO staff for their help in the 335GHz receiver measurements set-up. My deep and sincere respect and gratitude to Dr. Omar Mardam Bey are not enough for his continuous guidance, support, and dear friendship since my junior year in college.

The work in this thesis has been strengthened by the theory that Dr. George Eleftheriades developed for the integrated horn antenna. My close work with George and the understanding that we have between us made our research better and our friendship stronger. I am deeply grateful for his confidence in me and his encouragements as a big brother in difficult times.

My first two years in the United States would not have been easy without the help of my friend and colleague Steven Gearhart, who was patient in teaching me about American culture and helping me to adapt to it. I am also grateful to my colleagues Dr. Curtis Ling and Brian Kormanyos for their technical help, for their friendship, and for their patience with me. In addition, I would like to thank all the members of Prof. Rebeiz's and Prof. Katehi's groups for their help and all the good moments we had together inside and outside the laboratory. I extend my thanks to all the Radiation Laboratory faculty, staff, and students for making the work environment enjoyable and educational. I am grateful for the friendships of Leo Kempel, Dr. Nihad Dib, Adib Nashashibi, and Prof. Emilie Van Deventer.

The warm social environment in Ann Arbor introduced me to many interesting

people, whom I loved and who influenced me and gave a balance to my life. It is hard to acknowledge all these people that are dear to my heart, and I ask forgiveness from the friends whose names have not been mentioned. My last two years at the University of Michigan exposed me like never before to the Greek culture. I made many Greek friends who are dear to my heart, and learning about each other's culture has been a wonderful experience. The dear friendship of Apostolos Samelis made my last two years in graduate school easier. I will always remember the *laughs* and *regrets* that I shared with Apostolos, and the many *philosophical* discussions that we had. I am deeply grateful for the patience and dear friendship of Ms. Christina Chilimigras which gave a nice flavor to my life and broadened my outlook on life. I am also grateful for the friendship and trust of Angelos Alexanian and Gildas Gauthier. The joyful companionship of Dimitris Pandelis and the support and care of Nikos Kazantzis made difficult moments easier.

These acknowledgements are not addressed by myself only, but also, by my parents who are sharing with me my joy and my gratitude to all my friends and all the people who helped me. I thank God for blessing me with two parents who dedicated their lives to the education and happiness of their children. What I have achieved after all these years would not have been real without the encouragement and love of my father, and without the ethics and the discipline that he taught me. The care and affection of my mother who made the health and the education of her children a priority in her life taught me the meaning of sacrifice and love. What I have achieved now is only part of my obligation towards them, and may God help me to fulfill the rest. My joy can not be complete without expressing all my love to my brother Wissam and my sister Noha. I wish them all the luck and success in their educations so that they can reach their ambitions in this life and be proud of their own achievements.

PREFACE

This thesis deals with the design and performance of millimeter and submillimeter-wave integrated horn antenna Schottky receivers at room temperature. The design and performance of a dual-polarized integrated horn antennas imaging array for millimeter-wave applications is also included.

TABLE OF CONTENTS

LIST OF FIGURES

Figure

LIST OF TABLES

LIST OF APPENDICES

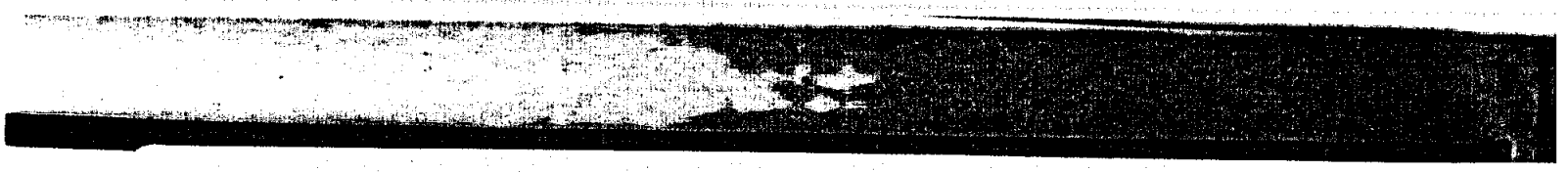

CHAPTER I

INTRODUCTION

Millimeter-wave systems spanning the frequency range from 30GHz to 300GHz are attractive for many reasons. Compared to lower-frequency microwave systems, millimeter-wave systems have better spatial resolution due to the small λ used, better immunity to interference, and increased sensitivity to Doppler velocity effects. The large bandwidths available at the corresponding millimeter-waves transmission windows result in the fact that GHz bandwidths can be accommodated at any particular millimeter-wave atmospheric window. Compared to optical systems, millimeter-wave systems have a better atmospheric propagation through fog, clouds, smoke, and dust in their transmission windows, and offer a technology more feasible for frequency multiplexing. Millimeter-wave systems have been used in many scientific and military applications such in remote sensing, radioastronomy, communication systems, imaging arrays, and missiles tracking radars [1, 2, 3, 4, 5, 6]. Millimeter-wave systems are now being introduced into the commercial market through applications such as anti-collision radars [7] and Intelligent-Vehicle-Highway-Systems (IVHS) [8].

During the past two-decades, scientists have exploited the near-millimeter wave frequency range (wavelength ranges from 3mm to 300μm) for remote sensing and radio-astronomical applications [1, 9]. Hence, the development of heterodyne receivers

with improved sensitivity has been necessary for a wide range of applications in radio astronomy, plasma physics, frequency standards, spectroscopy, and satellite-based radiometry. These low-noise heterodyne receivers use GaAs Schottky Barrier diodes or superconducting tunnel-junctions (SIS) as the non-linear elements. In figure 1.1, the basic configuration for a heterodyne receiver operating in the near-millimeter wave region is shown.

The loss encountered in waveguide structures at near-millimeter wavelengths has pushed the development of *quasi-optical* structures for guiding the wave through free-space and coupling it to the receiver antenna [10, 11]. The circuit functions, performed before by waveguides in a microwave or a millimeter-wave system, are performed now through the aid of quasi-optical elements with beam diameters which are not many orders of magnitude greater than the operating wavelength as in the optical regime. In figure 1.1, the LO and RF signal beams are combined using a quasi-optical diplexer. The combined beam is coupled to the antenna-mixer block via a dielectric lens. The IF signal is amplified through a low-noise IF chain. The most important element in determining the receiver performance is the antenna-mixer configuration. The most widely used antenna-mixer configuration, discussed in section 1.1, is a waveguide feed horn feeding into a waveguide mixer structure. This thesis deals with the design, development, and performance of a new antenna-mixer configuration that falls in the category of quasi-optical mixers that incorporate planar integrated antenna structures with hybrid planar mixer circuits.

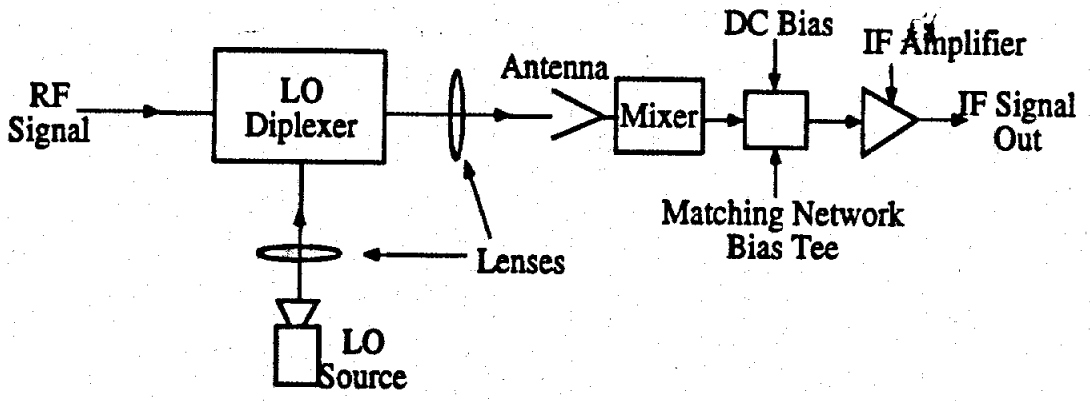

Figure 1.1: The basic configuration for a heterodyne receiver operating in the near-millimeter wave region.

1.1 Waveguide Receivers for the Near-Millimeter Wave Frequency Range

1.1.1 GaAs Schottky Diode Mixers

Fig. 1.2 shows the most common single-ended mixer mount structure [12, 13]. Scalar or corrugated horns [14], dual-mode horns [15], pyramidal and conical feed horns [16] are used to couple the input RF and LO powers into the mixer structure. The diode is mounted inside a reduced-height waveguide, typically one-fourth of the nominal value, resulting in desirable RF and IF impedance levels over a wide frequency range. A quarter-wave step transformer or taper transition is normally used to connect the reduced-height waveguide to the input guide. The RF choke, either a coaxial structure [17] or a dielectric microstrip line [18], is used to pass the IF signal and the dc bias to the diode and to present a reactive termination to the RF frequency at the waveguide wall for optimum mixer performance. The operation

of waveguide mixers is limited to 600GHz because above this frequency, single-mode metalic-guided wave structures become very difficult to fabricate and exhibit high loss. Corrugated horns with highly rotational symmetric patterns are difficult to be built above 350GHz due to the complexity of their mechanical designs. Dual-mode horns with high Gaussian coupling efficiency can be built up to 600GHz. Simple pyramidal or conical horns have been used at frequencies higher than 600GHz [19], but they suffer from high sidelobe levels and a distinctly non-symmetric radiation pattern, resulting in poor Gaussian coupling to quasi-optical systems.

The dot-matrix chip GaAs Schottky diode has been mostly used in waveguide mixer structures and has consistently achieved the best performance of any mixer diode, because of its small series resistance and junction capacitance, and its negligible parasitic capacitance. A single anode "dot" on the chip is contacted by a small diameter contact wire ("whisker"), and the backside of the chip which represents the cathode is soldered to an appropriate mounting surface. The whisker wire shape and dimensions and the position of an adjustable tuning short in the reduced-height waveguide are used to control the embedding impedance seen by the diode at the LO frequency and the RF sidebands. The optimization of the doping and thickness of the diode epilayer and the optimization of the mixer mount have a big effect on lowering the mixer noise temperature.

For high frequency applications, work has been done on fabricating diodes with small anode diameter and on reducing the skin effect resistance between the Schottky and ohmic contacts [20]. A considerable improvement in the receiver noise temperature is obtained by cooling the diodes to cryogenic temperatures. DSB waveguide receivers noise temperatures as low as 62K at 100GHz and as low as 330K at 230GHz have been obtained at cryogenic temperatures [21, 12].

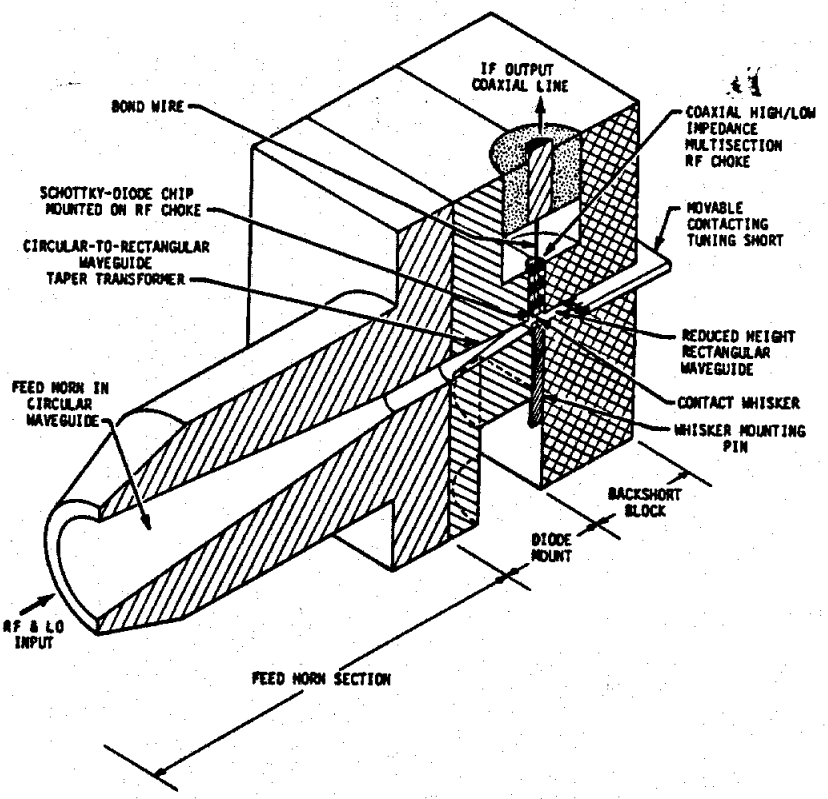

Figure 1.2: A typical waveguide receiver mixer mount operating below 600GHz.

One of the main disadvantages of the dot-matrix diode is the difficulty of achieving a mechanically reliable whisker contact. Also, whisker-contacted diodes require reduced-height waveguide mounts which are difficult to machine and are not well suited for space applications. To solve this problem, a variety of planar beam-lead diode designs have been investigated. In these beam-lead diodes, the whisker is replaced by a planar finger contact. This results in a reliable and strong diode structure, but suffers from high parasitic capacitance which deteriorates the mixer performance in the near-millimeter frequency range. Many designs have been developed for low-parasitic planar diodes such as the low-parasitic beam-lead diodes [22, 23, 24] and the "surface channel" planar diode. The surface channel diode proved to be a very promising structure for millimeter and submillimeter-wave applications [25, 26, 27].

As a result of planar diodes development, a new line of waveguide mixers have

been designed and implemented, including single-ended, subharmonically pumped, and balanced mixers, using fin-line, microstrip line, and suspended substrate strip-line technology [27, 28, 29, 30]. In these designs, planar diodes are mounted on a suspended strip-line or on a microstrip line structures which separates IF, LO and RF signals. The LO and RF signals are coupled from *full-height* waveguide to the strip-line or the microstrip line circuit via tunable probe-type transitions. These types of waveguide mixers employing planar diodes have showed compatible performance with whisker-contacted diode waveguide mixers for room temperature applications [28, 26].

1.1.2 SIS Mixers

An alternative mixer element is the SIS superconducting tunnel junction [31, 32]. The SIS mixer is the most sensitive detector in the millimeter-wave region. The quantum limit for noise temperature (in a SSB mixer) has essentially been reached at 100GHz [33]. This is a result of the extremely low shot noise, potential conversion gain and low local oscillator power requirements of SIS mixers. Waveguide mounts, similar to those used for Schottky-diode mixers, have been used for SIS mixers. The frequency operation of SIS mixers is limited by the superconducting energy gap of the material. Current SIS waveguide receivers are used at frequencies up to 700GHz [34, 35, 36, 37, 38, 39]. Even though SIS devices are relatively stable and thermally recyclable device, they must be cooled to 4-8°K. They are also electrically fragile and the mixers incorporating these devices are not as rugged or reliable as those using state-of-the-art planar Schottky diodes.

1.2 Quasi-Optical Receivers for the Near-Millimeter Wave Frequency Range

As discussed in the previous section, fundamental-mode waveguide mounts are difficult to fabricate above 600GHz and exhibit high loss above 600GHz. The most widely used open structure antenna in submillimeter-wave heterodyne receivers is the corner-cube antenna (Fig. 1.3) [40, 41]. In this mixer mount, the diode contact whisker is used also as a traveling-wave antenna. A narrow high-gain beam is produced by placing a corner reflector behind the wire. The disadvantage of the corner-cube antenna is that it has a low Gaussian coupling efficiency (around 40-50%) because of its relatively high side lobes and cross-polarization levels. Receivers employing the corner-cube antenna structure are the only receivers available now above 1THz [42].

The disadvantage of waveguide-based millimeter- and submillimeter-wave systems is the considerable cost of machining them. Applications, such as imaging arrays and collision-avoidance radars, which require a volume production base, would be very expensive to develop using precision-machined waveguides. Also, as discussed previously, waveguide-based receivers are very difficult to fabricate above 600GHz. It is clear that the suggested millimeter- and submillimeter-wave applications requiring a volume production base, low cost, optimized electrical performance, subminiature packaging, and minimal dc power consumption necessitates the development of a new generation of RF components and systems, one primarly based on advanced integrated-circuit techniques. Hence, integrated receivers are easier to manufacture and to assemble, and more reliable than waveguide receivers. The integration techniques allow a tremendous size and weight reduction of linear or two-dimensional arrays of receivers. Integrated receivers can be precisely controlled with enhanced-

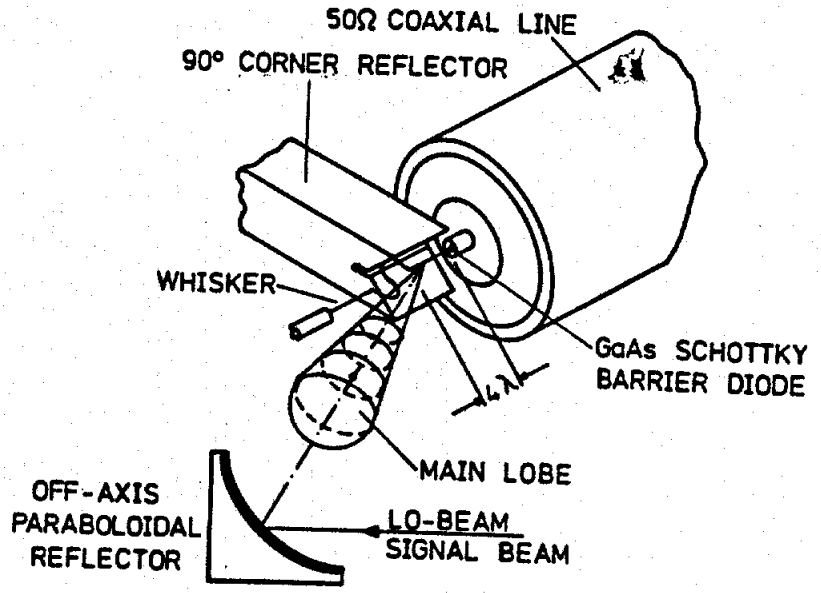

Figure 1.3: A quasi-optical mixer mount using a corner-cube antenna.

resolution processing techniques to achieve a high degree of reproducibility.

Millimeter-wave integrated circuits are either hybrid or monolithic. In hybrid circuits, the RF circuit is integrated on an insulating substrate and discrete, subminiature, semiconductor devices are mounted on the circuit. Then, the hybrid circuit is either placed in a thin-wall channelized housing or suspended in a waveguide cavity depending on the application. The hybrid approach leads to low startup costs and to circuit flexibility with reasonably low production cost. Also, the devices in a hybrid module can be evaluated individually prior to circuit integration. Hybrid integrated circuits been used extensively in the last decade and still being used now in the millimeter-wave frequency range for many commercial, scientific and military applications such as fundamental, balanced and subharmonic mixers, transceiver systems, amplifiers, and voltage-controlled oscillators [43, 44].

In monolithic circuits, the RF circuits and the active devices are both integrated on semiconductor substrates. Multifunction circuits are formed on a single semicon-

ductor chip and the optimum layout of these circuits leads to considerable miniaturization of the overall chip. The startup costs for monolithic circuits tend to be very high but when the stage of volume production is achieved, the cost per unit becomes very low. The big advancements in GaAs monolithic technology are making the advantages of millimeter-wave monolithic circuits real and the monolithic approach to be the approach of the future. GaAs MMICs and millimeter-wave monolithic circuits, such as amplifiers and mixer chips, have been developed and tested successfully with very favorable results [43, 45]. The physical dimensions of integrated RF circuits for submillimeter-wave applications make the job of mounting semiconductor devices on these hybrid circuits a very difficult and non-practical task. Also, the availability of semiconductor devices planar chips is limited. Hence, monolithic circuits are currently the only practical solution for the submillimeter-wave region. Yet, monolithic circuits are still in their early stage of development, and hence, the cost of their production is still high. Also, with monolithic circuits, there is no opportunity to adjust, modify, or otherwise "tweak" a circuit to optimize it. That is why hybrid integrated circuits have currently the state-of-the-art performance in millimeter-wave applications [46]. Note that we are not doing here a comparison with millimeter-wave monolithic SIS mixers since they outperform any other millimeter-wave either hybrid or monolithic integrated mixers.

The main important factor in the development of integrated receivers is the development of planar integrated-circuit antennas and of low-parasitic planar GaAs Schottky diodes [25, 26]. In an integrated receiver, the planar antenna is integrated together with the mixer circuit on the same insulating substrate (hybrid) or on the same semiconductor substrate (monolithic). In order for an integrated receiver to compete with a waveguide receiver in the near-millimeter frequency range, it is very

important that its planar antenna has a high coupling efficiency to Gaussian beam optics.

The first generation of integrated receivers was built using integrated antennas on dielectric substrates such as single-slot antenna [47] and double-slot antenna [18]. These antennas have the problem of low radiation efficiencies and poor patterns because of power lost through substrate-modes due to finite substrate thickness [48]. These substrate-modes losses can be eliminated by using a lens of the same dielectric constant as the integrated circuit substrate and attached to the substrate (typically called substrate lens) [48, 49]. This also increases the directivity and the Gaussian coupling efficiency of the printed-circuit antenna. Planar antennas, such as double-dipoles, double slots, log-periodic and spiral antennas, have been used extensively with substrate lenses to build hybrid and monolithic integrated Schottky receivers, and quasi-optical SIS receivers for millimeter- and submillimeter-wave applications. The paper by Rebeiz [50] presents an exhaustive review of the different designs of planar antennas on substrate lenses. The disadvantage of the substrate lens design is their cost when machined out of silicon (or GaAs). They also suffer from dielectric losses and reflection losses at the air-dielectric interface.

The need to have more efficient with no substrate-mode or dielectric losses pushed the development of planar antennas on thin dielectric membranes [51]. These membranes are grown on silicon (or on GaAs) substrates [52] and the area of the substrate on which the antenna will be printed is etched away to the membrane level which acts as an etch stop. In this new design, the membrane is so thin compared with a free-space wavelength that the antenna effectively radiates in free space. Log-periodic and linear tapered slot antennas have been fabricated on thin membranes and resulted in good radiation patterns in the submillimeter-wave range [53, 54].

Since the thin dielectric membrane on which the planar antenna is integrated covers a small area of the semiconductor substrate, the detectors and electronics can be integrated on the surrounding substrate. This, in addition to the absence of losses in this new planar antenna structure, resulted in the development of a two-dimensional imaging array of integrated horn antennas (Fig. 1.4) [51]. An integrated horn antenna consists of a dipole probe integrated on a thin membrane and suspended inside a 70.6° flare angle pyramidal cavity anisotropically etched in silicon. The function of the pyramidal cavity is to increase the efficiency and directivity of the dipole probe, but not to the level of competing with corrugated or dual-mode horns. The large area on the substrate and on the membrane surrounding the dipole probe is available for RF, IF and dc electronics. This makes the integration of the dipole probe and the surrounding circuitry fully planar.

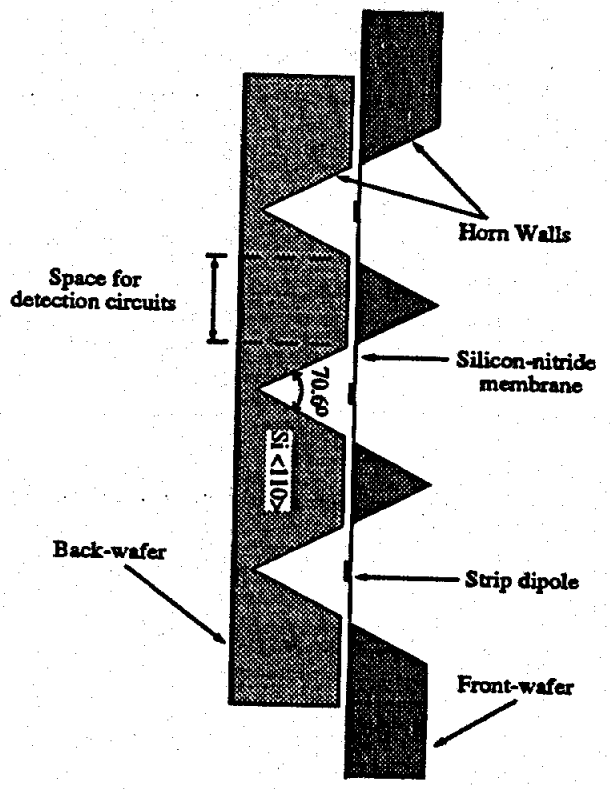

Figure 1.4: The basic structure of an integrated horn antenna.

The work in this thesis is directed toward the development of efficient low noise single-channel planar Schottky receivers based on the integrated horn antenna for millimeter- and submillimeter-wave applications. In chapter 2, the integrated horn antenna is modeled for pattern and impedance measurements. These measurements are very important for the receiver design. Chapter 3 describes the design, fabrication, and performance of an integrated Schottky receiver at 90GHz and 250GHz. This receiver is based on the quasi-integrated horn antenna [55] with a novel planar mixer design. The hybrid approach is chosen for the mixer design because of the availability of high quality low-parasitic surface channel planar GaAs Schottky diodes which are supplied by the University of Virginia and are suitable for the near-millimeter wave frequency range. The 90GHz and 250GHz receivers resulted in the best performance up to date for a room temperature quasi-optical receiver employing a planar diode. Also, a submillimeter-wave integrated receiver at 335GHz has been built with another novel mixer design, and its measured noise figure is within 1dB of the noise figure at 335GHz of the best tuned room temperature waveguide receivers employing a similar planar diode. Chapter 4 describes the design and performance of a 94GHz two-dimensional imaging array of dual-polarized integrated horn antennas. The orthogonal dipole probes on the membrane are fed with a novel feeding structure.

In appendix A, the design and performance of a 16×16 802GHz array of integrated horn antennas are described. A thorough study of quasi-optical diplexers and the derivation of mixer noise temperature in a quasi-optical receiver system are presented in appendices B and C, respectively. Appendix D describes the fabrication processes used for micromachining the V-groove and the trenches, which are part of the integrated horn antenna structure.

CHAPTER II

MILLIMETER-WAVE INTEGRATED HORN ANTENNAS

Integrated circuit antennas are the leading technology used for millimeter- and submillimeter-wave applications that vary from plasma diagnostics imaging arrays to radio-astronomy and anti-collision radars. At these frequencies, the planar antenna (or the antenna-array) is an essential part of the integrated circuitry. The basic requirements for most antennas are acceptable radiation efficiency, symmetrical far-field pattern, and impedance. This, in turn, translates to a high coupling efficiency to a lens or a reflector if the planar antenna is used as a focal plane sensor.

Several planar printed-circuit antennas on dielectric substrates have been developed such as the linear tapered slot antenna [56], the single-slot antenna [47], and the twin-dipole antenna [57]. These antennas are easy to integrate but they suffer from surface wave and substrate-mode losses [58, 59, 48]. This results in poor patterns and low antenna radiation efficiencies.

To solve this problem, the planar antenna is mounted on a dielectric lens which eliminates the substrate modes, and increases the effective aperture and coupling efficiency of the antenna [60, 61, 49]. Double-slot [42, 62], double-dipole [63], log-periodic [64, 65], and spiral antennas [38] on dielectric lenses have been successfully

ture, or millimeter-wave frequencies. The main disadvantage of planar antennas as well as their dielectric lens counterparts lenses is the diffraction limit, whereby signals become considerably lighter at critical frequencies because some [W] and some reflection losses at the surface of the lens due to the dielectric's bulk.

One way to circumvent the [IC] loss of integrated antennas on substrates at millimeter waves is to integrate the antennas on a low-dielectric substrate. The simplest way this is accomplished is by the open method, as we already discussed in [IC, 81]. The antenna effectively radiates in free space and hence, free space antenna design techniques can be used. This leads to the introduction of the integrated horn antenna by Rebeiz and Rutledge [IC] (Figure 51).

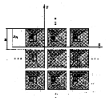

Figure 51: An integrated horn antenna (imaging mode). Dark antenna is fed by a vertically-polarized dipole.

ture, or millimeter-wave frequencies. The main disadvantage of planar antennas as well as their dielectric lens counterparts lenses is the diffraction limit, whereby signals become considerably lighter at critical frequencies because some [W] and some reflection losses at the surface of the lens due to the dielectric's bulk.

One way to circumvent the [IC] loss of integrated antennas on substrates at millimeter waves is to integrate the antennas on a low-dielectric substrate. The simplest way this is accomplished is by the open method, as we already discussed in [IC, 81]. The antenna effectively radiates in free space and hence, free space antenna design techniques can be used. This leads to the introduction of the integrated horn antenna by Rebeiz and Rutledge [IC] (Figure 51).

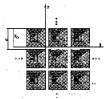

Figure 51: An integrated horn antenna (imaging mode). Dark antenna is fed by a vertically-polarized dipole.

ture, or millimeter-wave frequencies. The main disadvantage of planar antennas as well as their dielectric lens counterparts lenses is the diffraction limit, whereby signals become considerably lighter at critical frequencies because some [W] and some reflection losses at the surface of the lens due to the dielectric's bulk.

One way to circumvent the [IC] loss of integrated antennas on substrates at millimeter waves is to integrate the antennas on a low-dielectric substrate. The simplest way this is accomplished is by the open method, as we already discussed in [IC, 81]. The antenna effectively radiates in free space and hence, free space antenna design techniques can be used. This leads to the introduction of the integrated horn antenna by Rebeiz and Rutledge [IC] (Figure 51).

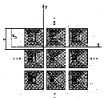

Figure 51: An integrated horn antenna (imaging mode). Dark antenna is fed by a vertically-polarized dipole.

ture, or millimeter-wave frequencies. The main disadvantage of planar antennas as well as their dielectric lens counterparts lenses is the diffraction limit, whereby signals become considerably lighter at critical frequencies because some [W] and some reflection losses at the surface of the lens due to the dielectric's bulk.

One way to circumvent the [IC] loss of integrated antennas on substrates at millimeter waves is to integrate the antennas on a low-dielectric substrate. The simplest way this is accomplished is by the open method, as we already discussed in [IC, 81]. The antenna effectively radiates in free space and hence, free space antenna design techniques can be used. This leads to the introduction of the integrated horn antenna by Rebeiz and Rutledge [IC] (Figure 51).

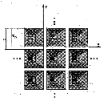

Figure 51: An integrated horn antenna (imaging mode). Dark antenna is fed by a vertically-polarized dipole.

ture, or millimeter-wave frequencies. The main disadvantage of planar antennas as well as their dielectric lens counterparts lenses is the diffraction limit, whereby signals become considerably lighter at critical frequencies because some [W] and some reflection losses at the surface of the lens due to the dielectric's bulk.

One way to circumvent the [IC] loss of integrated antennas on substrates at millimeter waves is to integrate the antennas on a low-dielectric substrate. The simplest way this is accomplished is by the open method, as we already discussed in [IC, 81]. The antenna effectively radiates in free space and hence, free space antenna design techniques can be used. This leads to the introduction of the integrated horn antenna by Rebeiz and Rutledge [IC] (Figure 51).

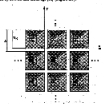

Figure 51: An integrated horn antenna (imaging mode). Dark antenna is fed by a vertically-polarized dipole.

ture, or millimeter-wave frequencies. The main disadvantage of planar antennas as well as their dielectric lens counterparts lenses is the diffraction limit, whereby signals become considerably lighter at critical frequencies because some [W] and some reflection losses at the surface of the lens due to the dielectric's bulk.

One way to circumvent the [IC] loss of integrated antennas on substrates at millimeter waves is to integrate the antennas on a low-dielectric substrate. The simplest way this is accomplished is by the open method, as we already discussed in [IC, 81]. The antenna effectively radiates in free space and hence, free space antenna design techniques can be used. This leads to the introduction of the integrated horn antenna by Rebeiz and Rutledge [IC] (Figure 51).

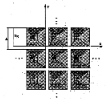

Figure 51: An integrated horn antenna (imaging mode). Dark antenna is fed by a vertically-polarized dipole.

ture, or millimeter-wave frequencies. The main disadvantage of planar antennas as well as their dielectric lens counterparts lenses is the diffraction limit, whereby signals become considerably lighter at critical frequencies because some [W] and some reflection losses at the surface of the lens due to the dielectric's bulk.

One way to circumvent the [IC] loss of integrated antennas on substrates at millimeter waves is to integrate the antennas on a low-dielectric substrate. The simplest way this is accomplished is by the open method, as we already discussed in [IC, 81]. The antenna effectively radiates in free space and hence, free space antenna design techniques can be used. This leads to the introduction of the integrated horn antenna by Rebeiz and Rutledge [IC] (Figure 51).

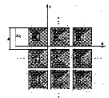

Figure 51: An integrated horn antenna (imaging mode). Dark antenna is fed by a vertically-polarized dipole.

ture, or millimeter-wave frequencies. The main disadvantage of planar antennas as well as their dielectric lens counterparts lenses is the diffraction limit, whereby signals become considerably lighter at critical frequencies because some [W] and some reflection losses at the surface of the lens due to the dielectric's bulk.

One way to circumvent the [IC] loss of integrated antennas on substrates at millimeter waves is to integrate the antennas on a low-dielectric substrate. The simplest way this is accomplished is by the open method, as we already discussed in [IC, 81]. The antenna effectively radiates in free space and hence, free space antenna design techniques can be used. This leads to the introduction of the integrated horn antenna by Rebeiz and Rutledge [IC] (Figure 51).

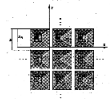

Figure 51: An integrated horn antenna (imaging mode). Dark antenna is fed by a vertically-polarized dipole.

2.1 Integrated Horn Antenna Fabrication

The mainpart of the integrated horn antenna is the membrane wafer. It consists of a silicon wafer on which a tri-layer of $SiO_2/Si_3N_4/SiO_2$ (top/center/bottom) of thickness ($\sim$ 4500Å/$\sim$ 3500Å/$\sim$ 7500Å) is grown on both sides. This trilayer of oxide/nitride/oxide films forms the membrane layer. The silicon wafers used for the membrane wafer and the other wafers forming the horn have their surface plane as the $< 100 >$ crystal plane [68].

The membrane wafer is patterned from the back-side and the trilayer is etched away to expose the silicon substrate. The silicon substrate is then etched anisotropically either using an ethylenediamine-pyrocathecol-water solution (EDP) or a hydroxide potassium (KOH)-water solution [68, 69]. The anisotropic etchant will continue to etch the silicon substrate until it reaches the other side of the wafer and the membrane will act as an etch stop, leaving a transparent membrane with a thickness of 1.4-1.5μm.

When etching using the EDP solution, the membrane layer is not attacked because the top layer of SiO_2 is etched at an extremely slow rate [70]. However, for the case of the KOH-H_2O solution, the top SiO_2 layer is attacked, and a masking layer has to be present during etching on the side of the membrane in order to protect it [68]. Anisotropic etchants attack the $< 111 >$ surfaces at a much slower rate than the $< 100 >$ surfaces. For EDP and KOH , the anisotropic etch-rate ratios of $< 100 >$ plane over $< 111 >$ plane are 50:1 and 400:1, respectively, and the etch rates are 1-1.2μm/min at 115°C and 0.4-0.5μm/min at 65°C, respectively. Normally, KOH etchant is used when very smooth walls are required (submillimeter-wave antennas) and when the membrane dimensions are smaller than 1mm so that the membrane can still hold even with the top oxide layer is etched away. Due to the slower etch

rate in the < 111 > planes than in the < 100 > planes, the resulting walls of the cavity formed are bounded by < 111 > crystal planes which are at an angle of 54.7° with the < 100 > planes (figure 2.2). We can express the dimensions of the resulting membrane as :

$W_{membrane} = W_{opening} - (2t)\tan(90° - 54.7°) \approx W_{opening} - \sqrt{2}t$,

where t is the wafer thickness.

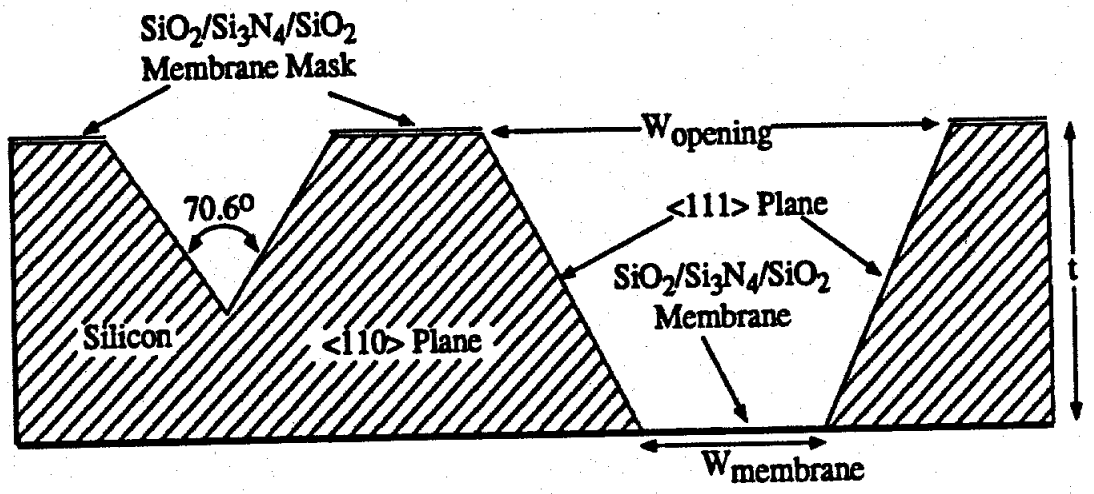

Figure 2.2: The membrane wafer. The feed-dipole antenna is integrated on the thin transparent membrane layer.

Before processing on the membrane wafer, the wafer is cleaned to remove any residual etchant using a 1:1 DI-H_2O:H_2SO_4 solution for 1 min. and then rinsed with water. The feed-dipole is then integrated on the thin membrane and any circuitry related to the antenna or receiver design is integrated around the membrane on the silicon wafer. The fabrication of the circuit is done with regular lithography techniques. More detail on the fabrication procedure are presented in [51, 71].

A dipole antenna suspended on the thin membrane acts as a dipole antenna in

air. Hence, its directivity and effective aperture are very low and it would very unefficient to use such kind of an antenna in an imaging or a receiver system. To increase the directivity of the feed-dipole antenna, we took advantage of the 35.3° angle between the < 111 > crystal plane and the normal direction to the < 100 > plane to form a pyramidal cavity containing the feed-dipole antenna. This is done by etching additional silicon wafers and attaching them to the front and to the back of the membrane wafer in order to complete the pyramidal cavity which has a flare angle of 70.6° (2×35.3°) (Figure 2.3). The depth of the horn d_H is related to the opening of the horn $W_{opening}$ by

$d_H = W_{opening}/\sqrt{2}$. The number of wafers used to complete the cavity depends on the horn opening and on the position of the feed-dipole inside the cavity. The wafers used for completing the cavity are completly etched through and therefore need to have only an oxide layer for use as a mask when etching in EDP or KOH.

The horn collects the energy incident on its aperture, and focuses it on the dipole antenna suspended on the membrane inside the horn. The integration of the dipole-antenna on the thin membrane layer eliminates the possibility of coupling some of the power incident on the dipole-antenna into substrate modes and eliminates the need of a substrate lens. The focusing properties of the horn increase the effective area of the dipole, thus leaving plenty of room for integrating circuitry around the membrane on the wafer. This gives us the ability to build a closely spaced array of integrated horn antennas and still leave ample space around the dipole underneath the horn opening area for the interconnections and detection circuitry (Figure 2.4).

We will start by discussing the single-element integrated horn antenna in a ground plane, since most of the work in this thesis is based on single-element integrated horn antennas. The design of the horn antenna involves the selection of the horn aperture

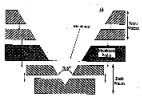

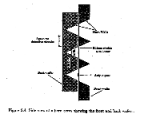

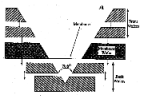

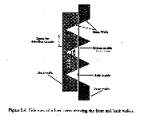

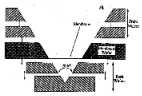

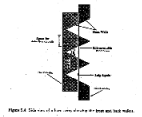

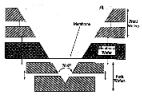

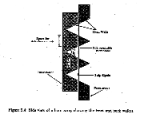

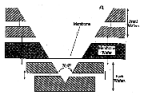

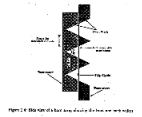

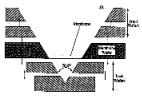

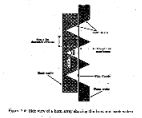

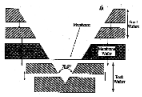

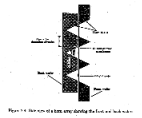

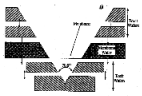

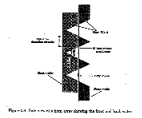

size and the dipole position in the cavity. A horn aperture smaller than 0.8λ results in a wide radiation pattern with a directivity around 8 dB. This pattern does not have any advantage over elementary antennas such as a dipole backed by a ground plane. On the other hand, a horn aperture greater than 1.8λ suffers from aperture phase errors due to the large flare angle of the horn [72]. Also, the horn radiation pattern and the dipole input impedance are strongly dependent on the dipole position inside the horn cavity. For example, a dipole position close to the apex lies near the cutoff region of the horn and results in a low input impedance, while the high-order modes triggered by a dipole position close to the aperture distort the aperture field and yield poor radiation patterns and low aperture efficiencies. From the theoretical analysis developed by George Eleftheriades for the integrated horn antenna in a ground plane [73, 74], we find that for a 70° flare angle, horn apertures from 1.0λ-square to 1.5λ-square with dipole positions between 0.36λ and 0.55λ result in good radiation patterns and practical values of dipole impedances.

2.2 Impedance Measurements

A microwave model at 1-2GHz was constructed for impedance measurements. The dipole antenna was fed using a coaxial cable and a coplanar-strip transmission line shorted $\lambda/4$ away from the feed (Figure 2.5). This design has two purposes. It models the low-frequency connection on the membrane effectively, and provides an effective Balun for the coax-dipole transition. The dipole antenna was modeled using copper tape over a thin polyethylene sheet which represents the membrane. The dipole was also fed along the axis of the horn with a coaxial cable and an appropriate Balun. Both measurements resulted in identical results. A strip width of 0.015λ-0.025λ was used in the following measurements.

The measured resonant resistance and resonant length of the feed dipole vs. dipole position are compared with theory [74] in figure 2.6. The resonant resistance is a strong function of the dipole position, and varies from 25Ω to 175Ω for dipole positions between 0.34λ and 0.6λ. As predicted by the fullwave analysis [74], the strip dipole cannot achieve resonance for feeding positions between 0.6λ and 0.8λ. This is due to the fact that at these positions, the dipole antenna resides in a strong capacitive region and the horn geometry limits the length of the dipole antenna which will provide the adequate inductance in order to obtain resonance. There is a second region of resonance near the aperture of the horn, but the corresponding radiation patterns are poor, because the higher order modes (mainly TE_{12} and TM_{12}), which are excited now close to the aperture, disturb significantly the dominant mode distribution at the aperture.

The input impedances versus frequency for various feed positions are presented in figure 2.7. It is seen that the dipole impedance increases and becomes more wideband as the dipole is moved away from the apex. The measured results agree very well with theory [75]. The region around 0.6λ resulting in large radiation resistances (150-200Ω) corresponds to the region where the horn focuses the incident energy from the aperture and which results in the largest values of the electric field along the horn axis [58, 51].

Measurements and theory [73] indicate that as long as the dipole is located within about 0.55λ from the apex of the horn, its input impedance is mainly determined by the local cavity environment and not by the size of the horn radiating aperture. Thus, the dipole impedances of figure 2.6 (up to a position of 0.55λ from the apex) are equally valid for 1.0λ, 1.5λ, and 2.0λ horn apertures. Also, the radiation patterns of the antenna and its directivity are not dependent on the dipole position when

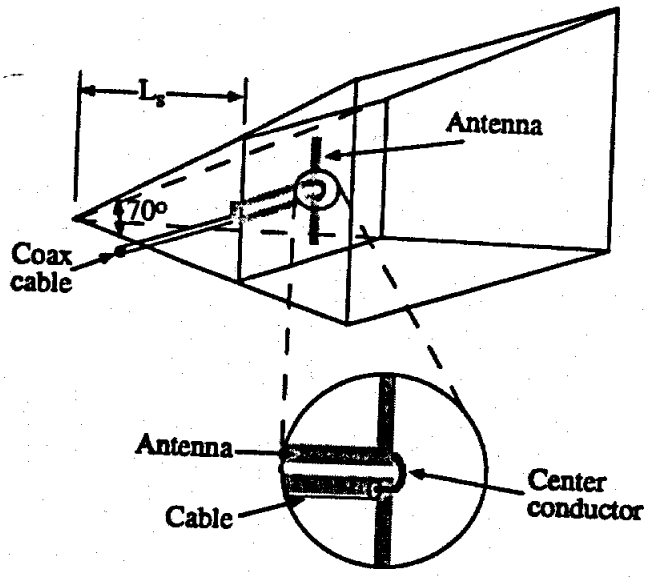

Figure 2.5: Microwave impedance measurement setup at 1-2GHz. The shorted coplanar-strips act as a balun and models the low-pass filter and the bias line in the 92GHz antenna.

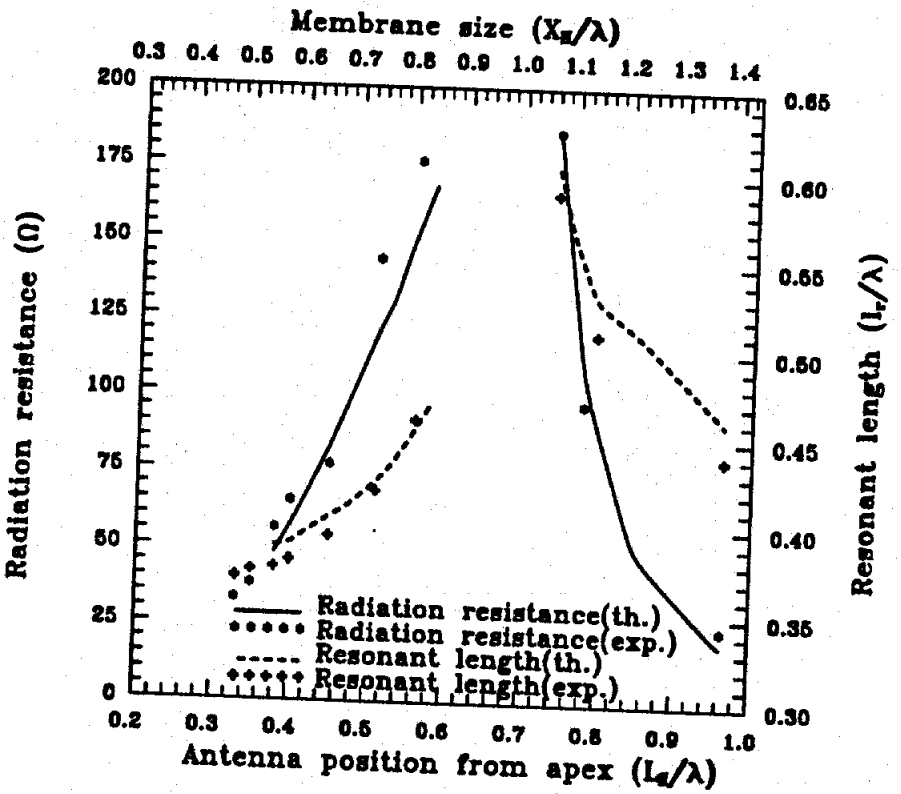

Figure 2.6: Measured and predicted dipole resonant resistance and resonant length versus dipole position from the apex. Notice the region of no resonance in the center of the horn.

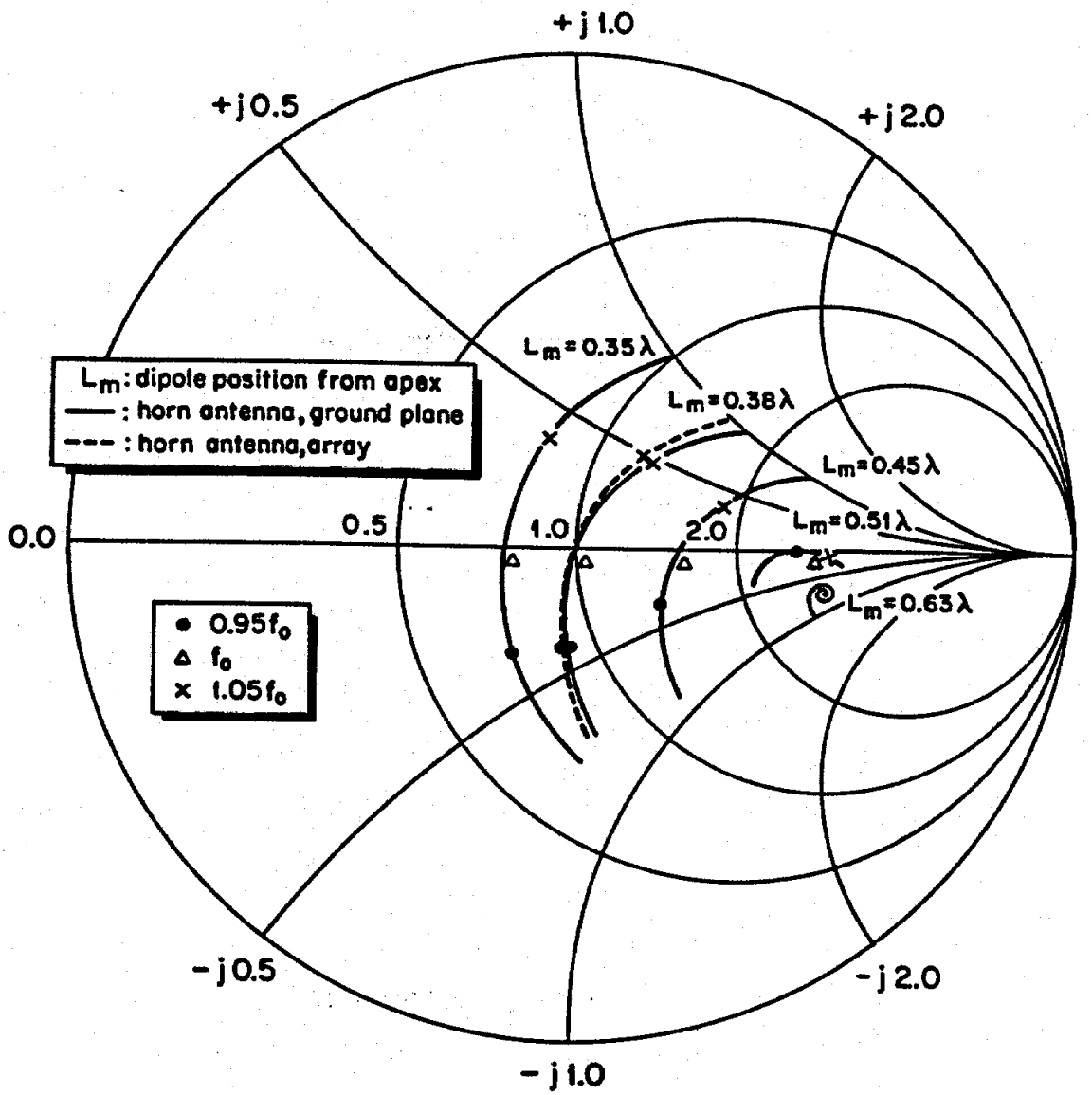

Figure 2.7: The input impedances versus frequency for various feed positions in the horn cavity. The dashed line is the measured impedance of a dipole in a 3×3 array at 7.3GHz [71].

placed below 0.55λ from the apex, because of the dominant excitation of TE_{10} mode in the horn cavity. For these dipole feed positions ($L_s < 0.55\lambda$), the far-field pattern is only dependent on the horn aperture size. This leads to the independence of the feed-dipole input impedance design and the antenna directivity design. Figure 2.7 shows that for dipole positions between 0.36λ and 0.55λ, we can obtain feed-dipole impedances which are suitable for Schottky diodes and SIS mixers.

2.3 Pattern Measurements

An integrated horn antenna with an aperture of 1.35λ-square and a dipole position of 0.38λ from the apex was fabricated for microwave and millimeter-wave pattern measurements. This design is based on the criteria discussed in the previous two sections of this chapter. The corresponding membrane is 0.54λ-square. The dipole is placed at the center of the membrane, and a resistive bolometer detector integrated at its apex. The length of the feed-dipole is 0.38λ because it results into a radiation resistance close to 50Ω at the design frequency (Fig. 2.6). The 0.54λ membrane allows the integration of a simple coplanar-strip $\lambda/4$ low-pass filter which results in a very large parallel impedance at the dipole apex [51]. The bolometer detector presents there a much lower impedance and absorbs all the received power.

A microwave model at 3GHz with a ground-plane dimension of 2.5λ-square was used for pattern measurements. For the 92GHz measurements, the horn design resulted in a front and back wafer thicknesses of 1.9mm and 1.25mm, respectively. The front and back wafers were constructed from a stack of low resistivity ($\rho = 1\ \Omega$–cm) silicon wafers with nominal thicknesses of 760μm and 380μm (Fig. 2.8). The variation in wafer thickness and alignment repeatability introduced several 60μm steps in the horn cavity. The horn sidewalls are gold coated except for the sidewalls of

the membrane wafer in order not to overshadow the membrane. This lowers the cross-polarization by 2-3dB and has a negligible effect on the co-polarized pattern [51, 76]. For patterns measurements, a 4μm$\times 4\mu$m-square bismuth microbolometer [51, 77] with a resistance of 70Ω is integrated at the apex of the dipole antenna, and is used for detecting the power coupled to the dipole antenna.

The measured E- and H-plane patterns (Figures 2.9, 2.10) agree well with theory at 3GHz and 92GHz [74, 78]. The discrepancy in the E-plane pattern for large angles are due to the finite size of the ground-plane at 3GHz, and to the steps in the sidewalls at 92GHz. Also note that the pattern is rotationally symmetric due to the small presence of the TE_{12} and TM_{12} modes on the aperture which taper the fields in the E-plane.

This antenna at 92GHz has a calculated directivity of 12 ± 0.3dB and translates into an aperture efficiency (coupling to a plane wave) of $70\%\pm 4\%$. It is possible to get a higher directivity (up to 15dB) from an integrated horn antenna structure with an opening of 3.0λ but at an expense of a very low aperture efficiency of 30% (due to the phase errors on the horn aperture) [73]. The cross-polarization component was very low and not measurable in the E and H-plane scans. The 45°-plane pattern also agrees well with theory (Fig. 2.10), but the cross-polarization component could not be measured due to signal-to-noise ratio limitations.

2.4 Comparison with Two-Dimensional Horn Arrays

The measured input impedance for feed positions between 0.36λ and 0.55λ did not change if the ground-plane was removed or if the horn was placed in the middle of a 3×3 array [71]. Also, for the dipole positions mentioned above, the measured (and predicted) impedance is insensitive to the horn aperture size. This is because

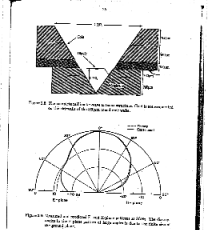

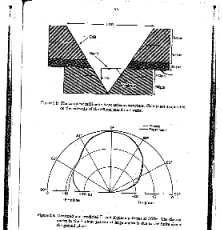

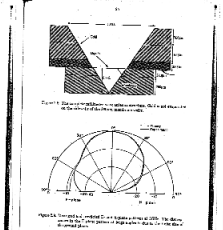

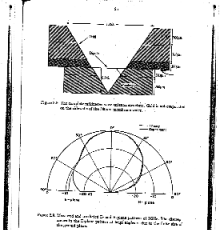

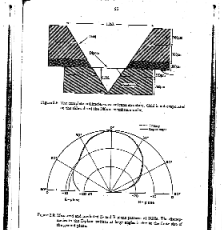

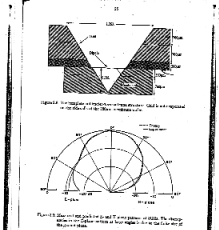

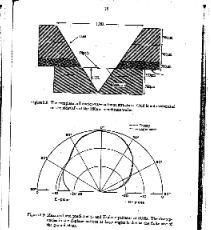

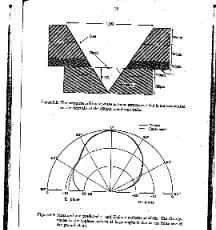

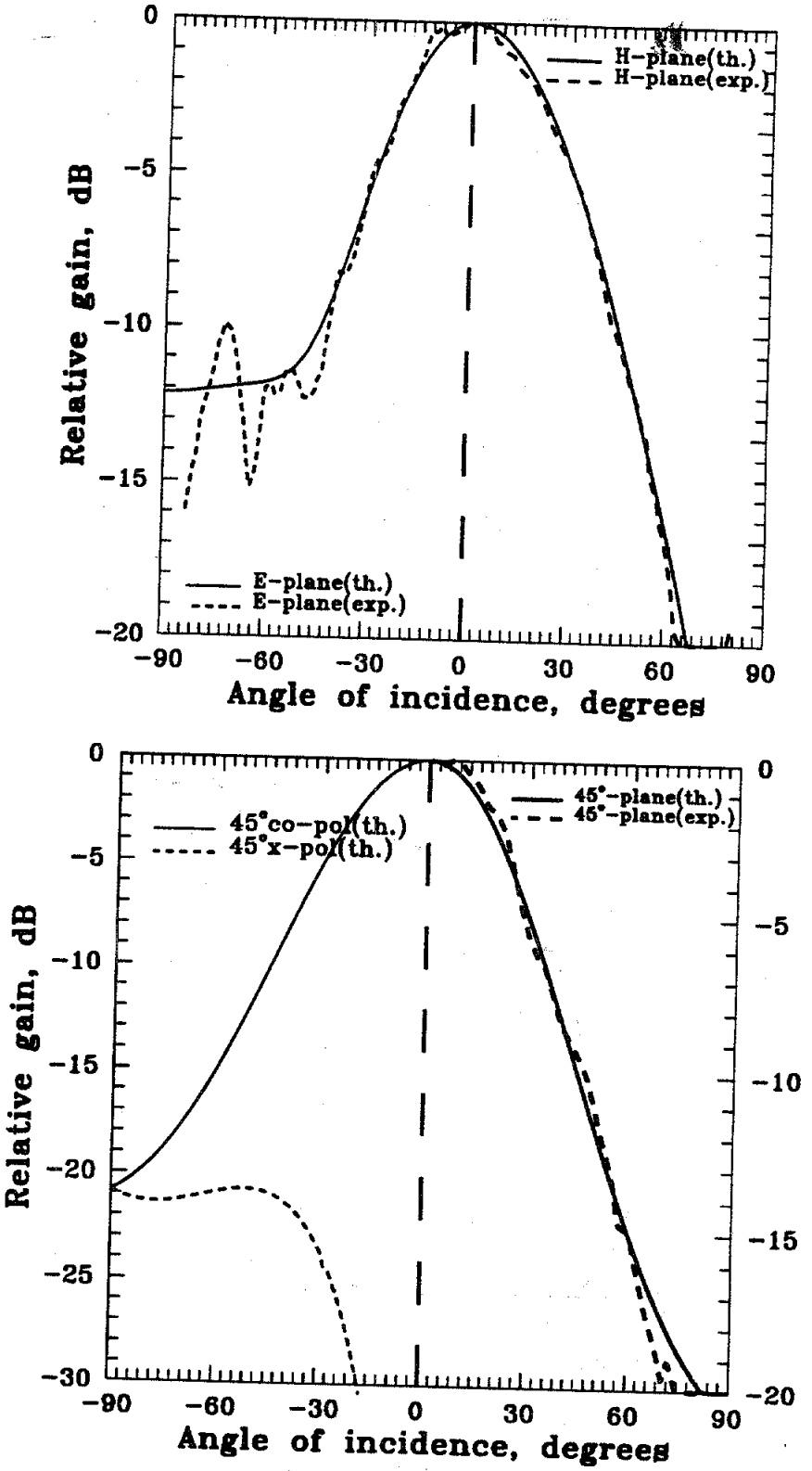

Figure 2.10: Measured and predicted E-,H- (top) and 45°-plane (bottom) patterns at 92GHz. The discrepancy in the E-plane pattern at large angles is due to the steps in the sidewalls.

at feed positions far from the aperture, the impedance is determined mainly by the geometry of the horn cavity and not by the transition to free space. The predicted impedances and resonant lengths for a horn in an infinite ground-plane can therefore be safely used for the design of two-dimensional horn arrays for dipole positions between 0.36λ and 0.55λ and for horn apertures greater or equal to 1λ. Indeed, the experimentally determined resonant length and radiation resistance used by Guo et al. [76] for the design of an efficient 1λ imaging array agree well with our calculations and measurements for a 1.35λ horn in a ground-plane with the same dipole position and dipole length (Fig. 2.7). For imaging arrays with apertures smaller than 1λ, the mutual-coupling among the array elements starts affecting the dipole impedance and the antenna patterns.

The patterns for a 1.35λ-square horn in a ground-plane and in a two-dimensional array are shown in figure 2.11. Reciprocity and mode-matching technique at the horn aperture has been successfully used to predict the pattern of a horn element in a two-dimensional array [73, 51]. The TE_{10} tapering of the electric field across the aperture yields a vanishing tangential electric field at the edges of the horn and therefore decouples the horn from the array environment. This results in an H-plane pattern that is similar to that of a horn in an infinite ground-plane as long as the horn aperture is larger than 1λ. In the case of the E-plane pattern, the horn sees the array and the spikes and nulls in the pattern are due to the discrete nature of the Floquet-modes [79]. It is clear from the patterns that a horn in a two-dimensional array will always yield a higher gain and spillover efficiency than a horn in an infinite ground-plane. This is due to the null in the E-plane pattern at 90° and is a result of the vanishing electric field at grazing angles in a two-dimensional array.

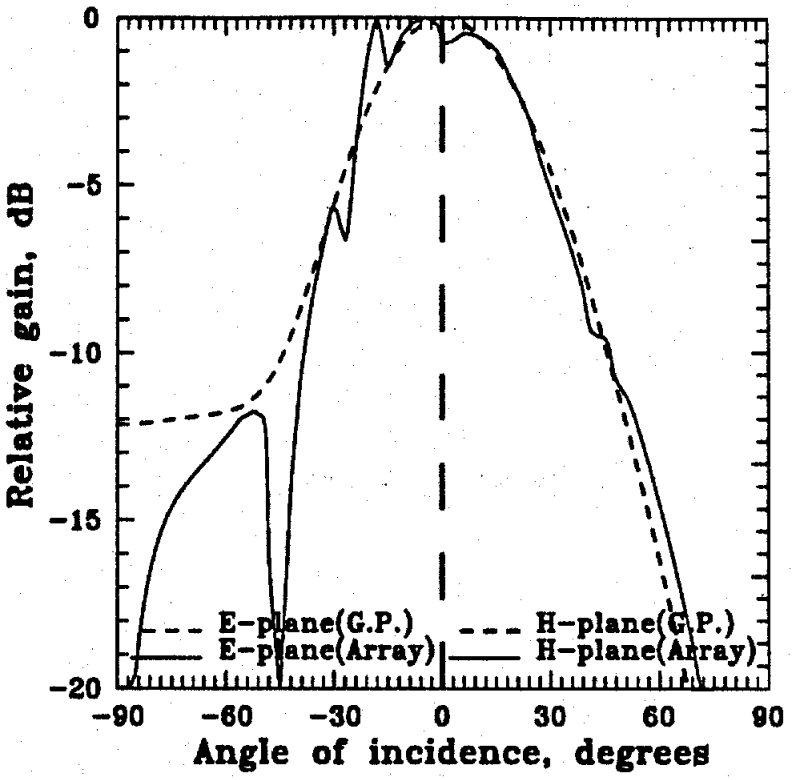

Figure 2.11: The E- and H-plane patterns of a 1.35λ horn antenna in a ground plane and in a two-dimensional array.

CHAPTER III

MILLIMETER AND SUBMILLIMETER-WAVE QUASI-INTEGRATED HORN ANTENNA SCHOTTKY RECEIVERS

In the previous chapter, the integrated horn antenna design was presented. The impedance measurements showed that for feed-dipole positions between 0.36λ and 0.55λ from the apex of the horn, the dipole impedance is determined mainly by the geometry of the horn cavity and not by the transition to free space, and the resulting impedances values are suitable for Schottky diodes and SIS mixers. Also, the theoretical study done in [73, 74] and the experimental verification presented in the previous chapter showed that horn apertures between 1.0λ and 1.5λ, either in an array or in a ground plane, result in good radiation patterns, independent of the dipole position as long as it is below 0.55λ from the horn apex. The resulting directivities are between 10dB and 13dB. The three main points which are important to mention and make the integrated horn antenna a good candidate for use in millimeter- and submillimeter-wave receivers are:

- The integrated horn antenna does not suffer from dielectric losses and substrate-mode losses like other planar antennas on dielectric substrates or dielectric lenses [50].

- The integrated horn antenna is ideally suited for imaging array applications with lots of space available for IF and low frequency connections.

- As will be seen in this chapter, a quasi-integrated horn antenna can be designed to yield a 97% Gaussian coupling efficiency.

Quasi-optical components such as interferometers, lenses, and reflectors are used for coupling the signal power into planar antenna receivers in the millimeter- and submillimeter-wave region. The wave suffers from diffraction loss while propagating through these quasi-optical components of finite diameter. A solution to the wave equation including diffraction is an orthogonal set of basis functions, termed "Gaussian modes", which are characterized by the fact that the transverse amplitude and phase distribution of the propagating beam possess circular symmetry [10]. The lowest order Gaussian mode or fundamental mode is of primary importance in practical receivers because it results in the smallest possible optics for the quasi-optical system. A well designed quasi-optical system allows nearly lossless propagation of the fundamental mode and any conversion of energy to higher order modes is regarded as undesired loss. Hence, the coupling efficiency between the receiver antenna and the fundamental Gaussian beam should be maximized. This is done by producing at the aperture of the feed antenna a field distribution whose radiation pattern is symmetric and highly Gaussian.

Scalar feed horns and dual-mode feed horns are examples of antenna feeds with high Gaussian coupling efficiency (A corrugated conical horn antenna with finite dimensions has a 97-98% Gaussian coupling efficiency) [16]. Note that a feed antenna optimized to yield a high Gaussian coupling efficiency does not result in the highest aperture efficiency (coupling to a plane wave) which requires a different aperture distribution (uniform field distribution). In fact, a Gaussian field [illegible]

circular aperture yields a 97-99% Gaussain coupling efficiency and a 55-60% aperture efficiency [72]. Integrated horn antennas are desirable for imaging since they result in a relatively high aperture efficiency (70-80%) (due to the presence of the dominant TE_{10} on the aperture) [51, 76, 78]. On the other hand, the coupling efficiency of integrated horn antennas, with an aperture opening between 1.0λ and 1.5λ, to the fundamental Gaussian beam is around 75-80% [73, 55]. This introduces a 1.2dB increase in the receiver conversion loss and noise performance.

In this chapter, the design and performance of 90GHz, 250GHz, and 330GHz *quasi-integrated* horn antenna receivers are described. The RF coupling structure of these receivers is a modification of the integrated horn antenna described in the previous chapter. It exhibits a high Gaussian coupling efficiency (97%) and is a considerable improvement over standard integrated-circuit antennas. The planar mixer circuit, along with the feed dipole, are both integrated on the membrane wafer. The diode used for mixing is a planar University of Virginia surface-channel Schottky diode. The IF signal is taken out through a simple CPS line on the silicon substrate and through an IF matching network. The mixer requires no tuning and no additional RF matching network, and shows excellent performance over a 10% bandwidth. The low cost of fabrication and the simplicity of the design makes it ideal for use in millimeter- and submillimeter-wave receivers, and the resulting performance compares favorably with the performance of the best Schottky waveguide mixers.

3.1 Antenna Design

A quasi-integrated horn antenna has been designed by Eleftheriades et al. [80, 55] to overcome the limitations of the large flare angle of the integrated horn antenna. In this design, a flared machined section is attached to the front part of the integrated

horn antenna to result in higher gain patterns (Figure 3.1). The abrupt change of flare-angle at the junction of the integrated section and the machined section of the horn acts as a mode converter that excites mainly the TE_{10}, TE_{12}/TM_{12} and TE_{30} modes. These modes are properly phased on the radiating aperture by appropriately selecting the length and the flare-angle of the machined section. This results in highly symmetrical far-field patterns with higher gain. Hence, we have now a quasi-integrated horn antenna compatible with integrated circuits, and which does not suffer neither from dielectric losses nor from surface wave losses and has a performance comparable to high gain scalar feed and dual-mode horns.

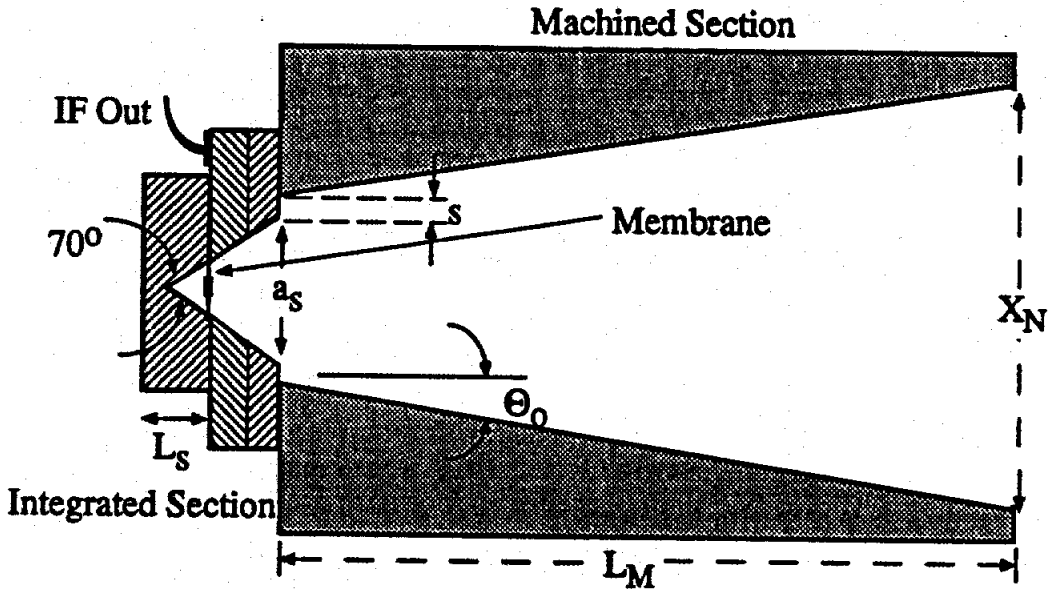

Figure 3.1: A quasi-integrated horn antenna structure.

The design of the integrated horn antenna section is the same as the one discussed in the previous chapter for the 92GHz pattern measurements. The 1.35λ integrated horn antenna aperture does not yield a lot of phase errors at the junction of the integrated section and the machined section. The 0.38λ feed-dipole position from the integrated horn apex results in feed-dipole impedance values suitable for Schottky

and SIS mixers (Figure 2.7), and determined mainly by the geometry of the horn cavity and not by the transition to the machined section. This is valid for dipole positions below 0.55λ from the horn apex, and this will facilitate the mixer modeling because there is no need to model the machined section for impedance measurements. The minimum dimension of the machined section is about 1.35λ-square, which should allow the fabrication of the quasi-integrated horn antenna up to 1.5THz. This is a considerable improvement over waveguide horn technology where it is possible to build corrugated horns up to 300GHz and dual-mode horns up to 600GHz [81].

3.1.1 Patterns and Radiation Characteristics for the 90GHz Quasi-Integrated Horn Antenna

A 20dB quasi-integrated horn antenna was designed for 90GHz using the method discussed above and with $a_s = 1.35\lambda$, $s = 0.0$, $L_M = 7\lambda$, $X_N = 3.56\lambda$ and $\theta_o = 9°$ (see figure 3.1 and [55] for more detail). In the measurement set-up, the machined section is mounted on a fixture, and the integrated horn antenna section is held against the machined section using an x-y-z positioning stage. The measured patterns at 91.4GHz (Figure 3.2) show low sidelobe-levels, a -22dB cross-polarization level in the 45° plane, a 10-dB beamwidth of 34°, and a calculated 97% Gaussian coupling efficiency [73, 55]. An excellent agreement down to -40dB between the measured patterns and the theoretical patterns has been obtained [80, 55].

The quasi-integrated horn antenna aperture dimension is 3.56λ-square and results in a 62.5% aperture efficiency (coupling to a plane wave) at 91.4GHz. Figure 3.3 shows the measured patterns for the 90GHz design at 86.5GHz and 95.5GHz. As shown, the variation in the 10dB-beamwidth is less than 3° in this frequency range. The radiation characteristics of the 20dB quasi-integrated horn antenna at the design frequency and

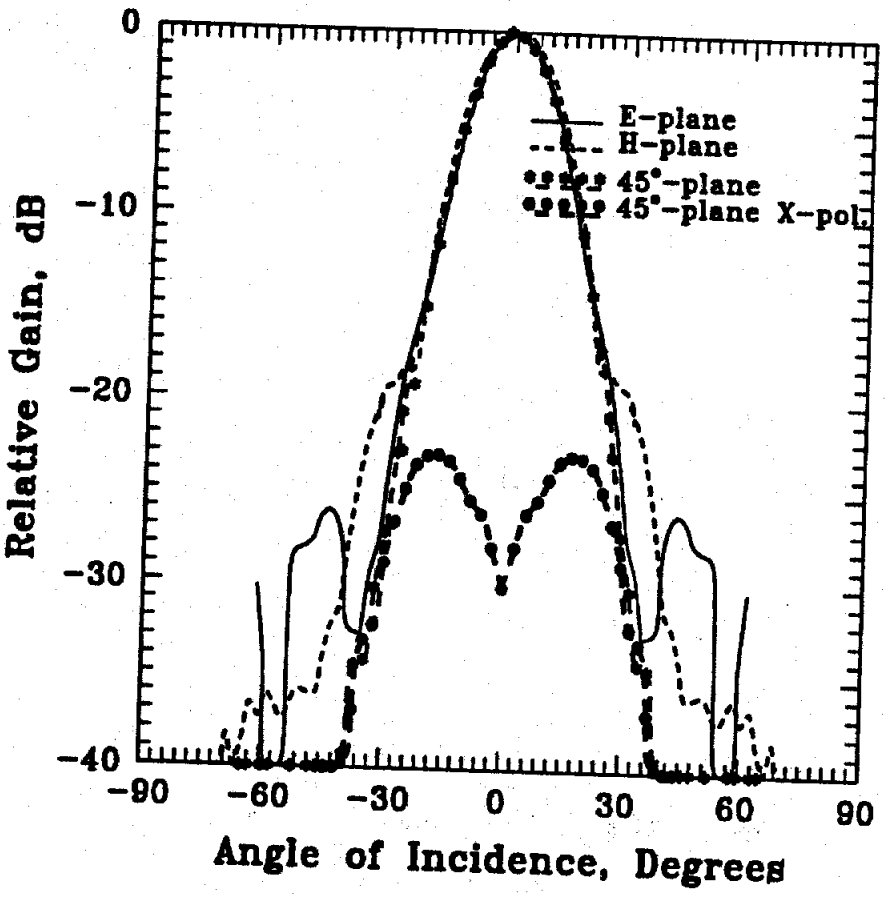

Figure 3.2: The measured E-, H-, 45°-, and x-pol. 45°-plane patterns of the 20dB quasi-integrated horn antenna at 91.4GHz (f_{design} = 90GHz).

	$0.95f_o$	f_o	$1.05f_o$
Gain	19.4dB	20dB	20.6dB
Aperture efficiency	60.6%	62.8%	65.4%
10dB Beamwidth	$37° \pm 1°$	$34° \pm 1.2°$	$32° \pm 1.8°$
Sidelobe-level (E-plane)	-23dB	-27dB	-26.3dB
Cross-pol. (45°)	-22.5dB	-22.7dB	-23dB
Beam-efficiency (to -10dB)	85%	86%	86.5%
Gaussian Coupling efficiency	95.5%	97.3%	96.5%

Table 3.1: The radiation characteristics of the 20dB quasi-integrated horn antenna over a 10% bandwidth.

at $0.95f_o$ and $1.05f_o$ are summarized in Table 3.1. It is seen that the Gaussian coupling efficiency remains very high (above 96%) and that the cross-polarization level remains below -22dB. Table 3.2 shows the calculated gain and coupling efficiency of the 20dB gain quasi-integrated horn antenna from 80 to 110GHz (this is the frequency range over which the receiver measurements were done). It is seen that the variation in the Gaussian coupling efficiency is not more than -0.5dB at the edges of the 30GHz bandwidth. Also, the Gaussian coupling efficiency drops more slowly at the higher end of the bandwidth. It is important to note that in these calculations, the Gaussian beam parameters are optimized at each frequency to obtain for the best coupling between the antenna and the Gaussian beam. In a practical system, this will translate into a slight adjustment of the receiving optics in the 30% bandwidth.

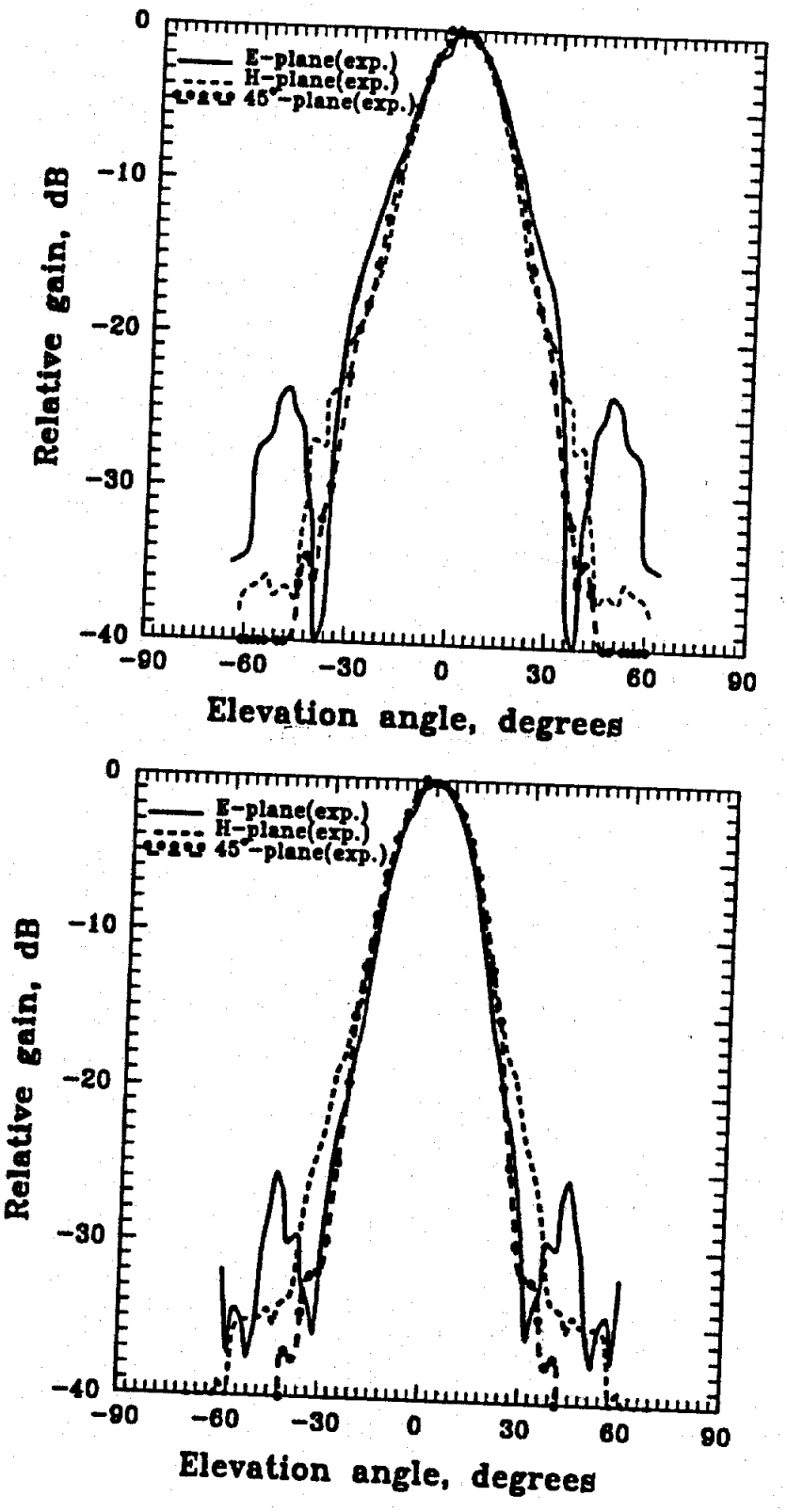

Figure 3.3: The measured E-, H-, and 45-° plane patterns of the 90GHz quasi-integrated horn antenna at 86.5GHz (top) and 95.5GHz (bottom)

Frequency (GHz)	80	85	90	95	100	105	110
Gaussian coupling efficiency %	86	95	97	97	92	88	86
Gain (dB)	18.7	19.4	20.0	20.6	21.3	21.9	22.7

Table 3.2: The calculated gain and Gaussian coupling efficiency of the 20dB quasi-integrated horn antenna from 80GHz to 110GHz. The design frequency is 90GHz.

3.2 A 90GHz Quasi-Integrated Horn Antenna Receiver

3.2.1 Mixer Design

The quasi-integrated receiver consists of an integrated section (Figure 3.4), and a machined section, which is attached to the front of the integrated horn antenna and is not shown in the figure. The integrated structure is based on the design discussed previously in section 3.1. The integrated horn aperture is 1.35λ resulting in a cavity depth of 0.95λ or 3175μm at 90GHz (the cavity depth is related to the 70.6° cavity flare angle).

The pyramidal cavity with the 70.6° flare angle is constructed using low and high resistivity silicon wafers etched anisotropically and stacked together. The appropriate wafer thicknesses used in the 90GHz receiver structure are shown in figure 3.4. Note that the *exact* cavity depth can not be achieved because of the limitations of wafer thicknesses available in the industry. The mixer circuit consisting of the feed-dipole with the CPS lines is integrated on the membrane wafer as shown in figure 3.5.

The horn sidewalls of each silicon wafer, except for the wafer containing the membrane, are coated with gold by flood evaporation before assembling the integrated

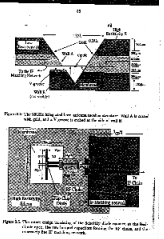

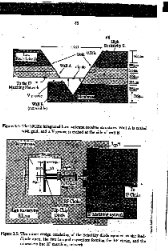

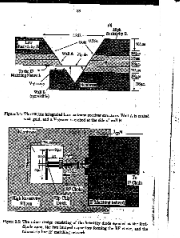

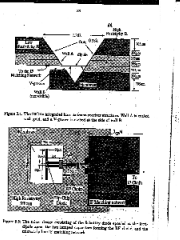

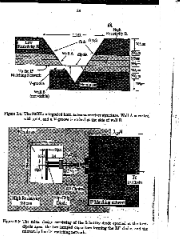

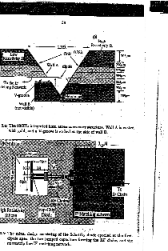

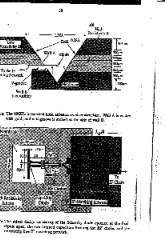

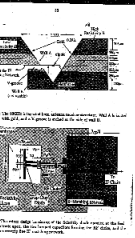

horn antenna. The thickness of the gold evaporated is at least twice the skin depth at 90GHz ($\delta_{skin}^{gold} = 0.25\mu$m at 90GHz). For the membrane wafer, only three sidewalls are coated with gold and the sidewall in *front* of the coplanar stripline (wall A, Figure 3.4) is left uncoated so as not to short the IF and RF signals on the CPS line in the mixer circuit. The three sidewalls of the membrane wafer are coated one at a time by masking the opening of the membrane except the area corresponding to the projection of the side wall on the membrane opening and then flood evaporating gold on the wafer. Again, to avoid an IF short on the CPS line, the sidewall *behind* the coplanar stripline (wall B, Figure 3.4) must also be far enough from the CPS line. To facilitate the fabrication of wall B, a V-shaped groove (70.6°) is etched anisotropically through wall B in the silicon wafer directly behind the membrane (Figure 3.6). Hence, the wafer containing the V-groove in wall B can be flood evaporated with gold, metalizing therefore all the sidewalls including the groove without inducing any short on the CPS line when the wafers are stacked. The silicon wafer containing the V-groove does not need to be of high resistivity type since it is eventually coated with gold. The reader is referred to Appendix D for details on the fabrication of V-shaped grooves in silicon.

A microwave model of a CPS line on a half-space dielectric (Stycast $\epsilon_r = 12$) covered by a V-shaped groove showed that the height of the cavity should be at least 6 times larger than the separation between the two strips forming the CPS line. This is needed in order to minimize the effect of the groove environment on the fields propagating along the CPS line on the dielectric. For the 90GHz design, the V-groove height (or depth) is 300μm which is ten times larger than the separation between the two strips forming the CPS line on silicon. The V-groove cavity is small enough so that no higher-order modes are present at 90GHz. The effective quasi-

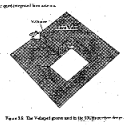

Figure 2.6: The V-shaped groove used in the 193 THz negative design.

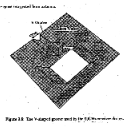

Figure 2.6: The V-shaped groove used in the 193 THz negative design.

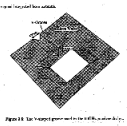

Figure 2.6: The V-shaped groove used in the 193 THz negative design.

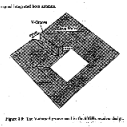

Figure 2.6: The V-shaped groove used in the 193 THz negative design.

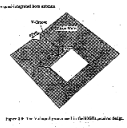

Figure 2.6: The V-shaped groove used in the 193 THz negative design.

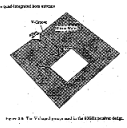

Figure 2.6: The V-shaped groove used in the 193 THz negative design.

Figure 2.6: The V-shaped groove used in the 193 THz negative design.

Figure 2.6: The V-shaped groove used in the 193 THz negative design.

signal on the surrounding dielectric substrate. The height of the high resistivity silicon substrate is chosen so that it appears thick at RF frequencies, and so that the capacitance between the contact pad at the end of each stripline and the underneath ground plane is minimized at IF frequencies. This ground plane is formed during the flood evaporation of gold on the sidewalls of the high resistivity wafer which is above the membrane wafer (Figure 3.4).

In the case of the 90GHz mixer, the high resistivity substrate consists of *two* 355μm high resistivity silicon wafers. The evaporated gold used in forming the mixer circuit is about 5000Å which is equal to twice the skin depth of gold at 90GHz ($\rho_{gold} = 2.2\times10^{-6}$ Ω−cm). An RF choke is defined along the CPS line by using two integrated lumped capacitors. At 90GHz, the first capacitor on the membrane itself is $\lambda_o/4$ away from the dipole apex and the second capacitor on the silicon is $\lambda_e/2$ away from the first capacitor, where λ_e is the effective wavelength of the CPS line on silicon covered on top by the V-shaped groove ($\epsilon_e \simeq (1+\epsilon_r)/2$). The capacitors are fabricated by evaporating two gold patches over the CPS line and using a 1.1μm insulating polyimide dielectric. The polyimide dielectric is Selectiplast HTR3-50 [82] with a measured dielectric constant of 4.0 to 4.5 at microwave frequencies. The separation between the two strips of the CPS line on the silicon wafer is reduced to 30μm rather than the 60μm on the membrane in order to minimize radiation losses of the CPS line in the substrate [48]. The 60μm separation between the two strips of the CPS line on the membrane is chosen to give space for the planar diode anode finger (50μm) when the diode is epoxied at the dipole apex. The CPS line impedance is 220Ω on the membrane ($\epsilon_e = 1$) and 82Ω on the silicon substrate ($\epsilon_e = 6.48$) (the reader is referred to figure 3.5 for the striplines dimensions, and to [83] for impedance calculations). The capacitor integrated on the membrane is approximately 90fF (70μm×240μm)

and the one integrated on silicon is 50fF (70μm×130μm). This results in a low pass filter with a -3dB corner frequency of 35GHz and a rejection of -19dB at 90GHz. The series resistance in the CPS circuit lines is 4 to 4.5Ω. The low pass filter presents a high impedance at the dipole apex at the fundamental frequency 90GHz and shorts the diode at the second harmonic. These are the two most important frequency components for mixer performance, as was shown by the work of Held and Kerr [84, 85] and also in [86].

A microstrip quarter-wave transformer is fabricated on a Duroid 5870 substrate [87] and used to match the 1.4GHz IF diode output impedance to 50Ω. The IF matching network is specifically not integrated on the high resistivity silicon substrate to facilitate the use of different IF matching networks. The transition from the integrated coplanar stripline to the Duroid substrate, obtained by either using silver epoxy or bonding wires, is not important due to the low IF frequency used. For higher IF frequencies, the IF matching network can be integrated directly on the wafer by using a transition from coplanar stripline to coplanar waveguide [88, 89]. For array applications with severe space constraints on the matching network, a transformer can be integrated using a lumped capacitor and a lumped inductor [90]. Figure 3.7 shows such a matching network.

The diode of choice to be used in the mixer design is the UVA SC2T3 planar surface-channel GaAs Schottky diode [25] with a 2.5μm anode diameter and a 6-7fF zero-bias junction capacitance, C_{j0} (Figure 3.8). The diode ideality factor η is equal to 1.1-1.2. The diode saturation current I_s is 5×10^{-17} Amps. The Schottky diode is fabricated using a 1000Å-thick n^- layer (2×10^{17} /cm^3) and a 5μm-thick n^+ layer (5×10^{18} /cm^3). The surface-channel etched underneath the anode finger results in a reduction of the diode parasitic capacitance. The diode chip dimensions are

$400\mu m \times 140\mu m \times 55\mu m$ yielding approximately a 6-7fF parasitic capacitance (C_{pad}) between the contact pads and a 1.5-2fF parasitic capacitance (C_p) between the anode finger tip and the cathode [91, 92, 93].

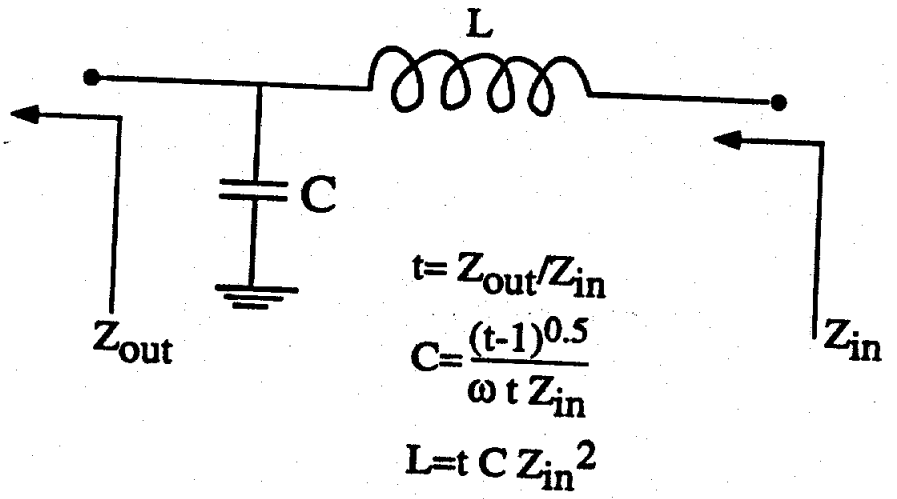

Figure 3.7: An IF matching network consisting of a lumped capacitor C and a lumped inductor L. Z_{out} is the mixer IF output impedance. Z_{in} is the input impedance of the matching circuit from the IF chain side (normally 50Ω).

The diode DC series resistance is 2.5-3Ω, but there are three components at RF which should be added to the dc value of the series resistance R_s. The first component is $R_{thermal}$ and it is due to the error in measuring the diode resistance at audio frequencies or dc, which results in a negative component caused by heating of the diode [84, 85]. In our case, $R_{thermal}$ is $\sim 1-2\Omega$ for a $2.5\mu m$ anode diameter [92]. The second component is due to the RF skin effect in the n^+ buffer layer and in the anode finger which results in an additional R_{skin} [94]. The skin depth δ_{skin} at 90GHz for n^+ ($\rho_{n+} = 10^{-3}$ Ωcm) is $5.3\mu m$ which is equal to n^+ layer thickness and hence at 90GHz, there is no additional skin effect resistance due to the n^+ layer. The anode finger which is $50\mu m \times 2.5\mu m \times 2.5\mu m$ results in an additional skin-effect resistance of $\sim 1.7\Omega$ at 90GHz ($\rho_{Au} = 2.2 \times 10^{-6}$ Ω−cm, and $\delta_{skin} = 0.25\mu m$). The third component results from the voltage dependence of the undepleted epitaxial material

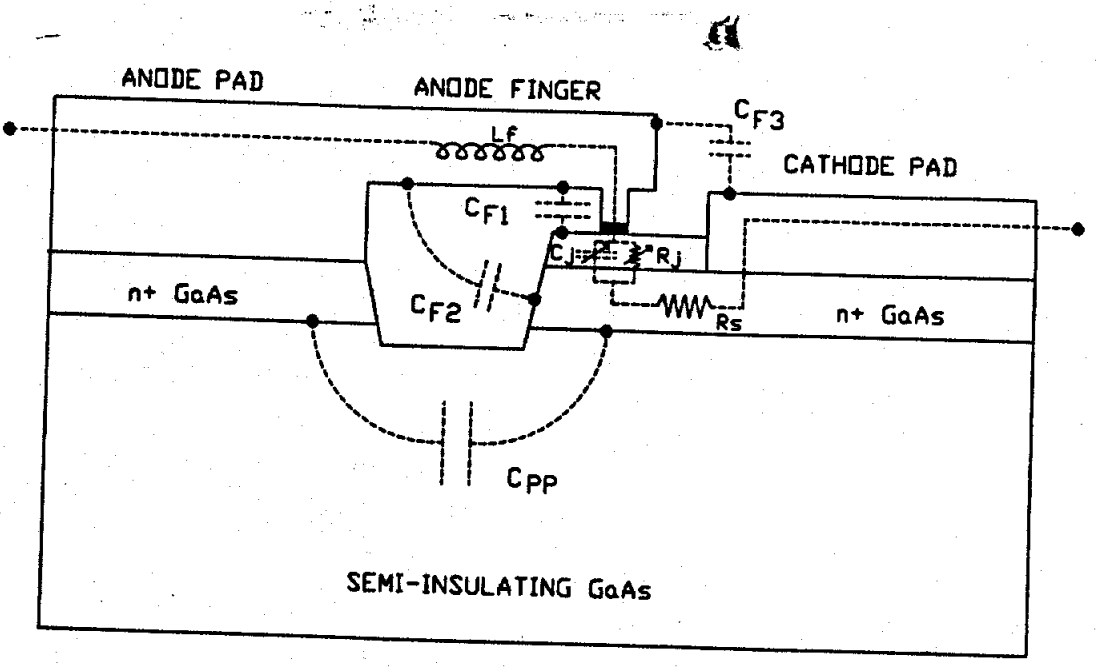

Figure 3.8: The geometry of the UVa planar surface-channel diode.

width. In this study, this third component is assumed negligible. Hence, the tota series resistance R_s of the SC2T3 diode is 6-6.5Ω. The finger inductance is assume negligible (~ 0.9pH at 90GHz) [95]. The SC2T3 diode has shown good performanc at millimeter-wave frequencies with RF embedding impedances around 50+j50Ω [96] This impedance could be approximately achieved at 91.4GHz (RF frequency) by usin a 0.38λ-long dipole positioned 0.38λ from the apex in a fully conducting horn cavity

Impedance measurements were done on a 35× scale model of the receiver structur at 2.55GHz (corresponding to a design frequency of 91.4GHz). The non-conductin wall A in the receiver structure was modeled using a wall of stycast ($\epsilon_r = 12$). Th measured input impedance was 85+j11Ω at the design frequency including the effec of the uncoated sidewall (wall A) and the V-shaped groove (wall B) (Figure 3.9) This input impedance drops to 75-j7Ω when a small stycast block is put at the apex of the feed-dipole to model the pad to pad parasitic capacitance (C_{pad}) of the GaA

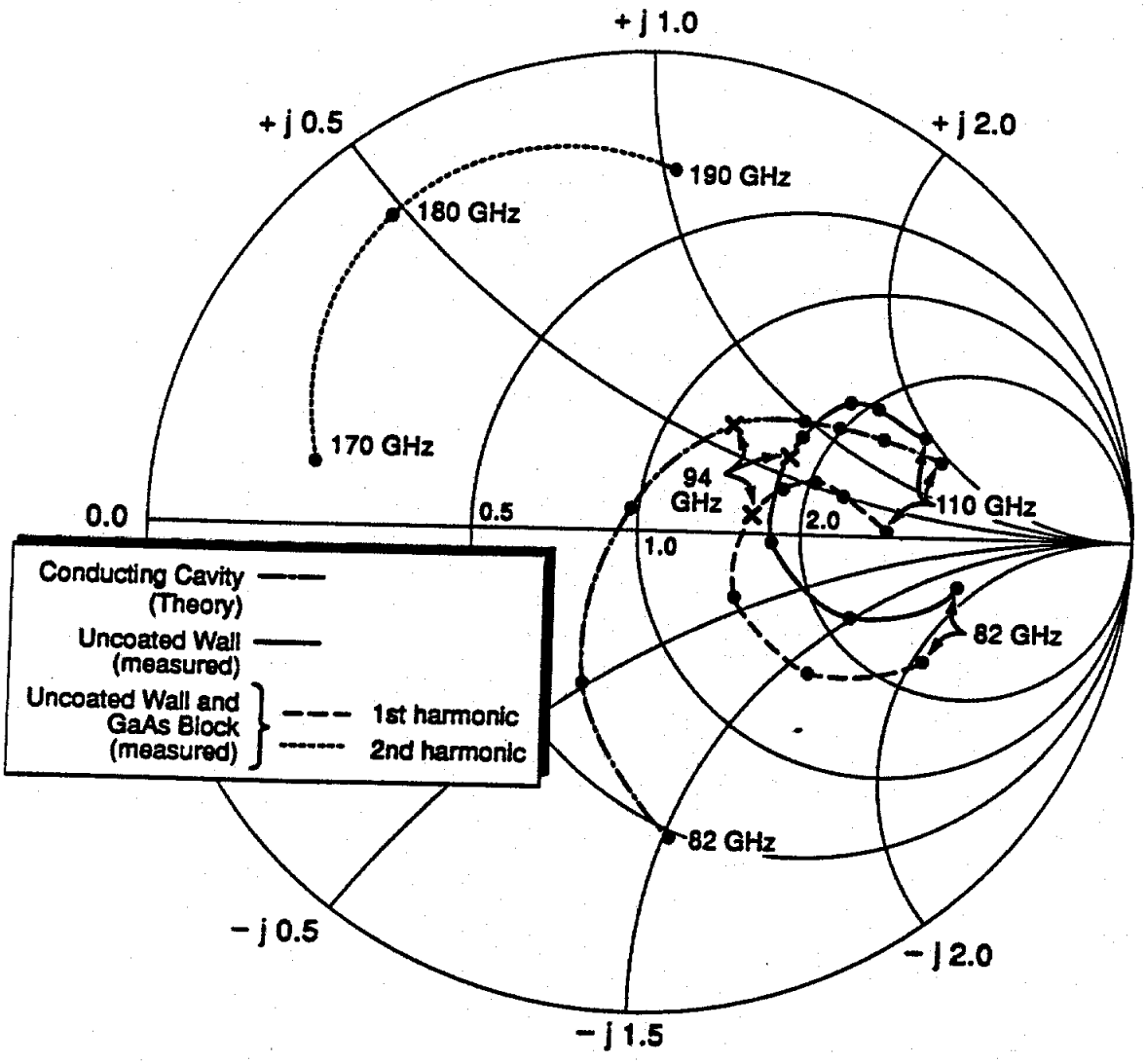

Figure 3.9: The measured feed-dipole impedance over the 82-110GHz and 170-190GHz range using the 2.55GHz microwave model of the integrated horn antenna receiver structure. The data points are 4GHz apart.

diode. Both measurements were sensitive to the feed geometry and were repeatable to $\pm 5 \pm j5\Omega$. Note that the impedance measurements include the effect of the low-pass filter which was also modeled. This is seen in the measured second harmonic (180GHz) impedances which are close to a short-circuit, and is due to the first lumped capacitor being $\lambda_{2f_o}/2$ away from the dipole apex at the second harmonic frequency.

3.2.2 Video Detection at 91.4GHz

A quasi-integrated horn antenna receiver was built at 90GHz and a UVA SC2T3 planar Schottky diode was epoxied at the feed-dipole apex (Fig. 3.10). Video detection measurements were done at 91.4 GHz by shining a plane wave with known power density on the quasi-integrated horn antenna and measuring the output detected diode voltage in a 120KΩ load using a lock-in amplifier. The RF plane wave is calibrated to $\pm 5\%$ using an Anritsu power meter and a standard gain horn. The video responsivity is defined here as the ratio of the detected low-frequency voltage across a 120kΩ load over the total RF plane wave power incident on the antenna aperture. This definition includes a 2.0dB loss resulting from the 63% aperture efficiency (coupling to a plane wave) of the quasi-integrated antenna [73, 55].

Figure 3.11 shows the theoretical and measured video responsivity versus bias current. The theoretical video responsivity was fitted to the measured video responsivity using the circuit parameters listed in Table 3.3. The fitted loss in walls A and B, and the fitted feed-dipole impedance including the effect of the pad-pad capacitance C_{pad} are very close to the measured values in the 35$\times$ scale model ($L_{walls}^{measured} = 1.1 - 1.2$dB and $Z_{dipole}^{measured} = 75 - j7\Omega$). In the theoretical model of the circuit (Figure 3.12), the parasitic capacitance C_p between the anode finger tip and the cathode has been included since it was not modeled in the microwave measurements. The 3fF predicted

Antenna			Diode				
$\epsilon_{aperture}$	$\epsilon_{lossinwalls}$	Z_{dipole}	R_s	C_j	C_p	ϕ_{bi}	η
-2.0dB	-1.15dB	70 -j15Ω	6Ω	6.5fF	3fF	0.9V	1.15

Table 3.3: The circuit parameters used to calculate the theoretical video responsivity at 91.4GHz (see text). Z_{dipole} includes C_{pad}, the parasitic capacitance between the contact pads.

value of C_p is higher than the estimated value of 1.7-2fF [92]. The increase in C_p might be due to the fact that the pad to pad capacitance was not perfectly modeled in the microwave model or there may be additional fringing capacitance between the anode finger tip and the cathode at high frequencies [97]. For the junction capacitance C_{j0}, an average value of 6.5fF was used for the 6-7fF range of value. The built-in-potential Φ_{bi} value of 0.9V was derived from the log I-V curve of the diode. A 6Ω value for the RF series resistance has been used which accounts, in addition to the dc resistance, for skin-depth losses and thermal time constant in the diode as discussed previously. It is seen that a very good agreement exists between theory and measurement over four decades of bias current. The peak video responsivity is 1140V/W which is equivalent to 1.62 V/(mW/cm^2) when referring it to the incident power density on the antenna aperture.

The responsivity can also be defined as the detected low frequency voltage into a 120KΩ load divided by the power available at the dipole terminals (70Ω RF source). This definition excludes the aperture efficiency loss (2dB) and the horn side wall loss (1.2dB), and results in a peak responsivity of 2350V/W which is competitive with whisker diodes at these frequencies.

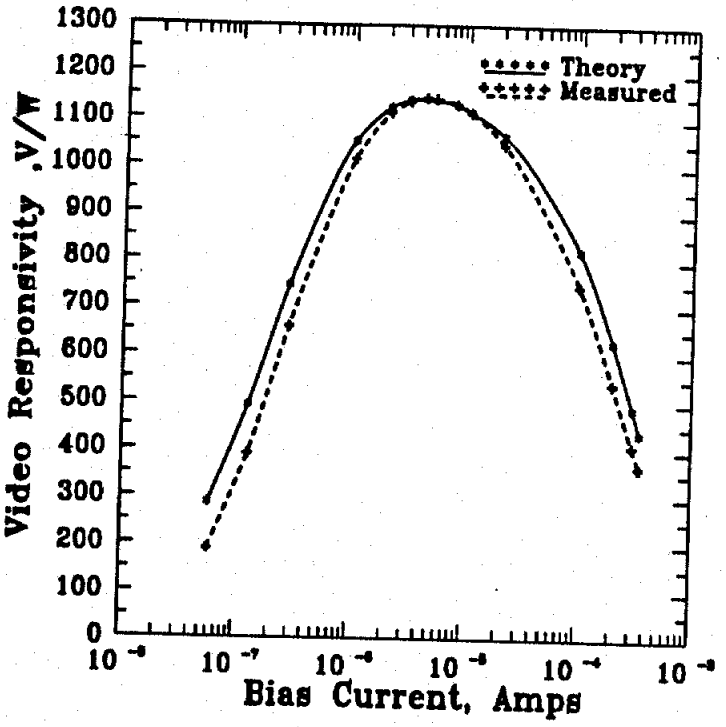

Figure 3.11: The theoretical and measured video responsivity of the antenna-mixer versus bias current at 91.4GHz.

3.2.3 Theoretical Analysis of the Mixer Performance

The mixer theoretical performance was analyzed using the reflection algorithm developed by Kerr et al. [98] for determining the steady-state conductance and capacitance waveforms for a diode given a certain dc bias, LO power level and the LO embedding impedances at the fundamental and harmonic frequencies. After the large signal analysis, the method described in [84, 85] is used to determine the small-signal properties of the mixer which results in the calculation of the mixer noise temperature and conversion loss as functions of the RF embedding impedances at the fundamental and harmonic sideband frequencies. The small signal analysis includes the effects of nonlinear diode junction capacitance and resistance as well as shot and thermal noise generated in the diode which predominate in room-temperature mixers. The large signal and small signal analysis are done using a computer software provided to us

by Prof. Maas [99].

The analysis is done for LO and RF frequencies of 90GHz and 91.4GHz, respectively. In our analysis, the embedding impedances at the first two LO harmonics (ω_{LO} , ω_{2LO}) and the first two harmonic sidebands pairs ($\omega_{LO} \pm \omega_{IF}$, $\omega_{2LO} \pm \omega_{IF}$) are considered because they are the most important in deciding the mixer performance [84, 85, 86]. All embedding impedances at higher harmonics are assumed to be short circuits due to the parasitic capacitance of the diode. The embedding impedance values at the RF frequencies (USB and LSB) are equal to the measured impedances at that frequency from the microwave model (figure 3.9) in parallel with a capacitive reactance due to C_p ($1/(jC_p\omega)$, C_p=3fF) as seen in figure 3.12. Table 3.4 shows the mixer theoretical performance for the UVA SC2T3 diode for an LO frequency of 90GHz, an RF frequency of 91.4GHz, a dc bias of 0.64V (I_{dc} = 1.4mA) and an available LO power at the dipole terminals of 1.6mW. The diode parameters used in this analysis are the one used in the calculation of the theoretical video responsivity (Table 3.3).

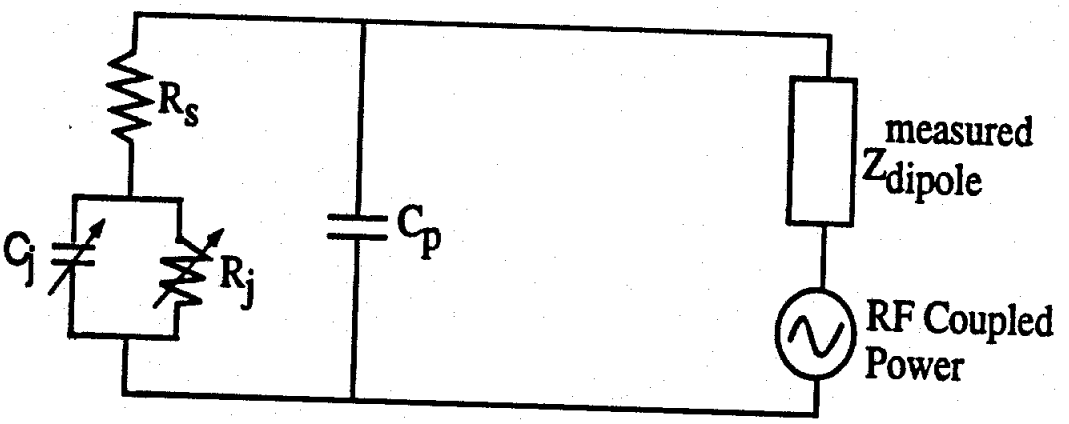

Figure 3.12: The equivalent RF mixer circuit. Note that C_{pad} is taken into account by the impedance measurements at the antenna terminals.

It is seen that a minimum SSB conversion loss of 5.4dB is achievable without a matching network, and the SSB conversion loss remains under 7.0dB over a 20%

f_{LO}(GHz)	90	
f_{RF}(GHz)	91.4	
LO embedding imp. (Ω)	90GHz	180GHz
	67-j27	7+j31
RF embedding imp. (Ω)	88.6GHz	91.4GHz
	64-j41	72-j16
RF embedding imp. (Ω)	178.6GHz	181.4GHz
	7+j26	6+j21
$Z^{in}_{diode,RF}(\Omega)$	80-j25	
$Z^{in}_{diode,LO}(\Omega)$	76-j58	
$Z^{out}_{diode,IF}(\Omega)$	105+j6	
Diode SC2T3 SSB Conversion loss (dB)	5.4	
Diode SC2T3 SSB mixer temperature (K)	480	
Diode SSB Conversion loss (dB) over 20% BW	5.0-7.0	

Table 3.4: The mixer theoretical performance of the UVA SC2T3 diode (2.5μm anode diameter) for a dc bias of 0.64V and an available LO power at the dipole terminals of 1.6mW.

bandwidth. The RF mismatch between the diode and the dipole at 91.4GHz is about 0.5dB. This can be eliminated by choosing a longer dipole in the pyramidal horn cavity. The embedding impedances at the second harmonic (178.6GHz, 180GHz, and 181.4GHz) are close to a short as expected. An improvement of 0.2-0.3dB in mixer performance can be obtained with a lower dc bias voltage, but at the expense of higher IF impedances which are hard to match to 50Ω over a wide IF bandwidth. The conversion loss can also be improved with higher LO power levels but at the expense of increasing the mixer noise temperature.

3.2.4 Quasi-Optical Measurement Set-up Design

A quasi-optical set-up has been designed to couple the RF and LO signals into the quasi-integrated horn antenna receiver using Gaussian-beam optics. The system shown in figure 3.13 has been designed for 90GHz. A WR-10 standard gain horn is used for coupling the LO power from a Gunn oscillator source. From the dimensions of the standard gain horn and using the application note [100], the minimum waist w_o^{LO} of the LO horn is 8.27mm at 90GHz. The beam waist w_o is the minimum beam radius of the fundamental Gaussian mode, and can be seen as the point from which a Gaussian beam is launched or to which it converges. At any point in the system, the beam radius w(z) of the fundamental Gaussian beam corresponds to the circular waist at which the power density in the fundamental gaussian mode beam drops to -8.7dB. The circular waist with a radius of $2w(z)$ corresponds to a power level of -35dB and presents a safe criteria for truncating the Gaussian beam. The system was designed so that any point z in the system, no Gaussian beam is truncated with a diameter less than $4w(z)$ so that to ensure propagation of essentially pure Gaussian beams and proper performance of the finite diameter focusing elements [10]. The beam

waist of the quasi-integrated horn antenna $w_o^{receiver}$ at 90GHz is estimated using the asymptotic angle of growth of the beam radius at large distances from the beam waist, which corresponds to the far-field region of the antenna [10], and is given by:

$$tan(\theta_{w_o}) = \lambda/\pi w_o \tag{3.1}$$

where θ_{w_o} corresponds to the -8.7dB angle in the antenna far-field patterns (considering symmetrical patterns). From the measured patterns at 90GHz (Fig. 3.2), $\theta_{w_o} = 16°$ and results in $w_o^{receiver} = 1.11\lambda = 3.7$mm at 90GHz. The horn beam waist is located at its phase center which is 1.45λ from its aperture for the case of the 20dB quasi-integrated horn antenna [55].

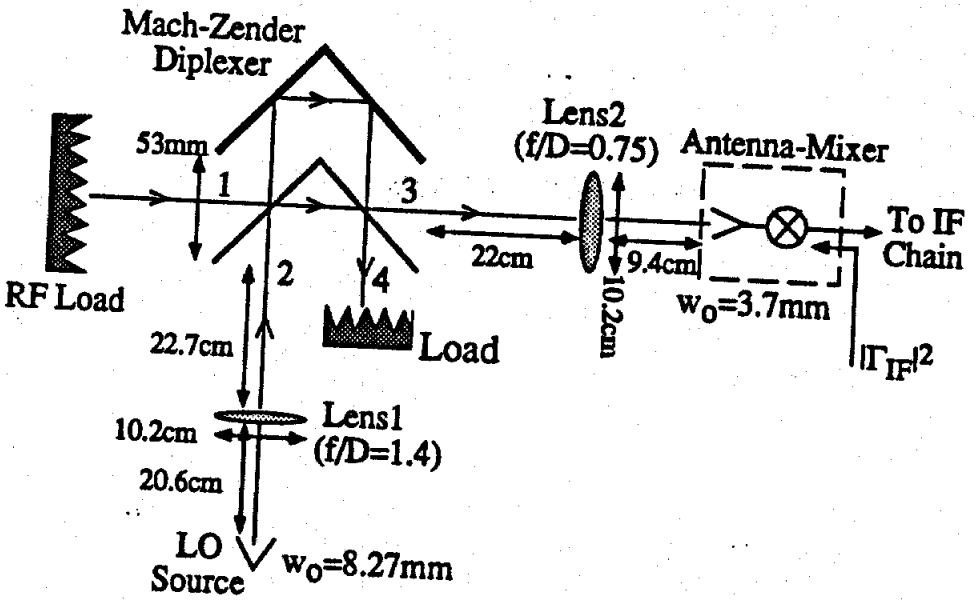

Figure 3.13: The quasi-optical set-up used in the measurement of the quasi-integrated horn antenna receiver performance. The design frequency is 90GHz.

As seen in figure 3.13, the power in the LO Gaussian beam is converged to the quasi-optical diplexer using a dielectric lens (lens1) with a power taper at its edges of

-35dB as discussed previously. The RF and LO beams at the output of the diplexer are coupled to the receiver using a dielectric lens (lens2) which also has a minimum taper of -35dB at its edges. An important design consideration is the position and width of beam waist inside the quasi-optical diplexer. As discussed by Erickson in [101], the converging minimum beam waist from lens1 is placed in the center of the interferometer, and this results in the smallest interferometer size. The size of this beam waist is given by equation B.13 (appendix B) and results in the minimum diffraction loss when combining the undelayed beam and the delayed beam at the output of the interferometer [10] (figure 3.14). In the case of double sideband (DSB) measurements, the path length difference Δ used in equation B.13 is equal to $\lambda_{IF}/2$. At 90GHz and for an IF frequency of 1.4GHz, $w_o^{diplexer}$ should be greater than 16.9mm to result in a diffraction loss of less than 0.09dB.

In our set-up, a Mach-Zender interferometer is used for diplexing (Appendix B). Before setting a beam waist of 16.9mm at the center of the interferometer, we have to make sure that there will not be any beam truncation inside the interferometer due to its dimensions. The output port 3 has a diameter which is limited by the separation between the corner mirror and the beam splitters, and in the case of DSB measurements and an IF frequency of 1.4GHz, $d = \lambda_{IF}/4 \simeq 53.6mm$ (Fig. 3.14). As discussed previously for the proper Gaussian beam propagation, the output and input ports diameters should be greater or equal to $4w$ where w is the beam radius at the output and input ports. For d=53.6mm, the beam radius at the output port cannot be larger than $d/4 \simeq$ 13mm without blockage of the beam. This sets the beam waist size at the center of the interferometer in our design to 13mm and will result in an increase in the diffraction loss (this is presented in the next section).

The quartz plates used as beam splitters in the Mach-Zender interferometer are 49

mils thick, and have a 50% reflectance for a vertically polarized wave incident at an angle of 45° to the normal to the plate (Appendix B). The resulting response of the diplexer is shown in figure B.2. The insertion loss in the LO path at the LO frequency of 90GHz (path 2→3 in fig. 3.13) is 0dB theoretically, and increases to 0.3dB and 0.08dB at 82GHz and 112GHz, respectively, due to the change in the reflectance of the quartz plates over the frequency range of measurements (82-112GHz) (Appendix B). Note, as discussed in appendix B, the change in the reflectance value does not introduce any insertion loss in the sidebands path at the image and signal frequencies (path 1→3).

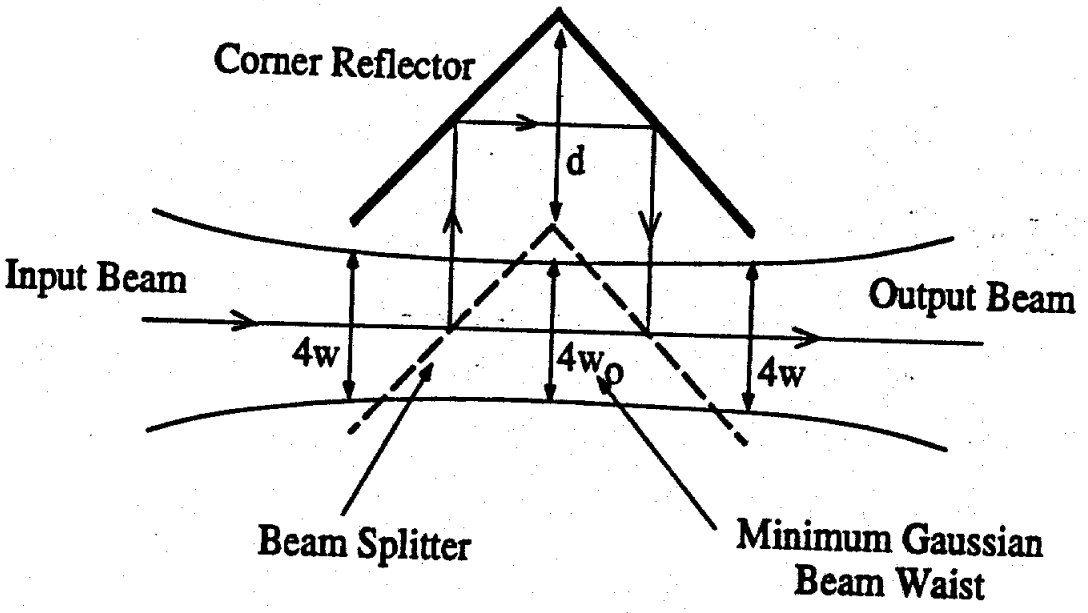

Figure 3.14: A Mach-Zender interferometer.

The system geometry can now be designed knowing the beam waists of the LO horn (w_o^{LO} =8.27mm) and the receiver horn ($w_o^{receiver}$ =3.7mm), and the beam waist at the center of the diplexer (13mm by geometrical constraints). Using the "thin lens" approximation formulas for Gaussian beam optics discussed in [10], we can find the size and the f/D number for lens1 and lens2, and the appropriate distances between

all the quasi-optical components which will result in minimum loss and minimum truncation of the signal beam through its path (-35dB tapering at the edges of the lenses). The resulting system, designed for 90GHz, is outlined in detail in figure 3.13. The two lenses are made up of teflon and lens1 is grooved to reduce reflections of its surface (both lenses are 10.2cm in diameter with focal distances of 14.22cm for lens1 and 7.62cm for lens2).

3.2.5 Receiver Measurements

DSB receiver measurements were done over the 82-112GHz range. In DSB operation, the mixer is assumed to have equal responses at both sidebands, and the mixer output noise temperature is generated equally from both sidebands. At each frequency, the distances between the lenses and the diplexer are varied empirically around the designed value at 90GHz in order to maximize the received LO signal by the receiver. This can be seen either by reducing the LO power, using the diode as a video detector, and maximizing the detected signal on the lock-in amplifier, or by pumping the diode with LO power and maximizing the dc rectified diode current on the current meter.

The beam waist size at the center of the diplexer is set always around 13mm at each measurement frequency. The optimum response of the Mach-zender interferometer corresponding to at least 20dB suppression of the LO signal at the upper and lower sidebands frequencies (Fig. B.2) is obtained by setting the half path length difference d to $\sim \lambda_{IF}/4$ (DSB operation) and then slowly varying d in order to maximize the dc rectified diode current. This is why, as discussed in Appendix B, at each measurement frequency f_{LO}, the IF frequency is not exactly 1.4GHz but is close to this value and related to f_{LO} by: $f_{LO}/f_{IF} = 2n$, where n is an integer. This is valid for DSB operation

and for the case when port 2 of the diplexer is used for the LO signal, port 1 is used for the RF and image signals, and port 3 is the output port where all the signals are combined (Fig. 3.13). Port assignments and path responses of the Mach-zender interferometer are discussed more in Appendix B.

The DSB receiver measurements were done using the standard hot/cold load method [102, 103]. The RF load, which is a black-body absorber [104], is directly placed at port 1 of the interferometer, so that its output noise power at both sidebands frequencies fills up the beam of the receiver antenna. The RF load is used at room temperature (T_H= 295K) and dipped in liquid nitrogen (77.3K). However, the cold load temperature T_C used in the calculations to determine the receiver performance is 85K and not 77.3K because the load material is not truly black (temperatures as high as 95K hav been quoted [12]).

As discussed previously in the mixer design, a microstrip line over a Duroid substrate ($h_{substrate}$ = 45mils, $\epsilon_r = 2.33$) is used to match the mixer IF output impedance to 50Ω. The predicted 1.4GHz IF output impedance from mixer theory (Table 3.4) is around 105Ω, and a 70Ω quarter-wave transformer is used as an IF matching network. The output of the IF matching network is fed into the IF chain shown in figure 3.15. The 10dB coupler used at the beginning of the IF chain is used for measuring the IF power reflection coefficient $|\Gamma_{IF}|^2$ at the output of the mixer. A calibrated and matched noise source is connected to the coupled port of the 10dB coupler and is turned off during receiver measurements. The load connected to port 2 of the isolator is cooled in liquid nitrogen. The temperature of this load T_{iso}^L is 85K assuming a slight increase in temperature due to the warm coaxial cable connecting the actual cooled load to the isolator port. The resulting IF chain has a gain of (G_{IF}) 92dB and a noise temperature (T_{IF}) of 128K at 1.4GHz, with a 100MHz bandwidth. The

output of the IF chain goes into a calibrated power meter at 1.4GHz.

After each receiver measurement, the IF power reflection coefficient $|\Gamma_{IF}|^2$ is measured using the following way [105]:

- For the same LO power level and dc bias used for the receiver measurement and with the noise source turned OFF, the IF power read on the power meter is recorded ($P_{IF}^{noise,OFF}$).
- For the same LO power level and dc bias used for the receiver measurement and with the noise source turned ON, the IF power read on the power meter is recorded ($P_{IF}^{noise,ON}$).
- The LO power and diode dc bias are turned off, and the noise source is turned ON. The mixer diode looks like an open circuit under this condition and will reflect all the power incident on the mixer port from the noise source. The corresponding IF power recorded is $P_{noise\ source}$.
- The IF reflection coefficient is then calculated as:
  $|\Gamma_{IF}|^2 = (P_{IF}^{noise,ON} - P_{IF}^{noise,OFF}) \ / \ P_{noise\ source}$.

In the remainder of this section, three different terms related to the measurements will be used, and each term represents a specific way of defining the system performance. In figure 3.16, the mixer conversion loss L_M includes the diode intrinsic conversion loss and the RF mismatch between the diode impedance and the feed-dipole impedance. The antenna-mixer conversion loss L_{A-M} includes the mixer conversion loss L_M, the Gaussian coupling efficiency loss, and any other loss in the antenna structure. The receiver conversion loss L_{rcvr} includes the antenna-mixer conversion loss, the IF power reflection loss $|\Gamma_{IF}|^2$, and the RF losses in the quasi-optical diplexer an

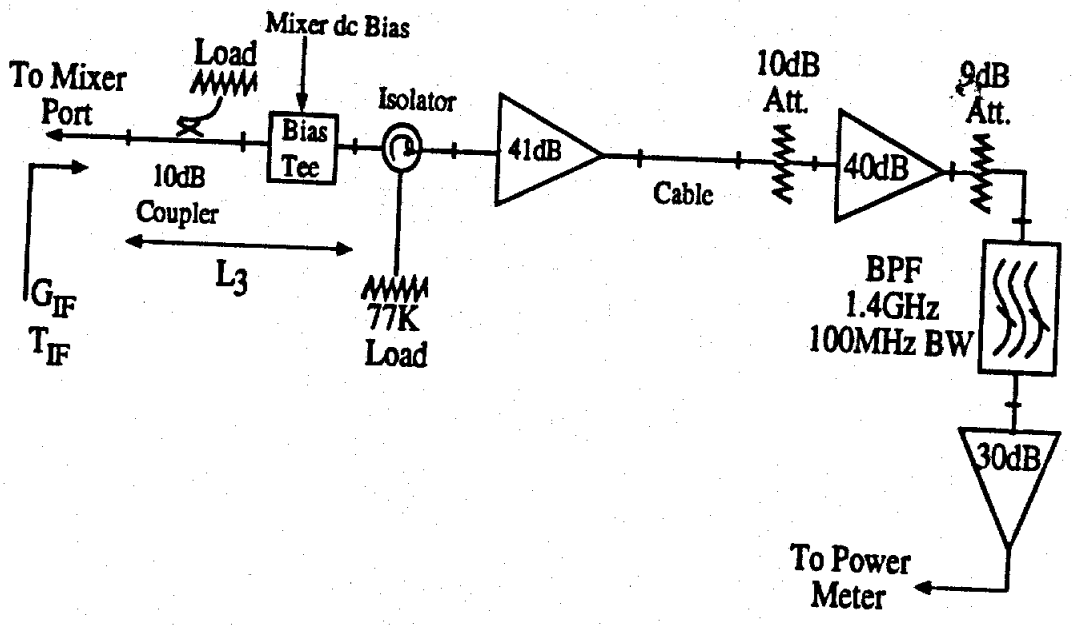

Figure 3.15: The IF chain used in the 90GHz receiver set-up. 92dB gain, 128K noise temperature, and 100MHz bandwidth.

in lens L2 in front of the receiver antenna. The receiver noise temperature includes also the noise temperature of the IF chain.

The receiver DSB temperature and conversion loss over the 82GHz to 112GHz range are shown in figure 3.17. At each frequency, the LO power and dc bias voltage were adjusted for minimum overall noise temperature T_{rcvr}. All the best data points are obtained for a 1.5-2mW LO power available at the dipole terminals and a 0.91V-0.92V dc bias voltage corresponding to a 1.2-1.5mA dc bias current. The LO power available at the dipole terminals has been estimated knowing the transmitted power from the Gunn source (which is measured using an Anritsu power meter) using a 70% Gaussian coupling efficiency for the standard pyramidal horn antenna [100], and estimating all the losses in the LO signal path till it reaches the dipole apex. The LO signal losses are presented in the following paragraph. The receiver performance calculations are done using equations C.15-C.17 (Appendix C). A minimum *receiver*

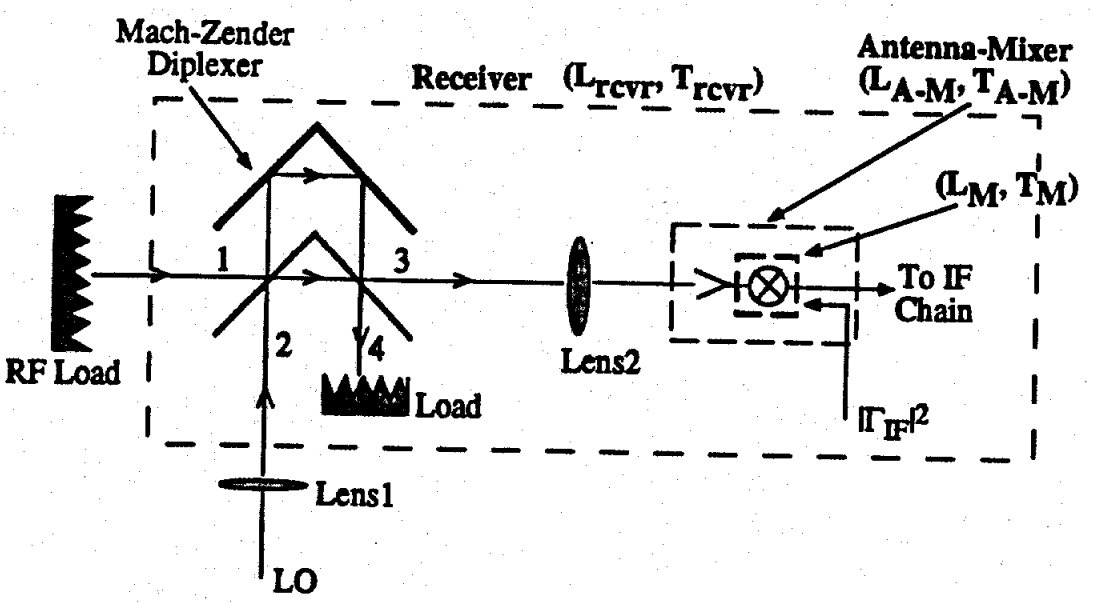

Figure 3.16: The system block diagram.

conversion loss of 6.5dB±0.3dB and noise temperature of 1600K±40K are obtained at 90GHz and 92GHz. This noise temperature includes the IF-chain noise temperature of 128K. As shown in figure 3.17, a *receiver* noise temperature of 1370K±10K was measured at 92GHz without the 10dB coupler in the IF chain (G_{IF} = 93dB, T_{IF} = 78K).

The loss in lens1 (L1) and the loss in lens2 (L2) (Fig. 3.13) were determined empirically to be 0.3±0.05dB and 0.5±0.1dB, respectively, over the frequency range of measurements. The diffraction loss in the diplexer at each measurement frequency for a beam waist size of 13mm inside the diplexer and a path length difference $\sim \lambda_{IF}/2$ for an IF frequency of 1.4GHz has been calculated using equation B.12. The resulting insertion loss $L_{1\to3}$ in the diplexer RF path at the sidebands frequencies varied between 0.3dB and 0.2dB for the frequencies between 82GHz and 112GHz. As for the LO path (2→3), the insertion loss $L_{2\to3}$ at the LO frequency consists of two

components:

- Diffraction loss, assumed to be equal to the diffraction loss calculated at the sideband frequencies (see above) since f_{IF} is small compared to the signal frequencies.

- Loss due to the change in the value of the reflectance R of the beam splitters with the change in the frequency of operation. This loss is less than 0.2dB over the range 82GHz to 112GHz ($0.4 < R < 0.6$). Note, this loss is not included in path 2→3 and path 1 →3 at the sideband frequencies since their responses are independent of R at those frequencies, as discussed in Appendix B.

Hence, the total insertion loss in the LO path at the LO frequency varied between 0.5dB and 0.4dB for the frequencies between 82GHz and 112GHz. The IF power reflection coefficient varied between 0.2dB and 0.7dB at the optimum bias points and LO power over the measurements frequency range. The insertion loss (L_3) at 1.4GHz in the IF chain between the mixer IF port and the isolator port is measured to be 1.05dB (including the bias-T and the 10dB coupler).

The DSB antenna-mixer conversion loss L_{A-M} and noise temperature T_{A-M} are calculated using equations C.18 and C.19, and a minimum antenna-mixer DSB conversion loss of 5.5dB±0.5dB is obtained at 90GHz and 92GHz, and a minimum antenna-mixer DSB noise temperature of 770K±50K is obtained over the 90GHz to 94GHz range (Fig. 3.18). The measured antenna-mixer DSB conversion loss and noise temperature over a 20GHz bandwidth (86GHz-106GHz) remain less than 6.3dB±0.5dB and 1000K±50K, respectively. With the 100MHz band pass filter in the IF chain was replaced by a 50MHz band pass filter, the DSB measurements at 92GHz were virtually the same.

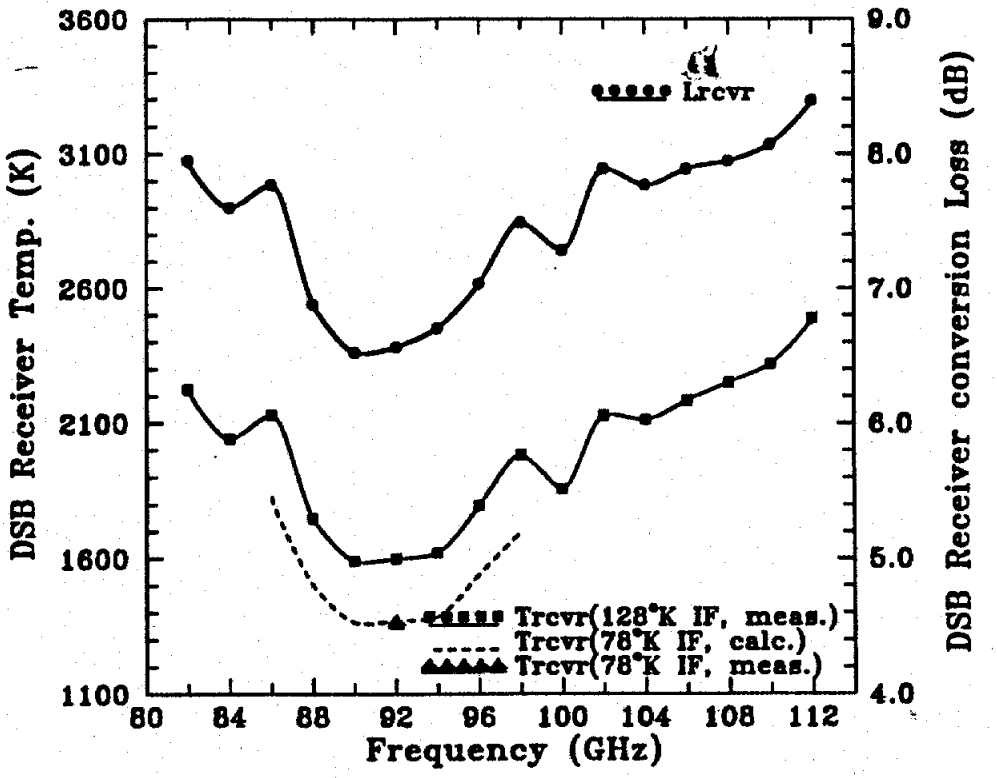

Figure 3.17: The measured receiver DSB noise temperature and conversion loss over the 82-112GHz range.

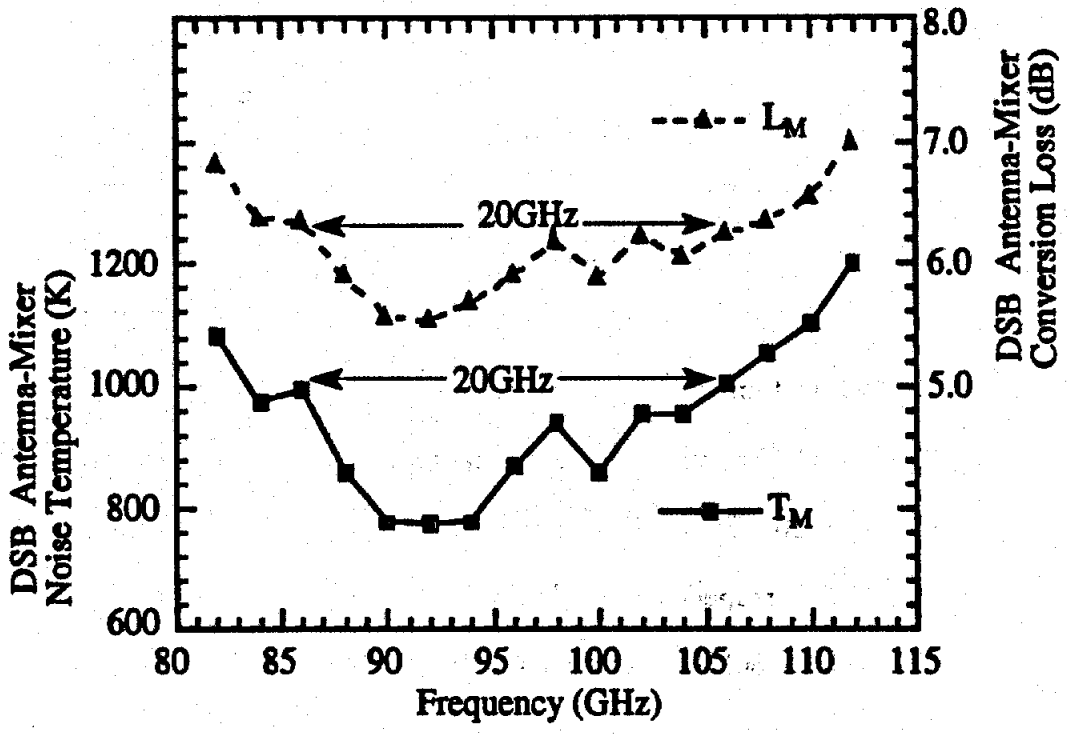

Figure 3.18: The measured antenna-mixer DSB noise temperature and conversion loss. The measured values remain less than 6.3dB±0.5dB and

The antenna mixer performance includes the drop in the Gaussian coupling efficiency of the quasi-integrated horn antenna at the low and high frequencies (Table 3.2) and the 1.1-1.2dB loss in the receiver structure as measured in the receiver microwave model and as predicted in the video detection theory (Table 3.3). At 90GHz, excluding the Gaussian coupling efficiency loss 0.13dB (97%) and the 1.1-1.2dB loss in the receiver structure, the resulting measured DSB mixer conversion loss and noise temperature are L_M = 4.2dB±0.5dB and T_M = 495K±50K. Hence, the measured DSB mixer conversion loss and noise figure (L_M^{meas} =4.2dB and NF_M^{meas} = 4.3dB) are only 1.8dB higher than the predicted theoretical DSB conversion loss and noise figure at 90GHz, shown in table 3.4, assuming equal mixer response in both sidebands (L_M^{theory} = 2.4dB and NF_M^{theory} = 2.6dB for DSB operation). We can see that the measured results are in close agreement with the predicted performance. The discrepancy between experiment and theory can be attributed to the following reasons:

- The discrepancy in the measured embedding impedances at the first and second harmonics between the microwave model of the receiver structure and the actual receiver at 90GHz.
- The effects of the embedding circuit, contributing noise from higher harmonic terminations [12].
- Power lost by conversion to other frequencies, where the terminating embedding impedances have real parts [85].

It is useful to derive the effective mixer diode temperature from the measured results at 90GHz, since it is an indication of the inherent noise characteristics of the diode and mixer environment. Assuming all losses are within the mixer diode itself and based on the attenuator noise model of the mixer described by Kerr [106], the effective

temperature is

$$T_{eff} = \frac{T_M^{meas,DSB}}{(L_M^{meas,DSB} - 1)} \tag{3.2}$$

which results in $T_{eff} = 300 \pm 25$K derived from the DSB mixer conversion loss of 4.2±0.5dB and noise temperature of 495±50K. For an idealized shot-noise limited mixer, where the diode series and parametric effects due to the diode nonlinear capacitance are negligible ($R_s = 0$, $C_j = Const$), and with higher harmonics reactively terminated so that no power is converted or generated by these harmonics, the idealized effective diode temperature is equal to $T_{eff}^{ideal} = \eta T_{physical}/2$ [106]. In this case, $\eta = 1.15$ and $T_{physical} = 295$K and therefore $T_{eff}^{ideal} = 170$K. Hence, the effective diode temperature of the 90GHz mixer diode is within a factor of 1.8 of the effective diode temperature of the idealized mixer using the same diode.

Single sideband (SSB) measurements for an LO frequency of 92GHz and an RF frequency of 93.4GHz were done by halving the interferometer path-length used in the DSB measurements and thereby tuning the interferometer as a single-sideband filter [10]. Hence, $\Delta_{SSB} = \Delta_{DSB}/2 = \lambda_{IF}/4$, resulting in $d_{SSB} = \Delta_{SSB}/2 = \lambda_{IF}/8$, which is equal to 26.8mm at 1.4GHz. This value of d, which also corresponds to the diameter of input port 1, results in the truncation of the signal beam at the - 9.2dB power level, assuming a 13mm beam waist at the center of the interferometer, as set in the DSB case. This truncation of power disturbs the propagation of the fundamental Gaussian mode and results in power loss in the RF path. To eliminate this RF loss, the interferometer is operated at a longer path length difference Δ_{SSB} which is set to $3\lambda_{IF}/4$ (K=2), instead of $\lambda_{IF}/4$ (K=1) (refer to Appendinx B). The resulting response of the interferometer corresponding to $d = \Delta_{SSB}/2 = 3\lambda_{IF}/8$ is shown in figure 3.19. Increasing the path length difference eliminates the truncation of the input beam, but results in an increase in the diffraction loss because the delayed beam travels a

large distance inside the interferometer before reaching the output port. However, a larger value of d allows the choice of a large beam waist inside the interferometer without fear of truncation at the output port. The diffraction loss is calculated using equation B.12 (Appendix B) for $f_{RF} = 93.4$GHz , $f_{IF} = 1.4$GHz, $\Delta = 3\lambda_{IF}/4$, and a beam waist size w_o set inside the diplexer of 17mm. The resulting diffraction loss is about 0.2dB.

Figure 3.20 shows the measured SSB antenna-mixer conversion loss (L_{A-M}) at 93.4GHz versus LO power available at the dipole terminals. For each LO power level, the DC bias voltage is adjusted to minimize the IF power reflection coefficient which was measured to be less than 0.3dB at optimum LO powers. A minimum SSB antenna-mixer conversion loss of 7.5dB±0.5dB was obtained for an available LO power between 1.3 and 2.5mW at the antenna aperture. Excluding the 1.2dB power loss in the antenna structure and the 0.13dB Gaussian coupling efficiency loss, the resulting SSB mixer conversion loss of 6.2±0.5dB agrees well with theory which predicts a 5.3dB SSB conversion loss (Table 3.4).

3.3 A 250GHz Quasi-Integrated Horn Antenna Receiver

A 20dB quasi-integrated horn antenna mixer was also designed at 250GHz with a design similar to the 90GHz mixer presented above. Figure 3.21 shows the measured patterns at the design frequency of 250GHz and at the edges of the ±10% bandwidth over which the receiver measurements were done (230GHz-280GHz). The E-,H-, and 45°-plane patterns are not perfectly symmetrical due probably to small alignment errors between the integrated section and the machined section. Also, as seen, there is an increase in the E-plane side-lobe level (-15dB) at 279GHz. Table 3.5 shows the theoretical gain and coupling efficiency from 222GHz to 279GHz of the 250GHz

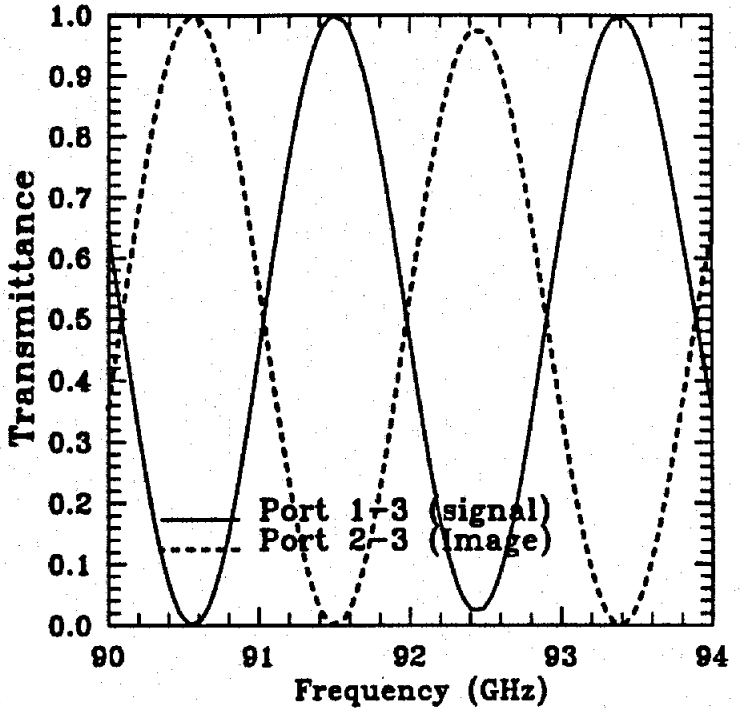

Figure 3.19: The ideal response of the Mach-Zender interferometer set for SSB operation with f_{signal} =93.4GHz and f_{LO} =92GHz (K=2, $d = 3\lambda_{IF}/8$).

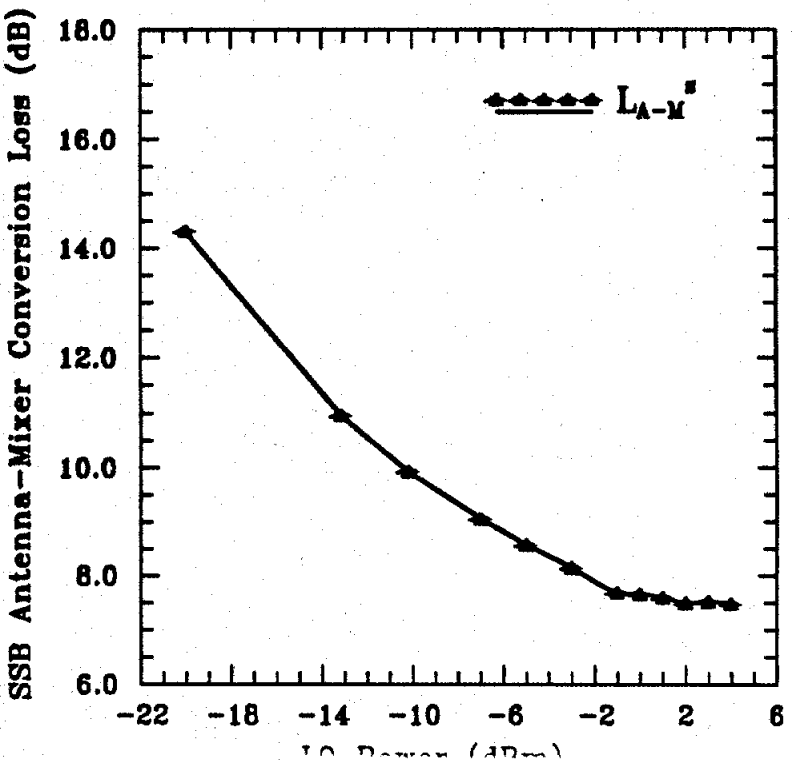

Frequency (GHz)	222	237	250	258	279
Gaussian coupling efficiency %	86	95	97	97	92
Gain (dB)	18.7	19.4	20.0	20.6	21.3

Table 3.5: The calculated gain and Gaussian coupling efficiency of the 20dB quasi-integrated horn antenna from 222GHz to 279GHz. The design frequency is 250GHz.

quasi-integrated horn antenna. As we can see, the 20dB quasi-integrated horn antenna shows a higher Gaussian coupling efficiency at 279GHz than at 222GHz.

The 250GHz receiver structure is shown in figure 3.22. The feed-dipole is positioned 0.38λ from the horn apex as in the 90GHz structure. The separation between the two strips of the CPS line on the high resistivity silicon wafer is 20μm rather than 40μm on the membrane in order to minimize radiation losses of the CPS line at 250GHz. The CPS line impedance is 240Ω on the membrane ($\epsilon_e = 1$) and 85Ω on the high resistivity silicon ($\epsilon_e \simeq (\epsilon_r + 1)/2 = 6.5$) (Fig. 3.23).

The height of the V-groove in wall-B is 140μm which seven times larger than the separation between the two strips of the CPS line integrated on the high resistivity silicon wafer (figure 3.23), and hence, the effective dielectric constant of the CPS line can still be assumed as $\epsilon_e = (\epsilon_r + 1)/2$. The cavity formed by the V-groove is small enough so that no higher-order modes are present at 250GHz. As seen in figure 3.21, the antenna far-field patterns are not severely affected by walls A and B. For a 1.1μm thick polyimide with $\epsilon_r = 4$, the metal-dielectric-metal (MIM) capacitor integrated on the membrane is 53fF (40μm$\times 190\mu$m) and the one integrated on silicon is 64fF (50μm$\times 170\mu$m). This results in a low pass filter with a -3dB corner frequency of 70GHz and a rejection of -26dB at 250GHz.

The mixer diode is the UVA SC1T4-S20 planar surface channel Schottky diode

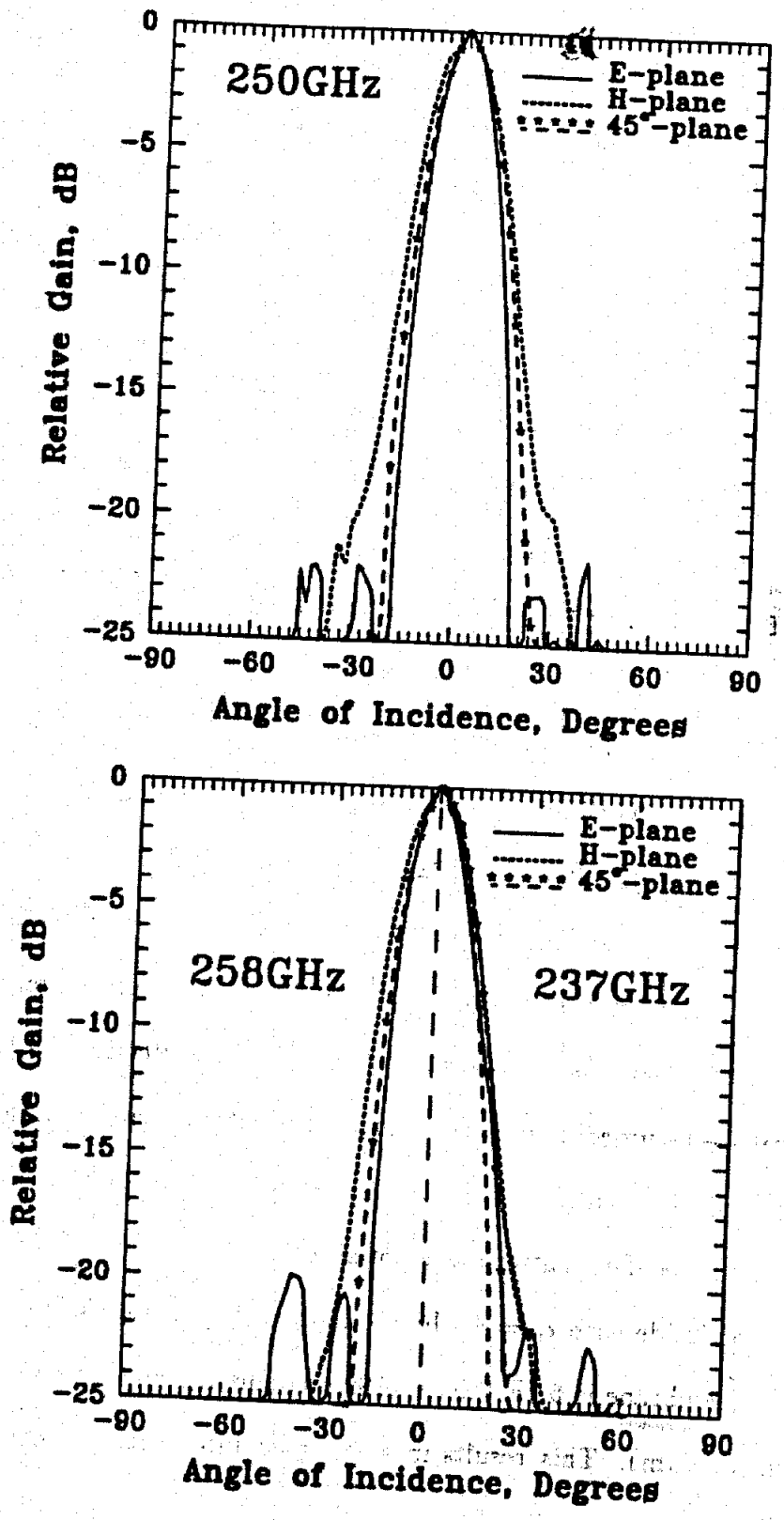

Figure 3.21: The measured E-, H-, and 45-° plane patterns of the quasi-integrated horn antenna at 250GHz (design frequency) (top) and 237GHz and 279GHz (bottom).

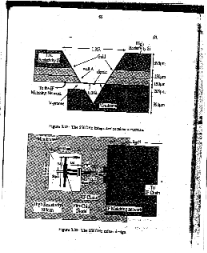

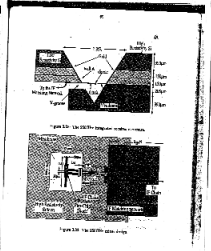

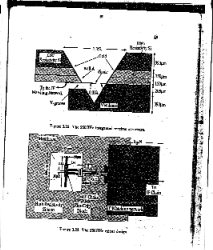

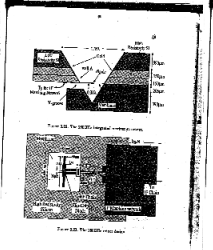

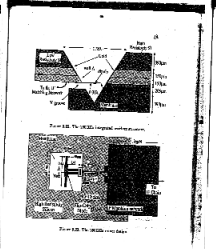

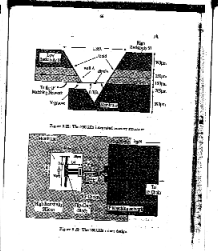

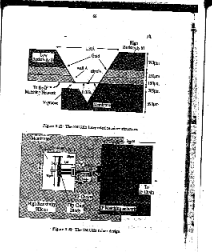

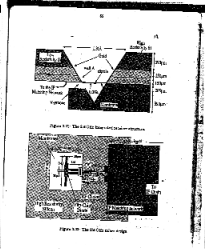

with a 1.3-1.4μm anode diameter and a 2-3fF zero-bias junction capacitance. The Schottky diode is fabricated using a 1000Å-thick n^- layer (2×10^{17} /cm^3) and a 5μm-thick n^+ layer (5×10^{18} /cm^3). The ideality factor is 1.15, and the dc series resistance is 10-12Ω. The diode saturation current I_s = 0.9-1$\times10^{-17}$. The series resistance R_s is expected to increase to 15-17Ω. This increase in resistance, as discussed before, includes the thermal component (about 1.5 Ω [92]), the skin effect in the n^+ buffer layer (1.3-1.5 Ω with $\delta^{n+}_{skin\ depth} = 3.1\mu$m) and the skin effect in the anode finger (1 − 1.2Ω). The diode chip dimensions are 210μm$\times$80μm$\times$50μm yielding approximately a 3-4fF parasitic capacitance (C_{pad}) between the contact pads and a 1.5-2fF parasitic capacitance (C_p) between the anode finger tip and the cathode [92, 91, 93]. The anode finger length is 20μm and results in a negligible inductance. The diode parasitic pad to pad capacitance is reduced by 1.5-2fF by chemically thinning the semi-insulating GaAs substrate to 25-30μm [92, 93]. The 25-30μm-thin diode is then mounted on the feed-dipole apex using silver epoxy.

In the 90GHz receiver design, we saw that it is always better to make the dipole more inductive in order to reduce the reactance induced by the diode parasitic capacitance. The dipole length in the 250GHz design is chosen to be 0.4λ. This results in a dipole impedance at 250GHz of 65+j25Ω, when measured in a microwave scale model of the receiver structure at 2.55GHz shown in figure 3.22. The measured dipole impedance includes the effects of the uncoated wall A, the V-groove in wall B, the stycast block on the dipole apex modeling the pad to pad parasitic capacitance of the 25-30μm thinned diode and the low pass filter.

Video detection measurements were done on a 250GHz quasi-integrated receiver from 230GHz to 280GHz using the same method described in the 90GHz experiment. The video responsivity is defined as the ratio of the detected low-frequency

voltage across a 120kΩ load over the total RF plane-wave power incident on the quasi-integrated horn antenna aperture. A 3mm×3mm large area bismuth bolometer is used to measure the incident power density on the antenna aperture [77]. The area of the bolometer is larger than $2\lambda \times 2\lambda$ at the measurement frequencies. The video responsivity varied around 500V/W or 91mV/(mW/cm^2) for a 3-6μA dc bias current from 230-280GHz. The variation in the data is due to the ±5% accuracy in the power measurements and the variation in the feed-dipole impedance. Excluding the 2.0dB loss resulting from the 62.5% aperture efficiency (coupling efficiency of the quasi-integrated horn antenna to a plane wave) and the 1.1-1.2dB RF-loss due to the uncoated wall A, the measurements result in a diode video responsivity of 1040V/W referred to the feed-dipole terminals. This is competitive with the performance of whisker-contacted diodes at 250 GHz in a WR-03 waveguide.

In the theoretical mixer analysis, and referring to figure 3.12, all the embedding impedances at the harmonics above the first harmonic are considered to be shorted. The embedding impedances at the LO, RF and image frequencies are assumed to be equal since the IF frequency is much smaller than the LO frequency. This embedding impedance is $65+j25\ \Omega$ in parallel with the reactance of C_p at 250GHz ($C_p = 4fF$ assuming 2fF between the anode finger tip and the cathode, and an additional 2fF to compensate for unmodeled capacitance and for fringing capacitance). The resulting embedding impedance at ω_{LO} and $\omega_{LO} \pm \omega_{IF}$ is $74-j6\ \Omega$. The resulting SSB theoretical conversion loss and noise temperature are 6.5dB and 1084K, respectively, for a dc bias current of 1.4mA and an available LO power of 1.5mW at the dipole terminals. This conversion loss includes a 0.7dB RF mismatch between the diode and dipole impedance. The mixer IF output impedance is around 150Ω and a $\lambda/4$ microstrip line matching network on an ϵ_r =2.2 Duroid substrate [87] with an impedance of 85Ω

was used as a matching network at 1.4GHz.

The 250GHz quasi-optical set-up is similar to the 90GHz set-up but with different distances between the quasi-optics and smaller lenses (figure 3.24). The beam waist at the center of the Mach-Zender interferometer is set to 13mm for 230-280GHz resulting in a diffraction loss less than 0.1dB. The LO antenna is a corrugated horn with a 10dB-beamwidth of 21.5° [107]. The beam waist of the LO horn w_o^{LO} at 250GHz is estimated to be 2mm using its far-field patterns [107, 10]. The beam waist of the 20dB quasi-integrated receiver, as shown previously, is equal to $1.11\lambda = 1.33$mm at 250GHz. Lens1 in the LO arm of the interferometer has an f/D number of 1.4 (D=6.35cm), and lens2 in front of the receiver has an f/D number of 0.85 (D=6.35cm). The lenses are made from teflon and are not grooved, which result in a reflection loss in addition to the absorption loss in teflon. The IF chain used in the receiver measurements is the same one used for the 90GHz receiver.

The double-sideband conversion loss and noise temperature of the antenna-mixer are measured using the hot/cold load method. They were done at room temperature and from 230GHz to 280GHz. At each frequency, the optimum LO power is approximately 2.2-2.5mW available at the quasi-integrated aperture, and the optimum dc bias current is 1.2-1.4mA. The LO power at the antenna aperture was estimated by measuring the transmitted power from the LO tripler source using the large-area bolometer technique described in [77], and reducing it by the RF loss in the quasi-optical path between the LO port and the integrated receiver.

During measurements, the loss due to the non-zero IF reflection coefficient at the mixer output port was between 0.5dB and 0.7dB. The RF losses (L_2) in the f/0.85, 6.35cm diameter teflon lens in front of the receiver are estimated to be 0.3dB due to loss resulting from normal incidence reflection at both surfaces of the lens [108]

($\epsilon_r^{teflon} = 2.07$) and 0.5-0.6dB due to absorption loss in teflon over the frequency range ($\alpha_{absorption} = 0.045$ Np/cm at 230GHz, $\alpha_{absorption} = 0.057$ Np/cm at 280GHz [66, 109]). The RF diplexer loss $L_{1\to3}$ in the signal and image path at both sidebands frequencies is estimated to be 0.1-0.2dB, which includes diffraction loss and dielectric losses in the quartz beam splitters. The insertion loss $L_{2\to3}$ in the diplexer LO path at the sidebands frequencies is assumed to be 20dB. The IF mismatch and RF path losses are removed from the receiver measurements (appendix B), and the double sideband antenna-mixer conversion loss and noise temperature are shown in figure 3.25.

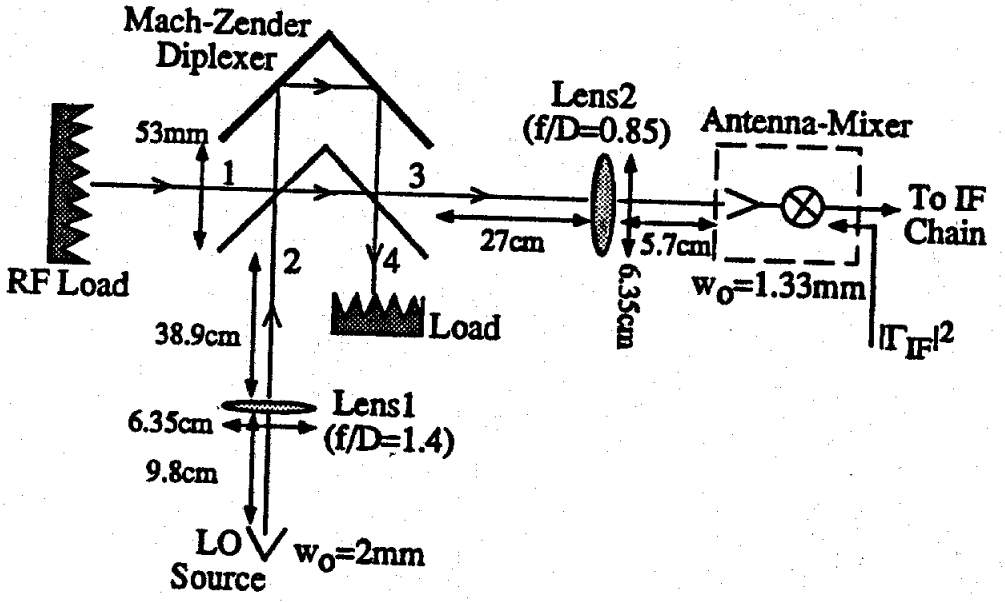

Figure 3.24: The 250GHz receiver quasi-optical set-up.

The conversion loss includes the antenna Gaussian coupling loss, any power loss in the antenna-mixer structure, the RF mismatch between the feed-dipole and diode impedances, and the diode intrinsic conversion loss. A minimum antenna-mixer DSB conversion loss of 7.1dB±0.5dB and noise temperature of 1405K±70K are obtained

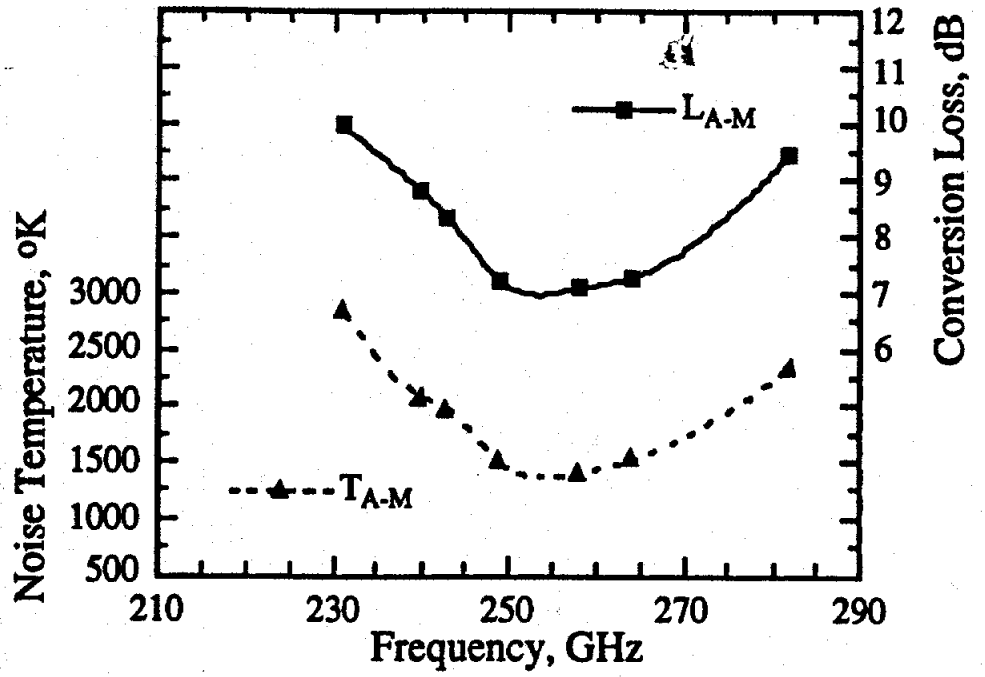

Figure 3.25: The measured antenna-mixer DSB noise temperature and conversion loss over the 230-280GHz range.

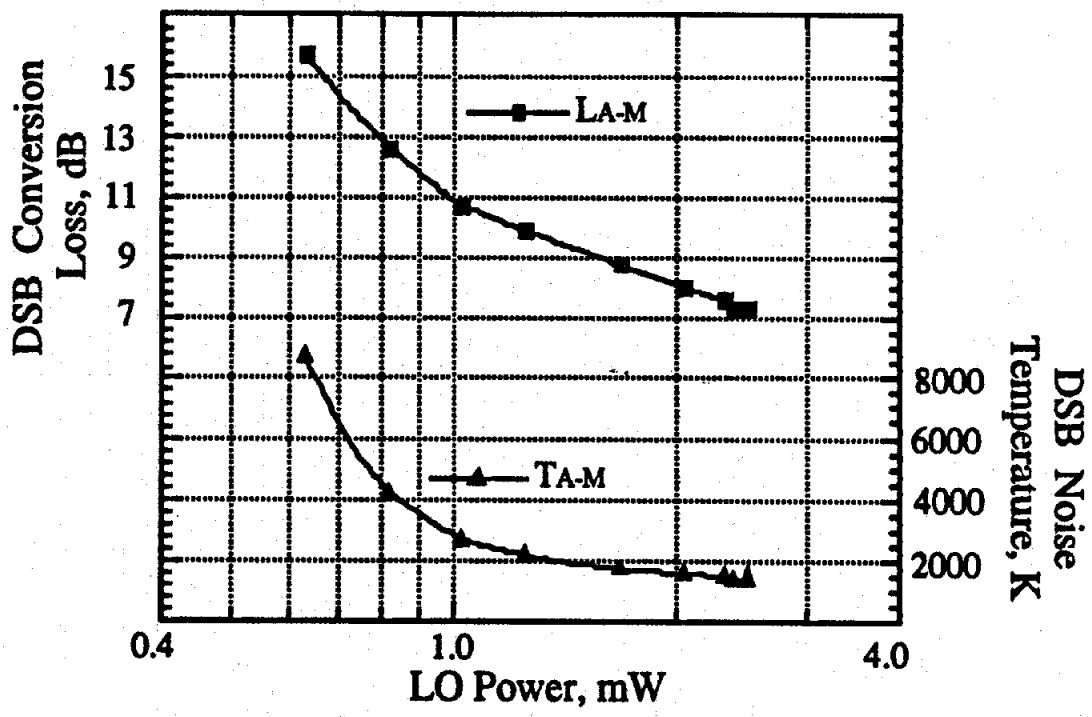

Figure 3.26: The measured 250GHz antenna-mixer DSB noise temperature and conversion loss vs. LO power available at the quasi-integrated horn antenna aperture.

at 258GHz. It is seen that the receiver has a comfortable 10% bandwidth. The measured DSB noise-temperature and conversion-loss versus LO power are shown in figure 3.26 and it is seen that the measurements level-off at an LO power of 2-2.5mW available at the antenna aperture (the available LO power at the dipole terminals is 1.3-1.5dB lower due to RF loss in the walls (1.2dB) and Gaussian coupling efficiency loss (0.1-0.3dB)).

Excluding the 1.2dB loss in the receiver structure and the 0.13dB Gaussian coupling efficiency loss (97%) at 250GHz, the resulting DSB mixer conversion loss and noise temperature between 250GHz and 258GHz are L_M = 5.8dB±0.3dB and T_M = 980K±60K. At 250GHz, the measured DSB mixer conversion loss and noise figure ($L_M^{meas} = 5.9dB$ and $NF_M^{meas} = 6.5dB$) are only 2.2dB higher than the predicted theoretical DSB conversion loss and noise figure at 250GHz, as discussed before, assuming equal mixer response in both sidebands ($L_M^{theory} = 3.5dB$ and $NF_M^{theory} = 4.5dB$ for DSB operation).

As discussed before, the discrepancy between the theoretical and measured conversion loss is attributed to the non-zero impedance of the higher order harmonics, higher RF mismatch than predicted and resistive loss in the junction [85]. As for the noise, the increase in the series resistance of the diode at high frequencies increases the generated thermal noise [84]. Also, the non-zero impedance of the higher harmonics tend to increase the correlated shot-noise components from these harmonics [110, 111]. Another noise component is hot-electron noise which should be considered in the case of small anode diameters [13]. Small anode diameters result in high current densities and therefore high electric field occurring in the undepleted active portion of the device during strong forward operation. These high fields accelerate the electrons through the undepleted epitaxial material, causing higher electron average

temperature than lattice temperature [112].

At 258GHz, the effective diode temperature assuming the attenuator noise model for the mixer diode, as done in the 90GHz case, is equal to 340K which is a factor of 2 larger than the effective diode temperature of the idealized shot-noise limited mixer using the same diode. The antenna-mixer DSB performance at 258GHz (LO) was measured for IF frequencies between 1.2GHz and 1.6GHz using a YIG-tuned filter in the IF chain. It is seen that the mixer has a comfortable 300MHz IF bandwidth with a simple $\lambda/4$ matching network designed at 1.4GHz (figure 3.27).

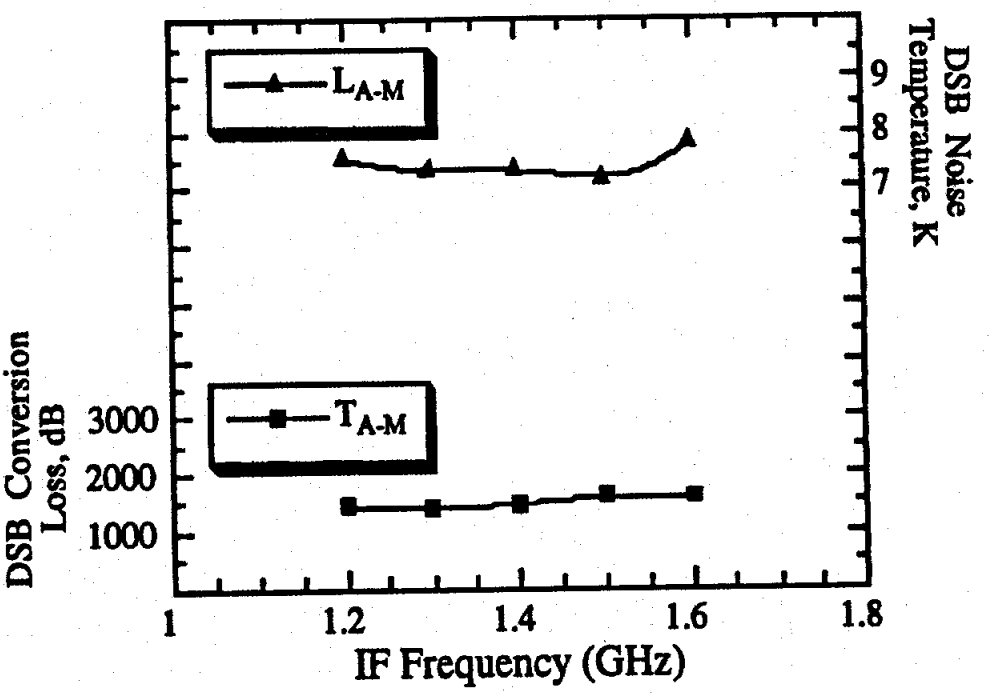

Figure 3.27: The DSB antenna-mixer conversion loss and noise temperature versus IF frequency (f_{LO} = 258GHz, and the IF matching network designed at 1.4GHz).

3.4 A 330GHz Quasi-Integrated Horn Antenna Receiver With A New Design

In the previous sections of this chapter, the design and measurements of a 90GHz and a 250GHz quasi-optical planar receivers based on the 20dB quasi-integrated horn antenna were presented. In this section, the design of the quasi-integrated receiver structure has been modified for the following reasons:

1. To reduce the power loss in the uncoated membrane wafer sidewall A near the CPS (IF) line integrated on the membrane wafer.

2. To eliminate the non-practical step of evaporating gold on the three membrane-wafer sidewalls.

3.4.1 Receiver Structure and Mixer Designs

The UVa SC1T4-S20 planar diode used in the 250GHz receiver is also used for the 330GHz mixer design. The diode performs well for RF embedding impedances around (60-70)+j(50-60)Ω, as predicted from mixer theory. The impedance of a dipole 0.4λ long and positioned 0.38λ from the horn apex is 65+j25Ω as measured in a microwave model of the 250GHz design (the measured impedance includes the effect of the diode block on the dipole-apex, the low pass filter in the mixer circuit and the receiver structure). Note that the measured dipole impedance is always in parallel with an unmodeled capacitance (3-4fF for the SC1T4-S20) which tends to lower the inductive reactance and increase the resistance real part of the equivalent RF embedding impedance. Hence, in the 330GHz design, there is a need for a dipole with a higher inductive reactance to compensate for the increased capacitive reactance of the diode. This can be done by increasing the length of the dipole or changing the dipole position. However, there are two limitations on increasing the dipole length:

1. The physical size of the membrane on which the dipole is integrated.
2. The real part of the dipole impedance increases also with increasing the dipole length and this results in a higher diode-dipole RF mismatch.

Moving the dipole away from the horn apex does not improve the RF match between the SC1T4-S20 diode and the dipole because of the increase in the dipole radiation resistance value (Figure 2.6). As a result, the dipole is kept positioned 0.38λ from the horn apex, but its length is increased to about 0.43λ. As seen in figure 3.28, the first part of the dipole is 70μm long and 40μm wide and corresponds to the size of the diode contact pads. The dipole width is then reduced to 20μm in order to increase the dipole inductance.

The low pass filter is designed in a similar way to the 250GHz design, but in the 330GHz design, sputtered SiO_2 is used as the dielectric layer in the integrated capacitors. The advantage of sputtering SiO_2 (ϵ_r =3.86) is that it exhibits low loss at submillimeter-wave frequencies and it is possible to obtain very thin dielectric layers with this process. This results in smaller integrated capacitor dimensions. The sputtered SiO_2 layer is 3500Å-thick, and the capacitor integrated on the membrane is 45fF with dimensions of 20μm$\times 124\mu$m, and the capacitor integrated on silicon is 75fF with dimensions 40μm$\times 94\mu$m. This results in a low pass filter with -3dB corner frequency of 97GHz and a rejection of -29dB at 330GHz.

As seen in figure 3.28, V-trenches have been etched 50μm to 75μm away from the membrane sidewalls, and coated with gold or filled with silver epoxy to make them conducting. The fabrication of the V-trenches is explained more clearly in Appendix D. The close proximity of the coated V-trenches sidewalls to the pyramidal cavity sidewalls acts as if the membrane sidewalls have been coated with gold. This step of micromachining the V-trenches is done along with the mixer fabrication, and therefore

eliminates the gold evaporation step on the membrane wafer sidewalls, which proved to be impractical at these frequencies. Also, we are able to etch two trenches parallel to sidewall A, which is above the CPS (IF) line so as to reduce any power loss through this sidewall. The unetched silicon of width 120μm between the two "sidewall A" V-trenches is left unetched since it is the supporting substrate for the integrated CPS line.

The 330GHz receiver structure with an aperture opening of 1.35λ (figure 3.29) and the mixer design without the V-trenches were modeled at 1.35GHz. The 20-25μm-thick diode in the 330GHz design was also modeled at the dipole apex. The resulting dipole impedance is around 76+j50Ω at 330GHz (Fig. 3.30). As discussed in the 250GHz design, there is a 3-4fF parasitic capacitance still unmodeled, which introduces a reactance in parallel with the measured dipole impedance. The resulting embedding impedance at the LO and sideband frequencies is 107-j14Ω, assuming C_p=3.5fF (refer to the circuit in figure 3.12). The higher harmonics are assumed shorted in the mixer analysis. The UVa SC1T4-S20 diode parameters were presented in the 250GHz receiver section. The diode dc series resistance is 10-12Ω and is expected to increase to 16-18Ω at 330GHz. For an LO frequency of 330GHz and an RF frequency of 331.4GHz, the mixer theory [84, 85] predicts a mixer SSB conversion loss and noise temperature of 7.5dB and 2100K, respectively, for an available LO power of 1.5mW at the dipole terminals and a DC bias current of 1.2mA. The predicted IF impedance is around 175Ω at 1.4GHz.

3.4.2 Antenna Design

A new design has been used for the quasi-integrated horn antenna which results in a higher gain antenna and a better Gaussian coupling efficiency rolloff versus

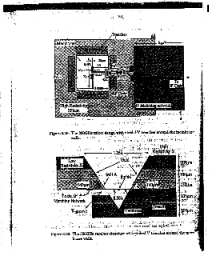

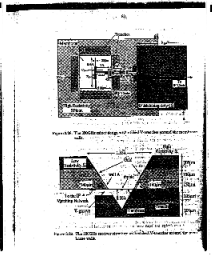

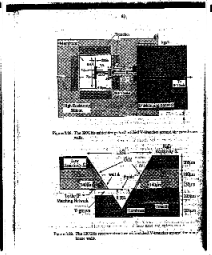

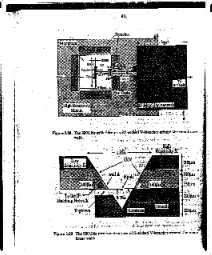

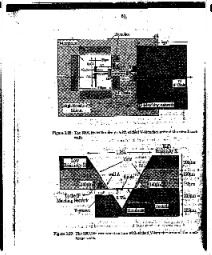

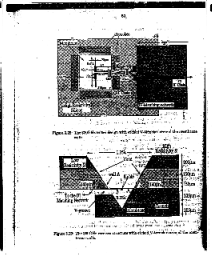

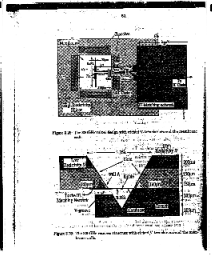

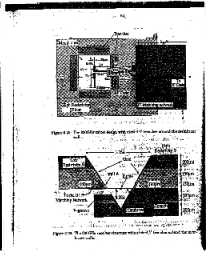

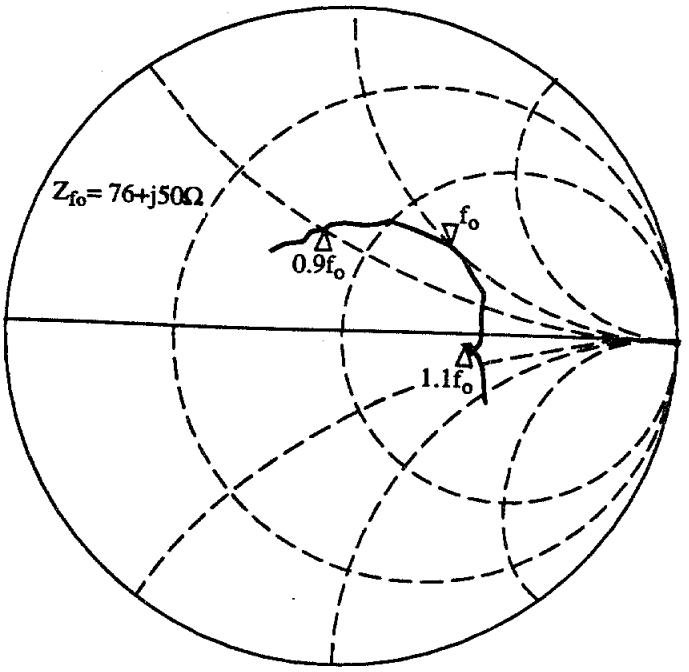

Figure 3.30: The measured feed-dipole impedance in a microwave model of the 330GHz receiver structure. The diode was modeled at the dipole apex but the V-trenches were not modeled.

frequency [55]. A step has been introduced at the junction between the integrated structure with an aperture of 1.35λ and the machined section. This provides more tapering of the modes at the machined section aperture resulting in a higher gain antenna with higher symmetry in the patterns. Referring to figure 3.1, the choice of $a_s = 1.52\lambda$, $2s = 0.17\lambda$, $L_M = 13\lambda$, $X_N = 5.4\lambda$, and $\theta_o = 8.5°$ results in a 23dB gain antenna at the design frequency [73]. The antenna radiation characteristics (Table 3.6) show lower E-plane sidelobe levels than the 20dB gain design. The advantage of this new design is that it is wideband in its Gaussian coupling efficiency and it has a higher gain (Table 3.7). The higher gain results in a larger antenna beam waist w_o, and hence, a larger lens f/D number can be used in front of the receiver antenna, resulting in lower absorption losses in the signal path. Again, the Gaussian coupling efficiency is optimized at each frequency and this means that the distances

in the quasi-optical set-up should be readjusted at each measurement frequency. The 23dB gain antenna has its phase center around 3.6λ away from the machined section aperture [73].

A 23dB quasi-integrated horn antenna was designed at 330GHz for the receiver. The antenna far-field patterns were measured at 352GHz (a 330GHz quadrupler was not available at the time of measurements). The resulting patterns are highly symmetric and the measured E-plane pattern agrees very well with the theoretical E-plane pattern (Fig. 3.31). No cross-polarization measurements were done at 352GHz but due to the high circular symmetry of the patterns, it is expected that the cross-pol level is lower than -20dB [113]. The calculated directivity from the measured patterns is around 25dB. The measured patterns were done on a quasi-integrated horn antenna with trenches etched around the membrane sidewalls, and therefore we conclude that the trenches do not have any significant effect on the far-field patterns.

3.4.3 Receiver Measurements

Video detection measurements were done on the 330GHz receiver from 350GHz to 380GHz. The video responsivity varied between 400V/W and 600V/W for a diode bias current of 40-60μA (see section 3.2.2 for the definition of the video responsivity). This bias current is higher than the 250GHz diode bias current due to a non-optimum diode I-V characteristics. The uncertainty in the measured video responsivity is due to the uncertainty in determining the exact power generated by the quadrupler source.

A picture of the trenches and the flip-chip diode is shown in figure 3.32 (top), and figure 3.32 (bottom) presents a picture of the integrated structure as viewed from its aperture. It can be seen at submillimeter-wave frequencies, the diode dimensions become comparable with the dipole dimensions, and the diode covers a large part of

	$0.965f_o$	f_o	$1.035f_o$
Gain	22.2dB	22.8dB	23.6dB
Aperture efficiency	48.5%	52%	58.4%
10dB Beamwidth	$27.6° \pm 0.2°$	$25° \pm 1.1°$	$22.5° \pm 1.3°$
Sidelobe-level (E-plane)	-28dB	-33dB	-29.8dB
Cross-pol. (45°)	-20.5dB	-21dB	-22dB
Beam-efficiency (to -10dB)	86.6%	86%	86.6%
Gaussian Coupling efficiency	97.2%	97.3%	96.8%
Gaussian Coupling rolloff	96.3%	97.3%	96.0%

Table 3.6: The radiation characteristics of the 23dB quasi-integrated horn antenna over a 7% bandwidth.

Frequency (GHz)	300	310	320	330	340	350	360	380
Gaussian coupling efficiency %	92.5	96	97	97.3	96.5	95	94	90
Gain (dB)	21.4	21.8	22.2	22.8	23.3	23.9	24.4	25.1

Table 3.7: The calculated gain and Gaussian coupling efficiency of the 23dB quasi-integrated horn antenna from 300GHz to 360GHz. The design frequency is 330GHz.

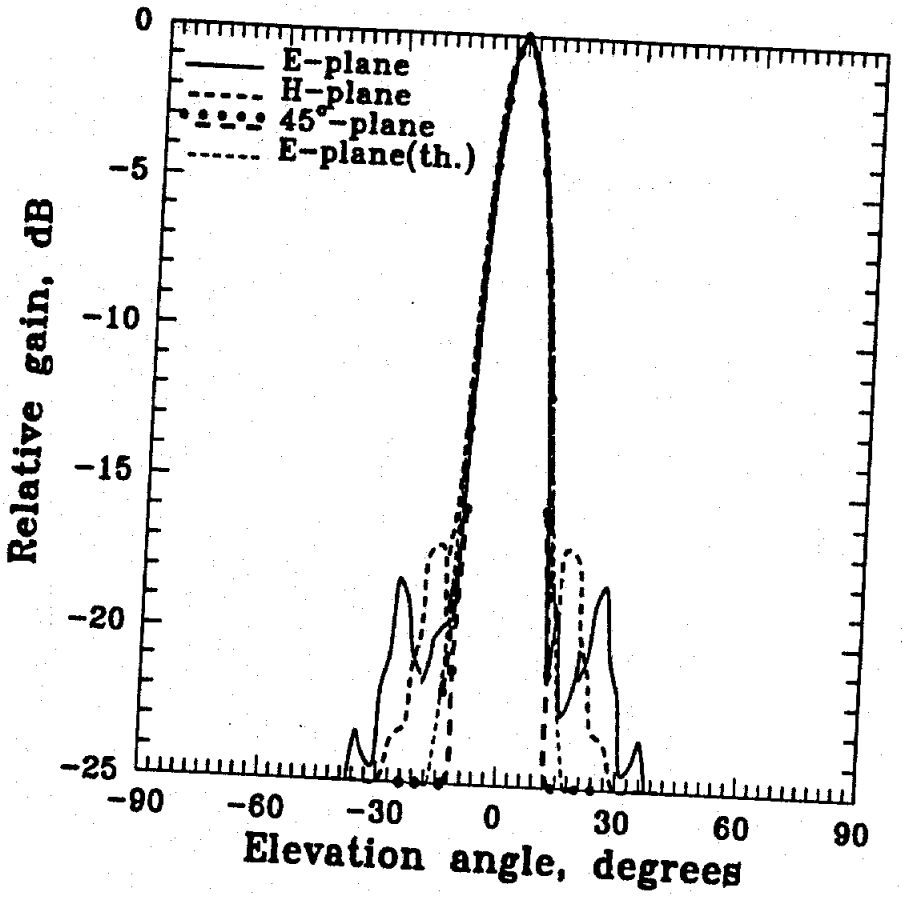

Figure 3.31: The measured E-,H-, and 45°-plane patterns at 352GHz for a 23dB quasi-integrated horn antenna. The design frequency is 330GHz.

the membrane.

The DSB receiver performance around 330GHz was measured using a carcinotron as the LO source [114], and a Martin-Puplett interferometer as the quasi-optical diplexer (refer to Appendix B). The interferometer was tuned for DSB operation for an IF frequency of 1.4GHz. The LO power was coupled into the input port of the diplexer through the appropriate lens that matches its beam waist to the beam waist inside the diplexer (Fig. 3.33). The beam waist at the center of the diplexer is set to 9mm which corresponds to a diffraction loss less than 0.1dB between 320GHz and 360GHz (refer to equation B.12). The beam waist of the 23dB quasi-integrated horn antenna is about 1.63λ [55] or 3.14mm at 330GHz. A lens with an f/D-number of 1.0 and a 55mm diameter was used to couple the output power from the diplexer into the quasi-integrated horn antenna (Figure 3.33). A Fabry-Perot filter [10, 115] was also used in the LO arm between the carcinotron power head and the input port to the diplexer in order to introduce a high rejection to the carcinotron LO noise at the sideband frequencies.

The receiver measurements were done at 335GHz, 345GHz, and 355GHz. Measurements at other frequencies were not possible because the diode I-V characteristics became non-optimal after the 355GHz measurements. At each measurement frequency, the optimum performance is obtained for an LO power of 1.5-2mW available at the antenna aperture. The optimum dc bias current is 1.2-1.4mA. The LO power at the antenna aperture was estimated using a Keating accoustic-cell quasi-optical power meter placed at the position of the quasi-integrated horn antenna [116]. At the optimum points, the loss due to the IF reflection coefficient was about 1-1.2dB, and is mostly due to the discrepancy between the actual IF impedance and the predicted IF impedance which becomes important at high frequencies. The RF

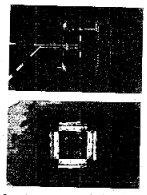

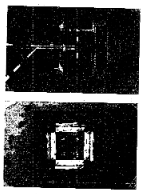

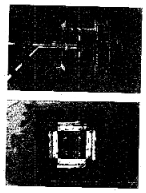

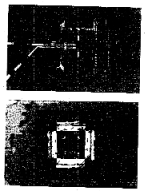

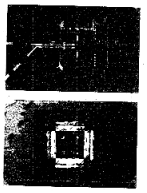

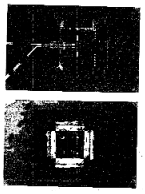

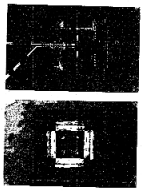

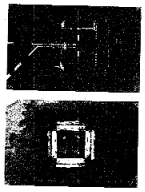

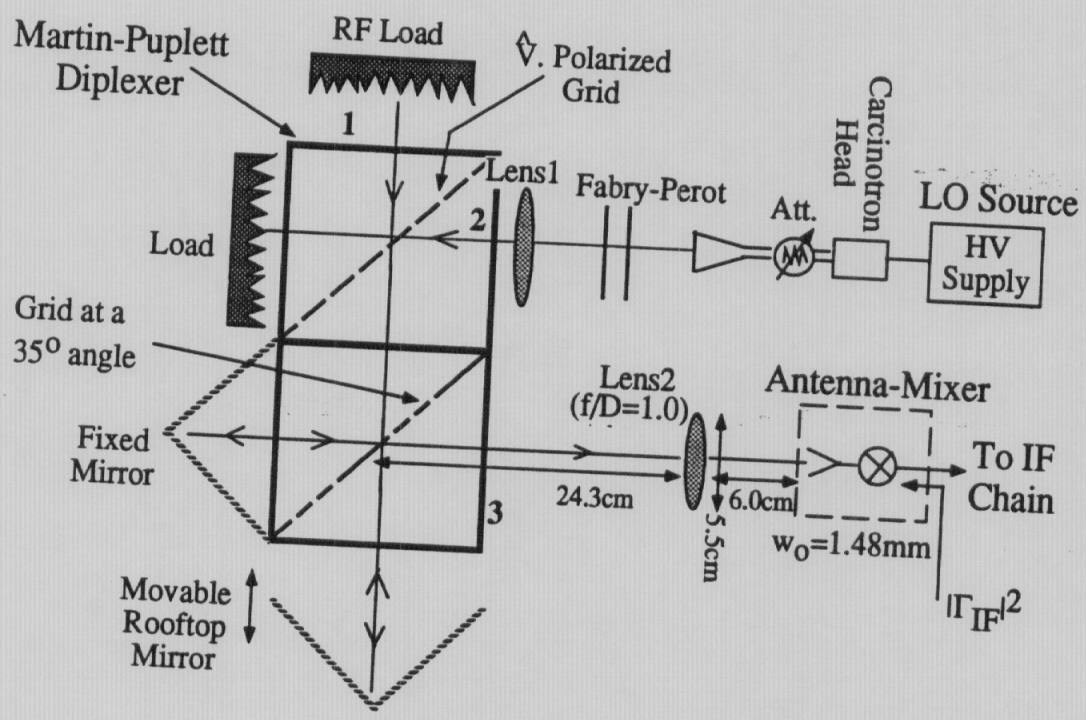

Figure 3.33: The 330GHz quasi-optical set-up. The IF chain has a gain of 97.1dB and a noise temperature of 85.4K.

loss L_2 in the f/1.0 teflon lens in front of the receiver antenna is about 0.8dB between 335GHz and 355GHz (0.3dB reflection loss [108], and 0.5dB absorption loss [66, 109]). The RF diplexer loss $L_{1\rightarrow 3}$ in the signal and image path at both sideband frequencies is estimated to be 0.1dB due to diffraction. In addition to all these RF losses which contribute to the receiver noise, an additional noise component is due to the carcinotron noise at both sideband frequencies. Carcinotrons output noise temperature in the sidebands can be as high as 50,000K [17]. Assuming a 25-27dB rejection at the sideband frequencies in the LO path through the Fabry-Perot filter and the Martin-Puplett diplexer, the noise temperature added to the receiver noise temperature is about 100-150K (Appendix C).

Table 3.8 shows the antenna-mixer DSB performance. Note that the antenna-mixer noise temperature has been corrected for the carcinotron noise. It is expected that the antenna-mixer performance at 315GHz-320GHz is as good as the 335GHz results, and even, is 0.5-1dB better because of a better diode-dipole match at these frequencies as measured in the microwave model and predicted by mixer theory. The effective mixer diode temperature at 335GHz, assuming the attenuator model for the mixer, is equal to 291±5K. This is within a factor of 1.64 of the effective temperature ($\eta T_o/2$) for an idealized shot-noise limited mixer. There is no direct indication that the etched V-trenches around the membrane wafer sidewalls eliminated the power loss in the antenna structure. However, we can conclude that first, the trenches did not affect the far-field patterns and second, we can see an improvement in the new 330GHz design performance in comparison with the performance of the 250GHz receiver. This improvement can be noticed in a reduction in the discrepancy between the effective actual mixer diode temperature and the effective idealized mixer diode temperature at 335GHz.

The Antenna-Mixer DSB Performance		
Frequency (GHz)	Conversion Loss (dB)	Noise Temperature (K)
335	8.5	1750-1800
345	9.2	1870-1920
355	10.9	2500-2550

Table 3.8: The DSB antenna-mixer performance of the quasi-integrated horn antenna receiver designed at 330GHz.

3.5 Comparison of the 90GHz, 250GHz, and 330GHz Mixers Performance to Other Mixer Diodes Performance

The published results for the best room temperature fundamental mixers operating around 90GHz, 250GHz, and 330GHz using whisker contacted and planar GaAs Schottky diodes are shown in Tables in tables 3.9 and 3.10. Any SSB published results have been converted to DSB values by dividing by 2 so that all the results are compared on a uniform basis.

The quasi-optical mixer presented in this work shows very good performance at 90GHz, 250GHz and 335GHz using a simple low cost design. The mixer requires no tuning whatsoever, is planar and is compatible with monolithic techniques. At 100GHz, the measured DSB performance of the quasi-optical planar mixer presented in this thesis is within 2-3dB of the best fundamental waveguide mixers using either a whisker-contacted or a planar diode, and which have the advantage of a backshort waveguide tuner. The measured DSB conversion loss from 86-106GHz is 1-2dB higher than wideband tunerless waveguide mixers [117, 118]. At 250GHz, the performance is within 3-4dB of the best tuned fundamental whisker contacted waveguide mixers. The difference in performance is due to the increase of the planar diode series resistance

Mixer Type (Whisker-Contacted Diodes)	f_{LO} (GHz)	L_c (dB DSB)	T_M (K DSB)	Ref.
SE, WG, Tuned	100	3.3	185	[21]
SE, WG, Tuned	230	3.6	400	[120]
SE, WG, Tuned	230	3.0	365	[12]
SE, WG, Tuned	345	5.8	860	[121]

Table 3.9: Summary of performance of best room temperature fundamental mixers operating near 90GHz, 250GHz, and 335GHz using whisker contacted GaAs Schottky barrier diodes. The IF frequency is between 1-2GHz. SE: single-ended; WG: wave-guide.

and parasitic capacitance effect which are negligible for whisker-contacted diodes, and the antenna loss in the uncoated sidewall.

At higher frequencies, the area on the membrane taken by the diode becomes significant when compared to the dipole. This results in having a relatively thick substrate of GaAs on the back of a significant portion of the dipole antenna, which makes it difficult to match the dipole impedance to the diode impedance. The GaAs substrate can be thinned down but it becomes impractical to mount chips which are less than 25μm thick. Also, the thermal conductivity of the thinned diode is reduced which causes degradation in performance due to excessive diode heating [119].

In the 330GHz, the power loss in the uncoated sidewall was reduced through the use of V-trenches. As we can see from the two tables, the performance of the tunerless quasi-optical receiver at 335GHz is within 2.5dB in conversion loss and in noise figure of the best tuned waveguide mixer using a whisker contacted diode with 1.5μm anode diameter. Comparing to the best tuned waveguide mixer performance at 335GHz employing a similar planar UVa diode, our antenna-mixer conversion loss is within

Mixer Type (Planar Diodes)	f_{LO} (GHz)	L_c (dB DSB)	T_M (K DSB)	Ref.
Ba, WG, Tuned	94	2.5	—	[117]
SE, WG, Tuned	106	3.2	360	[27]
SE, WG, Tuned	94	2.4	260	[26]
ShP, QO	90	6.7	1080	[64]
SE, QO	88	6.6	1160	[62]
SE, QO	92	5.5	770	This work
ShP, WG, Tuned	205	5.7	800	[28]
ShP, QO	182	8.5	1820	[64]
SE, QO	258	7.1	1400	This work
SE, WG, tuned	345	6.5	1370	[29]
SE, QO	335	8.5	1750	This work

Table 3.10: Summary of performance of best room temperature fundamental mixers operating near 90GHz, 250GHz and 335GHz using Planar GaAs Schottky barrier diodes. The IF frequency is between 1-2GHz.
SE: single-ended; WG: wave-guide; Ba: balanced mixer; ShP: subharmonically-pumped; QO: quasi-optical.

2dB and its noise figure is within 1dB only!

Currently, it is easy and inexpensive to array four of these receivers on a single chip. Together, the four planar receivers have a sensitivity similar to that of one of the best tuned waveguide mixers at frequencies from 100GHz to 360GHz.

3.6 Conclusion and Future Work

The work presented in this thesis represents the first complete work on building low-noise integrated Schottky receivers for millimeter- and submillimeter-wave applications using planar antennas printed on thin dielectric membranes. The integrated horn antenna, which consists of a dipole-probe integrated on a thin membrane and suspended inside a pyramidal cavity in silicon and which does not suffer from substrate-modes and surface-wave losses, has been used as the receiver structure. The knowledge of the RF dipole-probe impedance inside the pyramidal horn cavity and the knowledge of designing the integrated horn antenna to result in excellent radiation patterns led to the design of a novel simple mixer design. No RF matching network was required between the dipole-probe and the mixer circuit. Also, no tuning was required whatsoever because the dipole-probe can be designed so that its inductive reactance can tune out the diode capacitive reactance over at least a 10% bandwidth. The mixer circuit is planar and compatible with monolithic techniques. In addition to the comparable performance of integrated horn antenna Schottky receivers to that of tunable waveguide Schottky receivers at room temperature, the low cost of fabrication and the simplicity of the integrated receiver design make it suitable for compact millimeter- and submillimeter-wave receivers needed for mass-production.

Future work on integrated horn antenna Schottky receivers can be directed toward building quasi-optical millimeter-wave integrated balanced mixers. Two orthogonal dipoles can be integrated on the membrane, one dipole for RF and the other for LO. At the center of the membrane, four planar Schottky diodes are mounted in a ring mixer configuration between the two dipoles [122]. This work can be extended with low cost to building an imaging array of integrated horn antenna receivers with balanced mixer design.

The development of integrated horn antenna SIS receivers should be investigated. The integrated horn antenna outperforms other printed-crcuit antennas by its radiation efficiency and by its lossless structure. The SIS mixer is the most sensitive detector in the millimeter-wave region, and all high-quality millimeter-wave astronomy is based it. The SIS junction could be deposited lithographically at the apex of the dipole which is integrated on the membrane suspended inside the horn structure [123]. The combination of the integrated horn antenna with an SIS junction will result in a highly sensitive very low-noise receiver at millimeter- and submillimeter-wave frequencies, and with the development of sensitive SIS junctions at high frequencies.

With the progress of the GaAs processing technology, many industries are pushing the development of MMICs and millimeter-wave monolithic circuits for commercial applications. The integrated horn antenna is a very promising technology and all monolithic techniques can be applied on the wafer; however, the membrane does not allow the monolithic integration of semiconductor devices such as GaAs diodes. Also, as it was seen from the 335GHz integrated horn antenna design, it becomes inadequate to use the hybrid approach for the integrated mixer circuit because of the small circuit dimensions and because mounting the diode becomes very time consuming. This problem can be solved by the insertion of thin GaAs wafer into the integrated horn antenna structure which replaces the membrane inside the silicon cavity. The problem of surface-wave modes has been solved in [73, 124] by the synthesis of a cavity environment around the dipole, using the etching of trenches or via-holes. This new way of building an integrated horn antenna receiver will yield strong, compact, efficient, and inexpensive when mass-produced, monolithic planar systems suitable for millimeter-wave commercial and scientific applications. Also, these systems will represent a very promising solution for the development of monolithic Schottky re-

ceivers in the submillimeter-wave region where the building of waveguide receivers require a fortune!

CHAPTER IV

92GHz DUAL-POLARIZED INTEGRATED HORN ANTENNAS

Polarimetric radar is an increasingly important tool in microwave and millimeter-wave remote sensing. The technique consists of transmitting horizontally and vertically polarized waves, and measuring both polarizations of the return signal. A target polarization matrix is formed, and the return from any other incident polarization could then be readily synthesized. This technique has been used for image enhancement and target discrimination in synthetic aperture radars [125, 126]. Several researchers have also used orthogonal polarization for local oscillator and RF injection in quasi-optical balanced mixers [127, 122]. These mixers have inherent isolation between the RF and LO ports, and do not require a diplexer for combining the RF and LO signals. Dual polarization is also used in the emerging field of quasi-optical amplifiers. In this application, the input plane wave is horizontally polarized and amplified by a differential amplifier and the output wave is vertically polarized [128, 129]. In this chapter, we use mode symmetry and orthogonality in a rectangular waveguide to design a dual-polarized horn-antenna array suitable for polarimetric imaging and balanced mixers. The dual-polarized antenna array shares all the advantages of the single-polarized horn array discussed in chapter 2, such as high aperture

efficiency and diffraction-limited imaging, and also provides two polarization channels with identical responses. Also, the dual-polarized design can be combined with a machined section to result in high gain (20-26dB) [73, 80]. The dual-polarized antenna consists of two dipoles perpendicular to each other and suspended on the same membrane inside the horn cavity (Figure 4.1). The dipoles couple to an orthogonal set of waveguide modes, and therefore are effectively isolated from each other.

The patterns are calculated for each dipole independently, by approximating the horn structure by a cascade of rectangular waveguide sections, and matching the boundary conditions at each of the waveguide sections and at the aperture of the horn. A detailed analysis of the theory is given in [73, 51]. The Schottky-diode or SIS detectors are integrated at the dipole apex at the center of the membrane, and do not couple due to symmetry. The IF or video signals are taken out through a novel bias structure that leaves room at the center of the membrane for the orthogonal dipoles and detectors. In section 4.1, the isolation between the two dipoles and the impedance of each dipole are measured using a microwave model of the dual-polarized horn antenna. Section 4.2 describes the fabrication process of a 5x5 dual-polarized integrated horn antenna array at 92GHz. The millimeter-wave measurements on the fabricated array and the comparison between experimental and theoretical data are presented in section 4.3.

4.1 Microwave Modeling and Design

A 1-2GHz microwave model was built for modeling the dual-polarized horn antenna. The antennas were designed for polarimetric applications, and two independent channels with a high degree of isolation were required. This is different from balanced mixers, where the antennas would combine together at the center of the

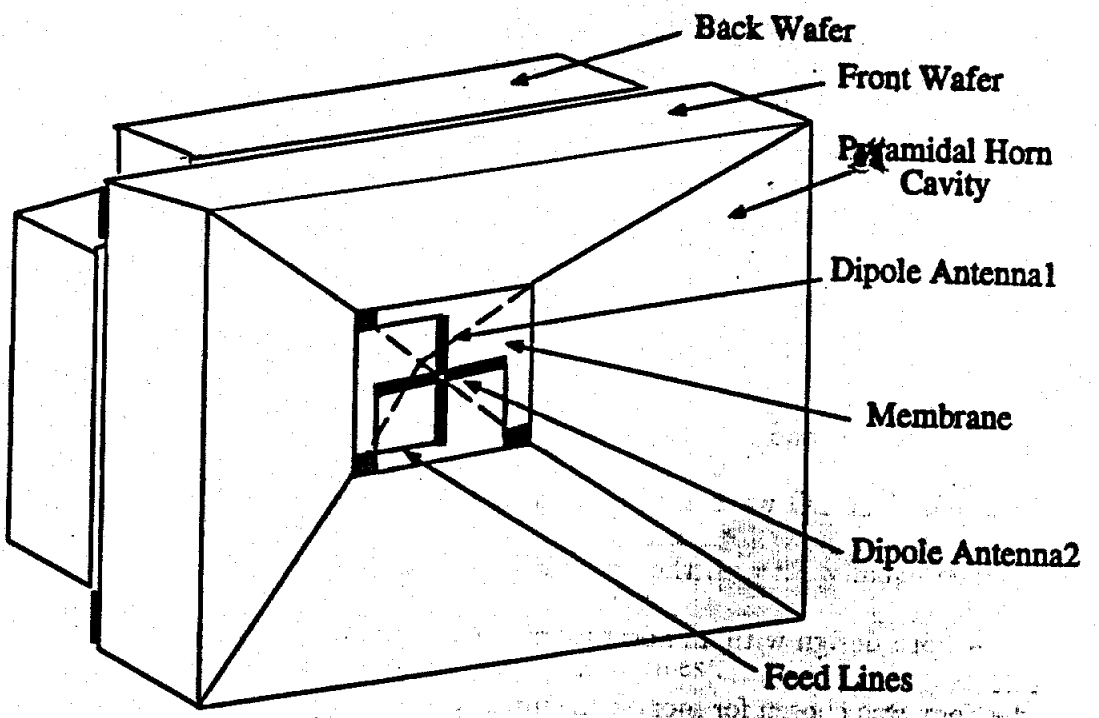

Figure 4.1: Monolithic dual-polarized horn antenna element with a novel bias and feeding structure.

membrane in a two or four-diode mixer to yield a single IF output [127, 110]. In our case, the Schottky diode or the SIS detector at the center feed of each channel acts as a fundamental mixer for the RF and LO waves of *same* polarization, coupled by the dipole antenna parallel to that polarization, and which is feeding that channel. This results in two separate IF signals to be taken out on the membrane wafer. The comfortable space present at the edge of the membrane wafer allows us to separate these two IF signals from each other, so as not to have interference between them.

An immediate problem is the design of a bias and IF feeding structure. Referring to the single-polarized horn array design discussed in chapter 2 (Figure 2.1), the coplanar-stripline feed at the center of the membrane could no longer be used since each antenna will electromagnetically short-circuit the other channel. To solve this problem, a new feeding structure was developed (Figure 4.1). It consists of narrow

lines (5μm) wide close to the cavity walls and connecting the two ends of the dipole antennas. The tangential component of the electric field is zero near the cavity walls, and therefore no RF current is induced in the bias lines. Furthermore, the lines are thin and do not affect the perpendicular component of the electric field. The bias lines are quarter wave in length and act as a $\lambda/4$-transformer between the end of the dipole antenna and the pyramidal cavity, which could be considered as an RF ground plane. The RF and LO waves will be coupled quasi-optically to the two orthogonal channels. The LO wave is incident at a 45° to each channel so that the LO power is divided equally between the two dipoles (Figure 4.2).

A horn design with an aperture of 1.35λ-square, and a feed position of 0.39λ from the apex was chosen for monolithic integration. This design yields nearly equal 10dB-beamwidths of 90° in the E and H-planes, and couples well to f/0.7 reflector systems [58]. The measured input impedance of each dipole is identical to the impedance of a single polarized dipole (see chapter 2 and [74]). The resonant impedance is 56Ω, and the resonant dipole length is 0.38λ (Figure 4.3). As presented in chapter 2, the dipole impedance for a feed position of 0.39λ is suitable for Schottky-diode mixers [96, 130]. The measured mutual coupling between the channel antennas at 1.2GHz is less than -30dB over a $\pm$10% bandwidth (Figure 4.4) which is sufficient for many millimeter-wave applications. These impedance measurements are also valid for a dual-polarized horn antenna in an array. This is due to the fact that the isolation between the two orthogonal dipoles is very high, and the aperture size of a horn antenna element is larger than 1.0λ-square which minimizes the mutual coupling between the horn antenna elements in the array [73].

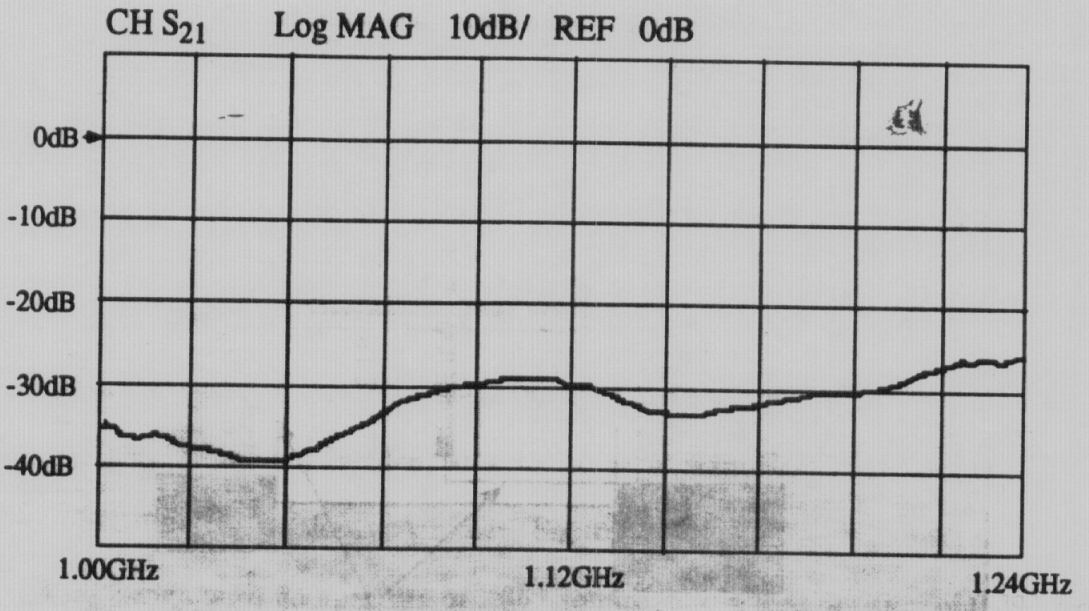

Figure 4.4: The measured isolation between the orthogonal dipoles in a microwave scale model. The center frequency is 1.12GHz.

4.2 Fabrication

The fabrication process of the dual-polarized horn antennas array is the same as the one described in chapter 2 for the fabrication of single-polarized horn antennas array. The horn array is composed of stacked silicon wafers with a ⟨100⟩ crystal orientation. The opening of the front wafer determines the aperture size, while the total thickness of the front wafers determines the position of the dipole antennas inside the horn. The two orthogonal dipole antennas and the corresponding two detectors are integrated on the membrane of each horn antenna element in the array. For this design, the detectors are 4μm-square bismuth microbolometers whichare thermal detectors, and can couple strongly if integrated near each other at the center of the membrane. To minimize the thermal coupling, the detectors were placed $40 - 50\mu$m apart in the horizontal and vertical directions (Figure 4.5). A 1μm polyimide-layer

[82] was used to isolate the two antennas. The polyimide layer provided a good dc and low-frequency isolation. This design, with shifted and overlapping antennas, broke the symmetry of the dual-polarized horn antenna and affected the 92GHz performance. It is important to note that Schottky diode mixers and SIS detectors are coherent detectors (as opposed to thermal) and will not couple if integrated directly at the center of the membrane.

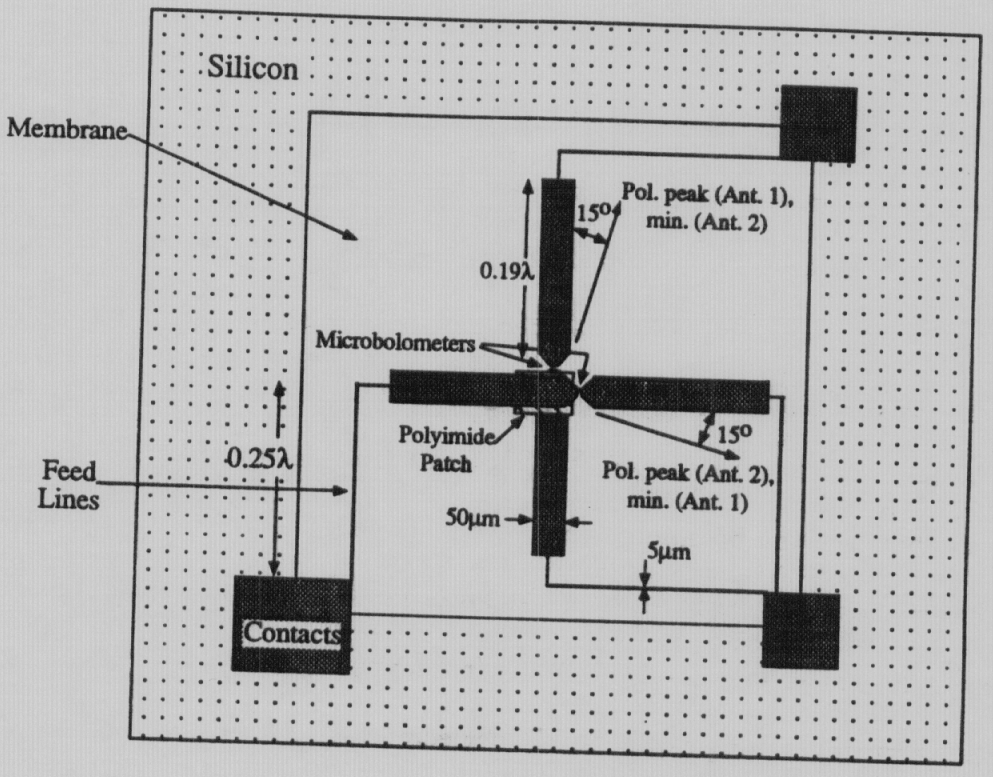

Figure 4.5: The exact design and polarization tilt of the 92GHz dipole antennas.

4.3 Millimeter-Wave Measurements

Millimeter-wave measurements were done on a 5x5 horn array, with a horn opening of 1.35λ and a dipole feed-position of 0.39λ from the apex. The silver dipole antennas were 2500Å thick. The bolometer impedances ranged from 40Ω to 70Ω, with a responsivity around 8V/W at a 0.1V bias. The horn array was mounted at

the center of a two-axis computer-controlled gimbal mount, and the patterns were measured with a 92GHz Gunn source modulated at 300Hz. All pattern measurements were done on central elements in the array. The output from the bolometers was fed to a PAR-124A lock-in amplifier. The detected voltage peaked at 10μV and the signal-to-noise ratio was better than 26dB.

The polarization response of both antennas is shown in Figure 4.6. The peaks and nulls shifted 15° from the direction of the probe dipoles due to the electromagnetic coupling between the off-center antennas. The polarization is not expected to shift if electronic detectors are used and the antennas are integrated exactly at the center of the membrane. The antennas are still linearly polarized, and a polarization isolation higher than 20dB was measured between the two channels (Fig. 4.6). It is also possible to check for thermal coupling by measuring the peak-to-null ratio in the polarization curve at two different modulation frequencies. This is because the thermal path between the bolometer detectors is modelled as a lossy transmission-line [131] that will exhibit less attenuation at lower modulation frequencies. The peak-to-null ratio did not change for modulation frequencies of 90Hz and 900Hz, indicating that the thermal coupling can be safely neglected.

The E-, H- and 45°-plane patterns of both channels are presented in Figures 4.7 and 4.8. It is difficult to define these patterns when the polarization direction no longer coincides with the array axis. In this case, the patterns were taken at a polarization angle of 0° (this is the standard IEEE definition) without rotating the antennas for maximum response. This did not affect the patterns since the power loss was less than 0.2dB. The patterns are symmetrical and agree well with theory, and the horizontal and vertical antennas exhibit nearly identical responses.

Patterns were also taken at the peak polarization angle of 15° (Figure 4.9). In this

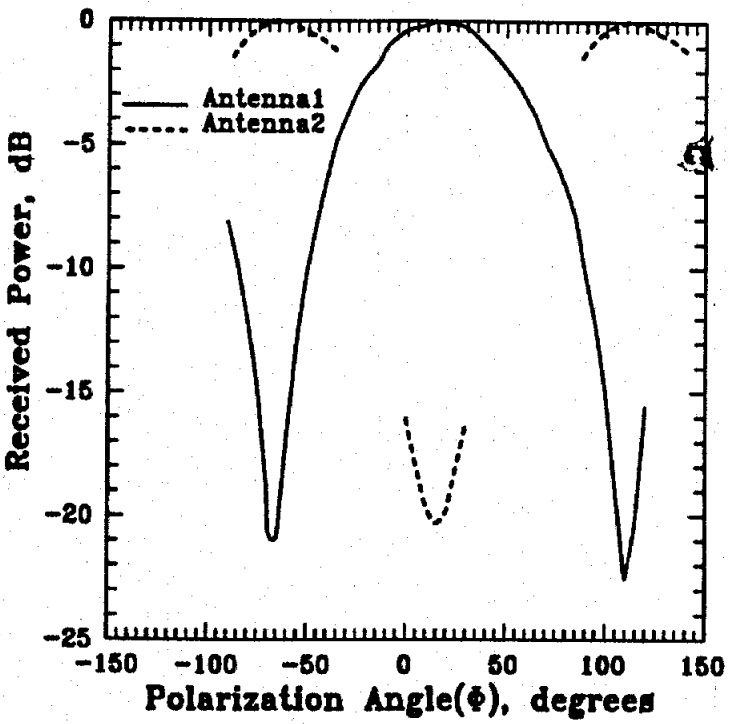

Figure 4.6: The measured polarization response of the orthogonal antennas at 92GHz.

case, the array was rotated 15° for maximum response, and the standard E-, H- and 45° plane cuts were measured. Again, the antennas showed identical patterns, and the cross-polarization level was lower than -23dB in the E and H-plane patterns, and peaked at -15dB in the 45° pattern. The cross-polarization level agrees with earlier measurements done on singly polarized horn antennas [51]. The patterns agree well with the standard E-and H-plane patterns for an integrated horn antenna element in an array [73, 51], except for the absence of the -13dB sidelobe in the measured E-plane. This is because the E-plane scan at a polarization angle of 15° does not coincide anymore with an array axis. This result is a strong indication that the E-plane sidelobe is due to the two-dimensional array structure and its corresponding Floquet modes [79, 73].

The two-dimensional pattern of a single channel shows a nearly rotationally-symmetric pattern up to an angle of 45° from broadside, and a calculated co-polarized

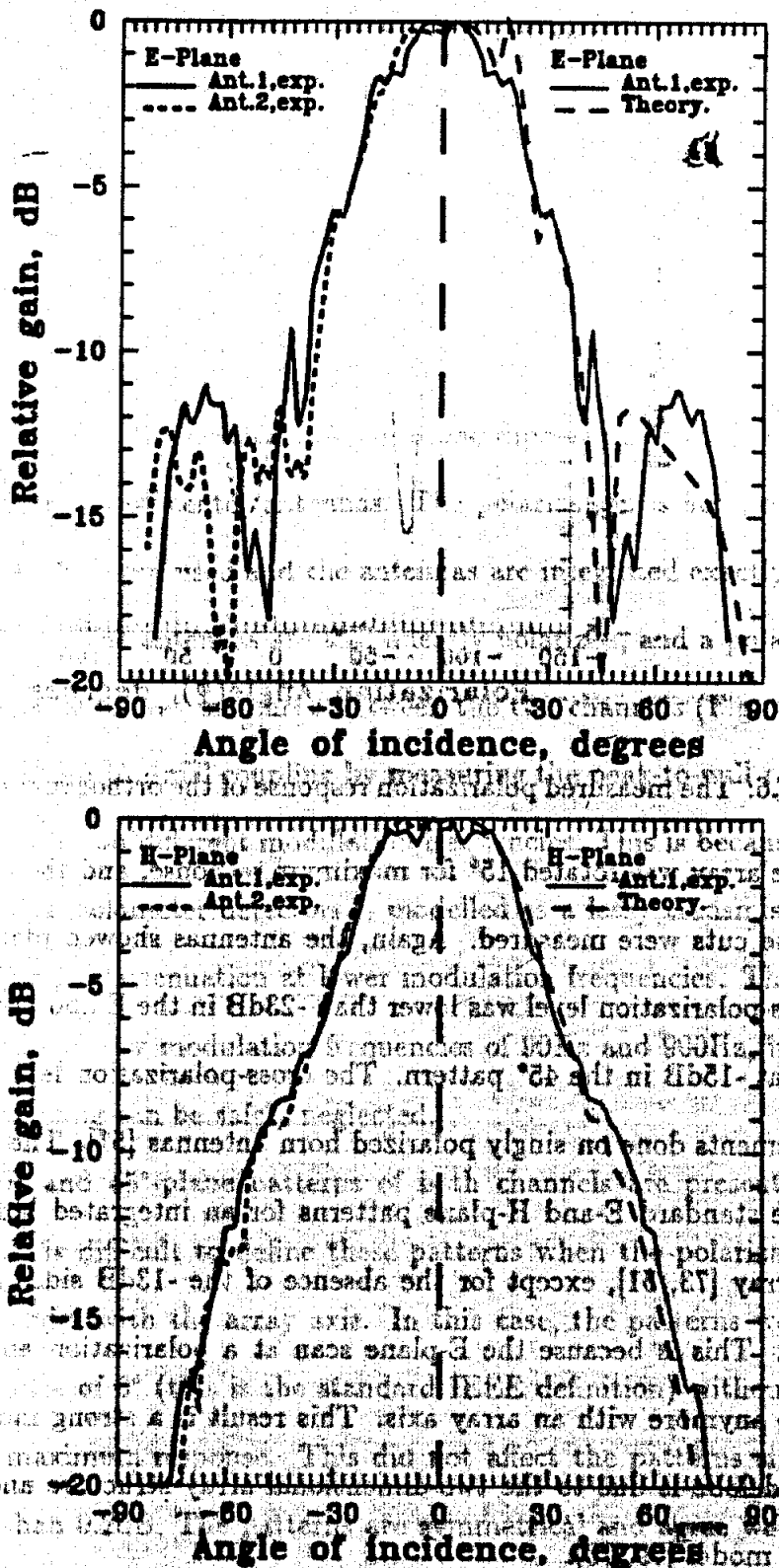

Figure 4.7: Measured 92GHz E-plane (top) and H-plane (bottom) patterns on a 1.35λ-square dual-polarized horn antenna on a polarization angle of 0°. The vertical and horizontal antennas are compared on the left, and on the right is a comparison between theory and experiment.

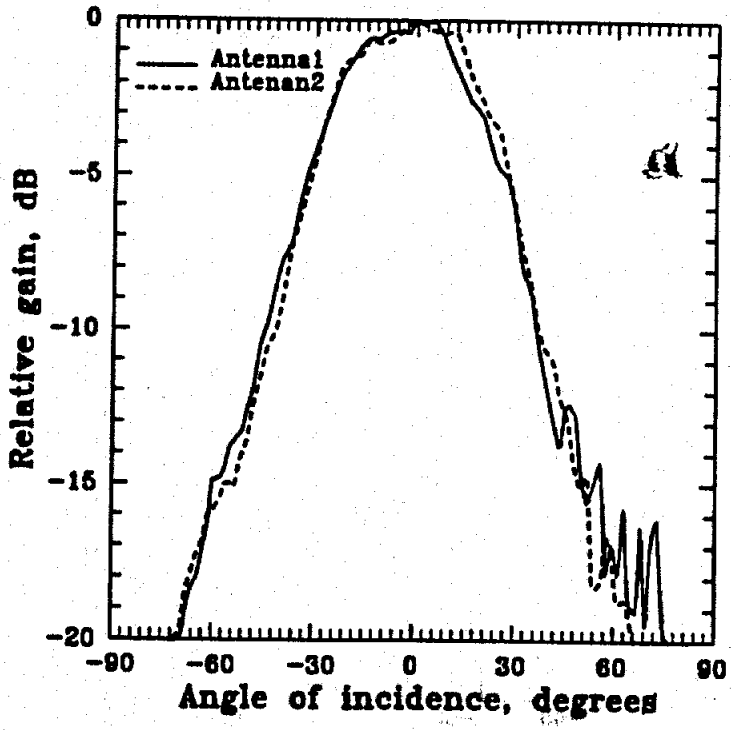

Figure 4.8: Measured 92GHz 45°-plane patterns of both channels on 1.35λ-square dual-polarized horn antenna on a polarization angle of 0°.

directivity from the two-dimensional pattern scan of 12.7±0.1dB (Figure 4.10) . This yields an aperture efficiency of 81±2%. Theoretical modeling on the horn array indicate that the aperture field distribution is quasi-TE_{10} with a small phase error. This is due to the array environment and the associated Floquet-modes. It is therefore possible to achieve a high aperture efficiency from a 1.35λ horn in an array environment. The radiated power is well confined to a main central beam, and 88% (or 79%) of the radiated power is within a 100° (or 80°) beamwidth. The resulting spillover loss is 0.5dB and 1.0dB, respectively. The dual-polarized horn array is therefore well suited for f/0.7-0.8 imaging systems [58].

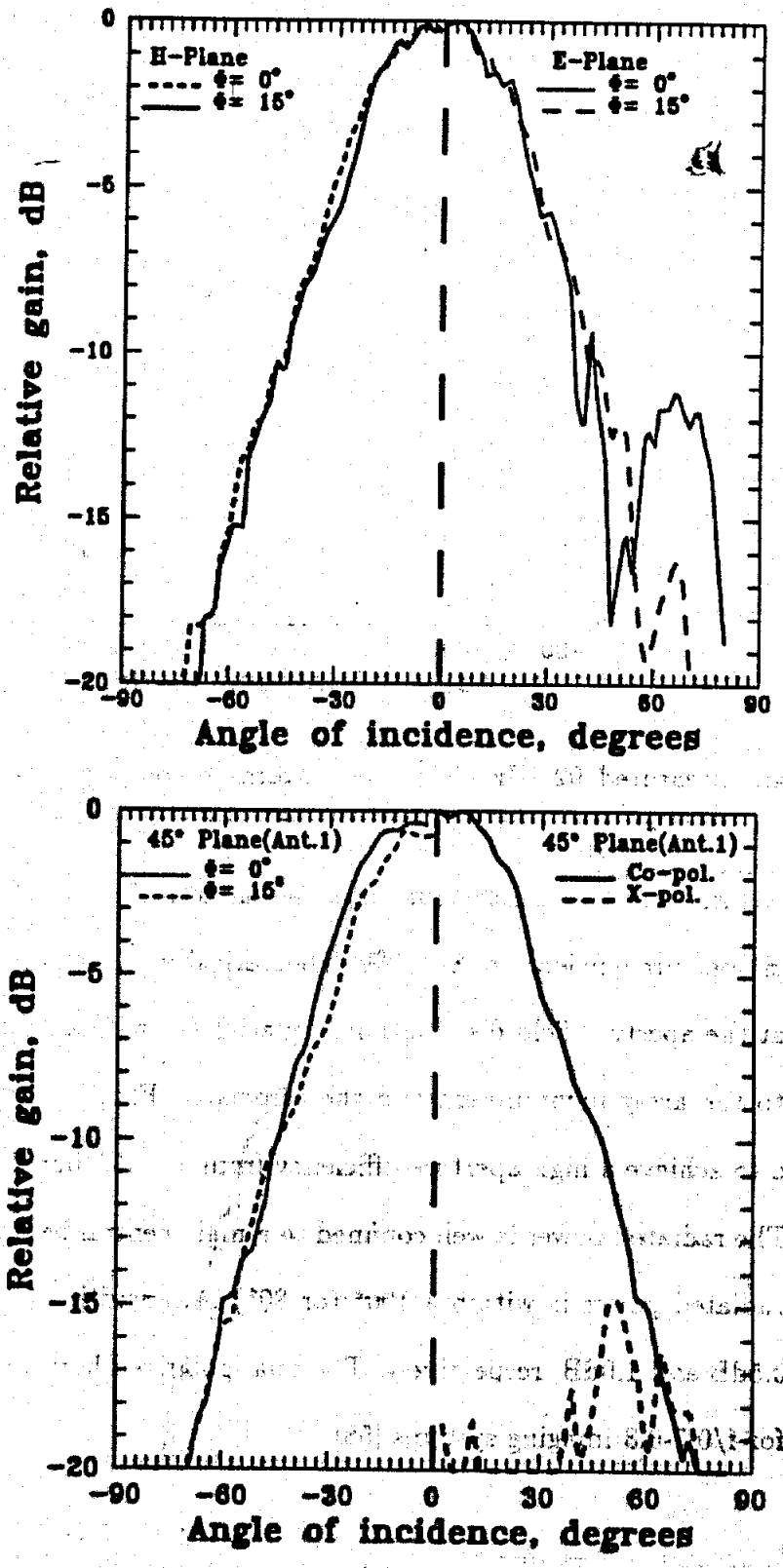

Figure 4.9: Comparison between the measured 92GHz response at polarization angles of 0° and 15° (polarization peak). The E- and H-planes are compared on (top) and the 45°-planes along with the measured cross polarization are presented on (bottom).

4.4 Summary and Conclusions

The two-dimensional dual-polarized horn antenna array has been shown to be a simple monolithic antenna suitable for millimeter-wave focal-plane applications. The key idea is the use of symmetry and orthogonality in rectangular waveguide modes. The orthogonal channels show identical far-field patterns, and agree well with theory. A small shift and an overlap in the orthogonal antennas shifted the polarization by 15° from the dipole directions, and limited the polarization isolation to 20dB at 92GHz. In the future, it should be possible to achieve a much better polarization isolation if the antennas are integrated directly at the center of the membrane with Schottky-diode detectors. This design has been used by Chen-Yu Chi at the University of Michigan to build a quasi-optical amplifier at 6GHz [128].

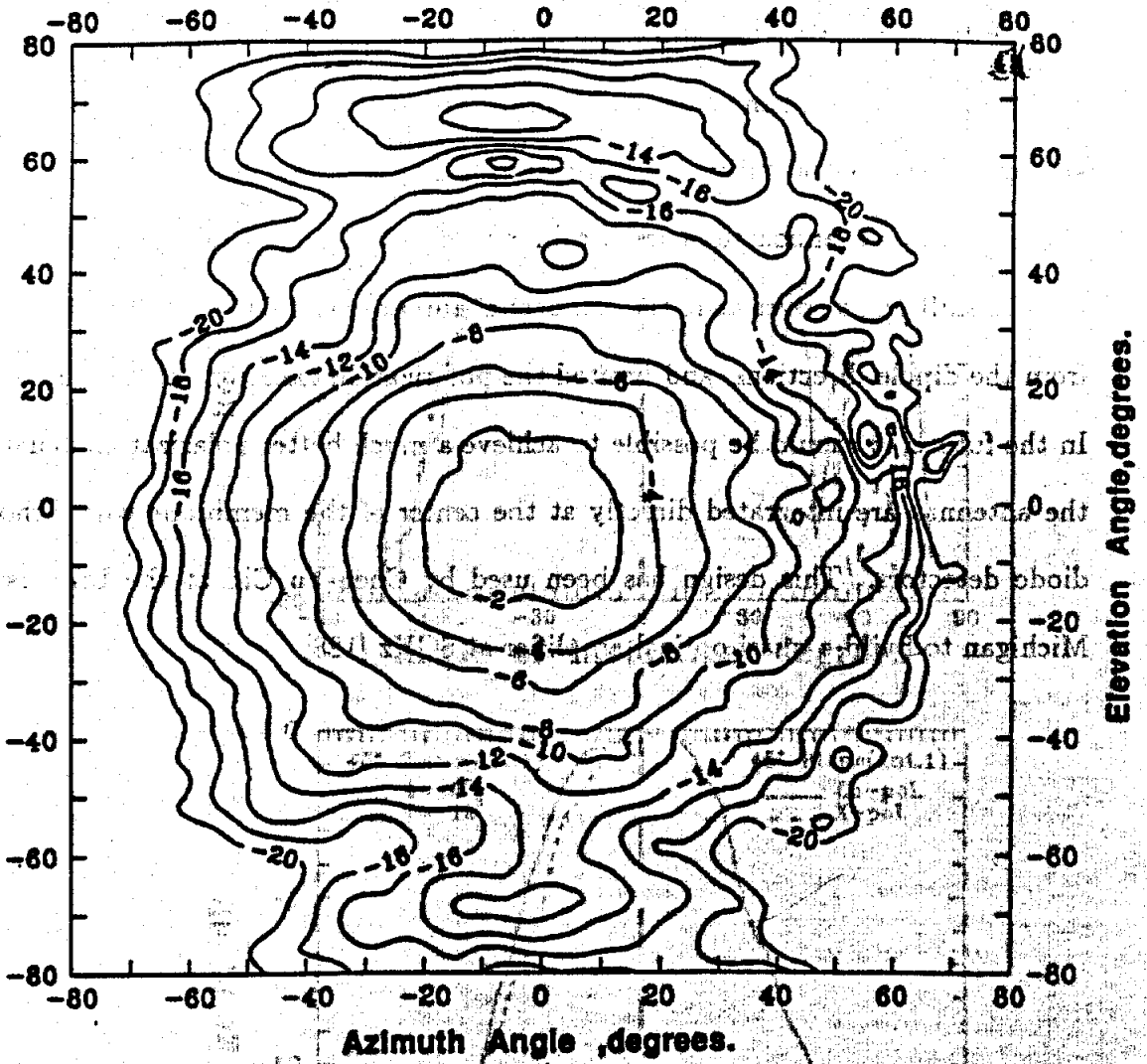

Figure 4.10: Measured two-dimensional scan at 92GHz of a single channel in a 5x5 dual-polarized array. The response of the other channel was virtually identical.

APPENDICES

APPENDIX A

Technology Demonstration at 802GHz

In chapter 2, the design of an integrated horn antenna in an array or in a ground plane was discussed. The fabrication of singly-polarized integrated horn antennas array has been successfully demonstrated at 94GHz [75]. To demonstrate the feasibility of submillimeter wave imaging arrays, a 16x16 singly-polarized integrated horn-antennas imaging array was built at 802GHz with 1.4λ horn opening (Figure A.1). The feed dipole is 0.4λ long and positioned 0.38λ from the apex. As discussed in chapter 2, this design results in a resonant feed-dipole impedance of 56Ω.

At 802GHz, the array consists of only two silicon wafers etched anisotropically and stacked together to form the pyramidal cavity. The front wafer or the membrane wafer is 210μm thick, and the feed-dipole antennas and the detection circuitry are integrated on its back side (the membrane side). The detectors are 4μm-square Bismuth microbolometers and are integrated at the center of each feed-dipole antenna. The back wafer is 390μm thick with an array of 150 μm pyramidal back cavities etched in it. In fact, it is much easier to build submillimeter-wave integrated horn antennas because the membrane becomes very small (about 300μm to 100μm-square) and only two wafers are needed for the horn cavity.

In our design, we contact an array of 4×4 elements in the center since we are only interested in the patterns of a single element in an array. There is a lot of space

available on the front wafer backside for bias and IF circuitry and in the case of a 1.4λ-square, the available space is 1-$(0.54\lambda/1.4\lambda)^2$ = 85% of the wafer surface. This is of course expected to increase to 98-99% with the use of a quasi-integrated horn having a gain of 23dB (aperture of 5.4λ-square).

The far-field patterns of a single integrated horn antenna in an array were measured using a far-infrared laser tuned at 802GHz [132]. The theoretical far-field patterns of a horn antenna in a two-dimensional array has been discussed in chapter 2 and in [73, 51]. Figure A.2 shows the experimental E and H-plane patterns which agree well with the theoretical patterns.

The H-plane is smooth due to the TE_{10} tapering of the electric field across the aperture. In the case of the E-plane, the horn sees the array, and the spikes and nulls in the patterns are due to specific Floquet-modes. The E- and H-plane 10dB-beamwidths are 80° and 90° respectively and the far-field pattern matches well an f/0.7-0.8 imaging system. The directivity of a single horn antenna calculated from the measured E and H-plane patterns is 12.3dB$\pm$0.2dB. The pattern is quite symmetrical as is evident from the measured 45°-plane pattern (Figure A.3). The radiated power is well confined to a main central beam, and 88% of the radiated power is within a 100° beamwidth. The resulting spillover loss is around 0.5dB.

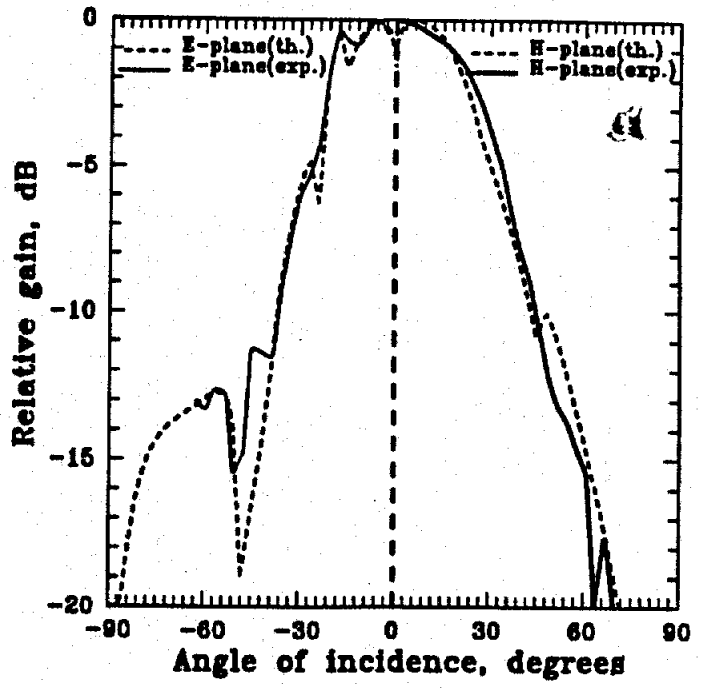

Figure A.2: Theoretical and experimental E- and H-plane patterns.

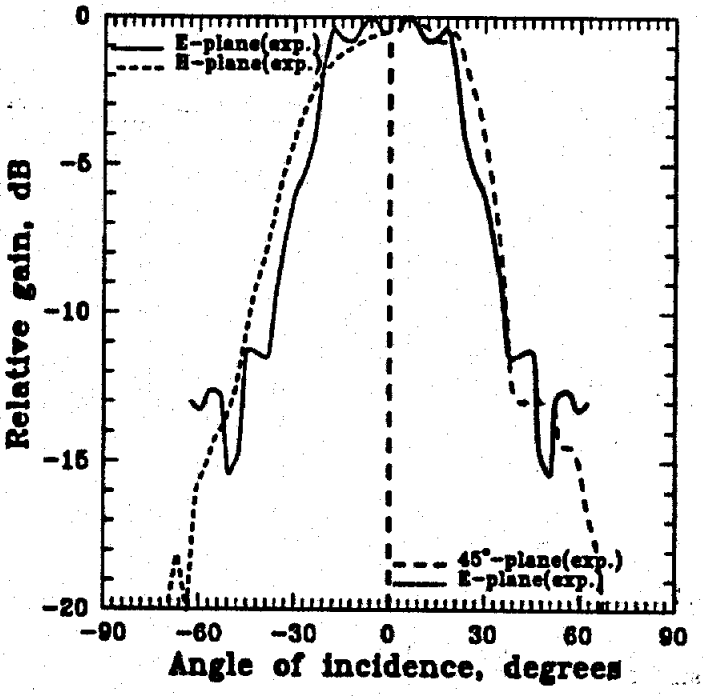

Figure A.3: Experimental E- and 45°-plane patterns.

APPENDIX B

Quasi-Optical Diplexers for Millimeter- and Submillimeter-Wave Applications

A wide variety of optical interferometers have been used in the millimeter and submillimeter-wave regions for LO injection in receiver systems and as single-sideband filters. These devices have a considerable variation in geometries, and can be described as either two-beam interferometers or multibeam interferometers. Fabry-Perot interferometers, or multibeam interferometers, based on repeated reflections between two partially reflecting mirrors with high reflectivity, have the advantage of achieving high resolution in a compact size because of the long internal path [10, 133]. However, Fabry-Perot interferometers have shown to suffer more absorption and diffraction losses than two-beam interferometers due to the multiple reflections that the signal encounters between the two parallel partially reflecting mirrors [134, 10, 135].

In this appendix, we will only be discussing the configurations and operations of two-beam interferometers which have been used in most of the applications discussed in this thesis. They are favored for their low insertion loss for both the signal and local oscillator and their high rejection of LO noise. Their behavior is nearly ideal and their size can be designed to be compact. In the first section of this appendix, we will discuss the different types and configurations of two-beam interferometers for DSB operation. A design method to follow when building a quasi-optical system that

includes an interferometer will then be outlined, and in the last section, a two-beam interferometer configuration for single-sideband filtering is presented.

B.1 DSB Operation of Dual-Beam Interferometers

B.1.1 Mach-Zender Interferometer

The Mach-Zender interferometer principle is based on the amplitude division of the signal into two beams, delaying one of the beams, and then recombining the delayed and undelayed beams at the output port [101, 10, 136]. Figure B.1 shows the basic geometry of the Mach-Zender Interferometer. The beam splitters are designed to have a specific power reflectance R at a certain frequency, for a specific beam incidence angle and a specific polarization. As we can see from figure B.1, the beams are incident at an angle of 45° on the beam splitters from input ports 1 and 2. The polarization of the two input beams and the two output beams is vertical (TE). TM polarization is not used because it gives low reflectance values, and this results in a high insertion loss in the LO path. The power transmissions from port 1 to port 3, and from port 2 to port 4 are equal to :

$$P_{1\to3} = P_{2\to4} = 1 - 2R(1-R)[1 + cos(2\pi\Delta/\lambda)] \tag{B.1}$$

Similarly,

$$P_{2\to3} = P_{1\to4} = 2R(1-R)[1 + cos(2\pi\Delta/\lambda)] \tag{B.2}$$

where Δ is the path length difference, which is equal twice the separation distance d between a beam splitter and the corresponding parallel mirror, and λ is the signal wavelength.

In DSB operation, we choose $\Delta = 2d = \lambda_{IF}(2K-1)/2$, where K is 1,2,3,.. and $f_{LO}/f_{IF} = 2n$, where n =1,2,3,.. ($\lambda_{IF} = c/f_{IF}$). The value of the reflectance is

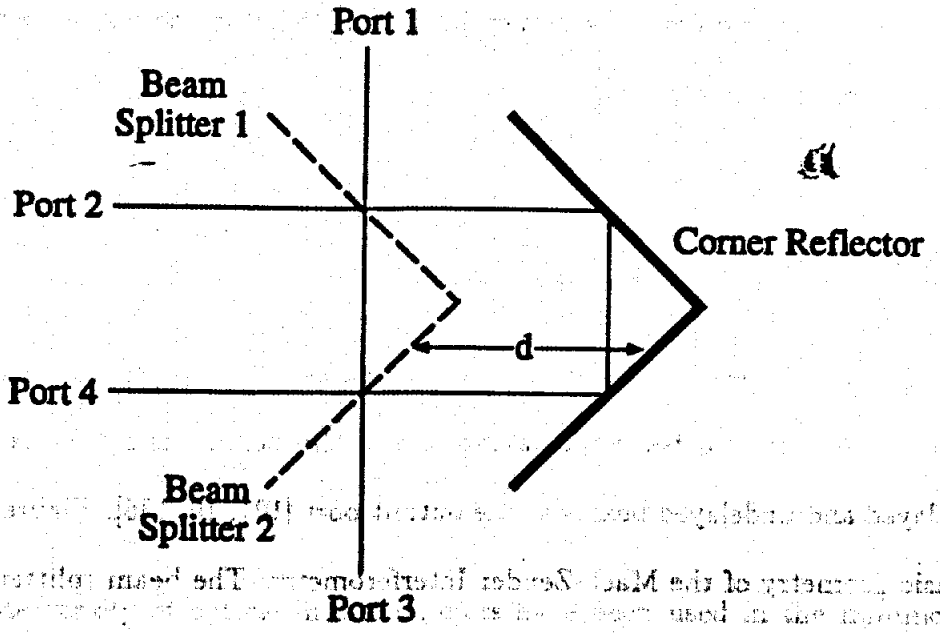

Figure B.1: The Mach-Zender Interferometer composed of two beam splitters and two reflecting mirrors.

chosen to be R at the LO frequency and is taken to be R at the upper and lower sideband frequencies since in general, $f_{IF} \ll f_{LO}$. This results in $P_{1\to3,max} = 1$, and $P_{2\to3,min} = 0$ at f_{USB} and f_{LSB} irrespective of R. Hence, port 1 is used as signal and image port because it ideally presents no insertion loss at the signal and image frequencies irrespective of R. In DSB operation, the image and signal frequencies are not separated because they share the same port (port 1). Port 2 is used as the LO injection port because it presents ideally zero transmission for the LO noise in the sideband frequencies. Assuming a lossless diplexer and as a result of conservation of power, the total power output at port 3 and port 4 due to an input beam at port 1 or port 2 is equal to the total power in the input beam. Hence, any power not exiting from port 3 leaves from port 4, and vice versa. Figure B.2 shows the ideal behavior of $P_{1\to3}$ and $P_{2\to3}$ for $K = 1$ and $R = 0.5$. If R changes between 0.4 and 0.6, this will result in a maximum theoretical insertion loss of 0.18 dB in the LO path (2

3) at the LO frequency. As discussed before, the variation in R does not result in an insertion loss in the signal path at the sideband frequencies.

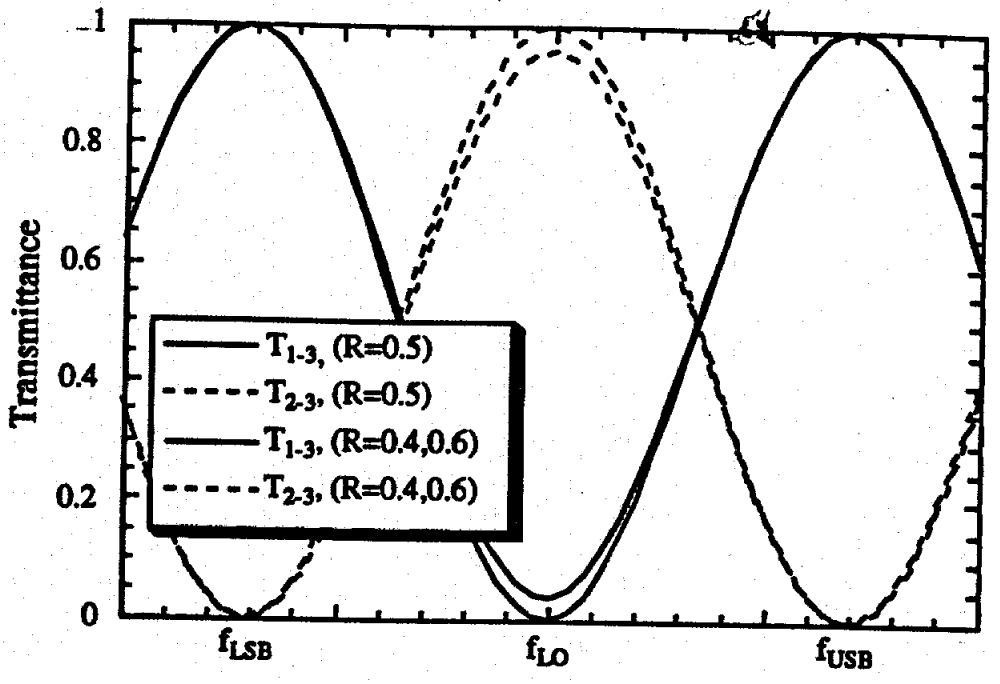

Figure B.2: The Mach-Zender Interferometer response tuned for DSB operation (R =0.4,0.5,0.6 and $K = 1$).

This variation of R with frequency determines the bandwidth over which we can use the interferometer efficiently and this depends on the choice of the beam splitters. Wire grids and dielectric slabs are used as beam splitters and the method of designing them will be explained in the following two sections.

• Wire Grids

Referring to [138, 137, 10], a summary of formulas for designing a wire grid with a specific reflectance is shown below.

$$R = \frac{1}{|1 + (2Z_g/Z_o)|^2} \tag{B.3}$$

$$Z_g/Z_o = i\cos(\theta_i)(ln\csc(\pi a/g))(g/\lambda), \quad \textit{for thin strips of width } 2a \tag{B.4}$$

$$Z_g/Z_o = i\cos(\theta_i)(ln(g/2\pi a))(g/\lambda), \quad \textit{for round wires of radius } a. \tag{B.5}$$

where θ_i is the incidence angle on the mesh. Z_o is the wave impedance of the medium. The equations for Z_g/Z_o are valid for $g \ll \lambda$ and for the incident electric field parallel to the direction of the grid conductors.

The performance of wire grids as partially reflecting mirrors is limited by the absorption loss due to the surface resistance R_s of the metal wires, and to any nonuniformity in the wire spacing.

• Dielectric Slab

For a dielectric slab of thickness d, dielectric constant ϵ_r, attenuation coefficient α, and at a wavelength λ (in air), the reflectance R of the slab to a vertically polarized electric field (TE) incident at an angle θ_i from air side is given by

$$R = \frac{|r^2|(1+(1/L^2)-(2/L)\cos(\delta))}{1+|r|^4-(2/L)Re(r^2e^{-i\delta})} \tag{B.6}$$

where r, δ, and L are defined in the following equations:

$$r = \frac{((1/\sqrt{\epsilon_r})\cos(\theta_i)-\cos(\theta_2))}{((1/\sqrt{\epsilon_r}\cos(\theta_i)+\cos(\theta_2))} \tag{B.7}$$

$$\theta_2 = \sin^{-1}(\sin(\theta_i)/\sqrt{\epsilon_r}) \tag{B.8}$$

$$\delta = 4\pi d\cos(\theta_2)\sqrt{\epsilon_r}/\lambda \tag{B.9}$$

$$L = e^{2\alpha d/\cos(\theta_2)} \tag{B.10}$$

Using the previous equations for r, δ, and L and equation B.6 for R, we can calculate d for a specific R at a specific frequency. The problem has multiple solutions which can be expressed under the form $d = d_0 + md'$, $m = 0, 1, 2, \ldots$ d_0 is the solution which yields to the choice of the thinnest slab and the widest bandwidth for the reflectance [139, 115].

Figure B.3 shows the reflectance R vs. frequency for three fused quartz slabs (ϵ_r=3.826) which are designed to yield a reflectance of 0.5 at 90GHz.

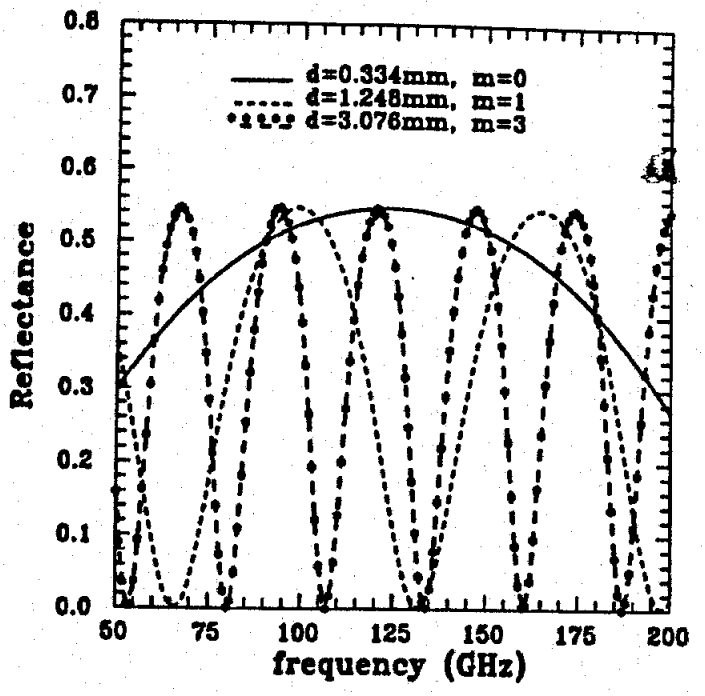

Figure B.3: The reflectance vs. frequency for three fused quartz slabs designed to yield $R = 0.5$ at 90GHz.

The thinnest slab (d_0) yields the widest bandwidth where the insertion loss in the LO path at the LO frequency is less than 0.2dB ($0.4 < R < 0.6$) from 66GHz to 180GHz. The thickest slab (d_2) syields a bandwidth of only 13.3% around 94GHz. As the slab thickness is increased, the periodicity in obtaining $R = 0.5$ at other frequencies increases on the expense of reduction in bandwidth. The limitations in using dielectric slabs, especially at submillimeter-wave frequencies, is the absorption loss in the dielectric and the accuracy in obtaining very thin slabs.

For the two kinds of beam splitters described before, as we mentioned at the beginning, the variation in the reflectance R of the beam splitter around 0.5 will result in an insertion loss in the LO path at the LO frequency. The lost power will exit from port 4 which is normally terminated by a matched load.

• Diffraction Loss

Quasi-optical systems suffer from diffraction of the finite-sized beam in the pres-

ence of quasi-optical elements. Assuming a fundamental-mode Gaussian beam being coupled to either port 1 or port 2 of the Mach-Zender interferometer, this beam will be split in two beams. These two beams will recombine at output port 3 with one of them (beam A) having traveled a longer distance than the other one (beam B) due to the path difference Δ. This means that beam A will have a bigger radius at the output port than beam B. For perfect coupling at the output port, the two beams should have the same beam radii and radii of curvature. Due to the imperfect coupling between beam A and beam B, some power will be lost in the signal path and will be coupled to higher order-mode gaussian beams. This loss is important because it represents an insertion loss in the RF and LO paths, and increases the receiver noise temperature. This insertion loss in the signal and image path (port 1 $\rightarrow$ port 3) [10] can be calculated using Gaussian-beam optics and is expressed as

$$L_{1\rightarrow 3} = [1 - R(1 - \frac{1}{(1+\alpha^2)^{1/2}})]^2 \qquad \text{(B.11)}$$

where $\alpha = \lambda\Delta/2\pi\ w_o^2$. w_o^2 is the beam waist of the input beam. For $R = 0.5$, equation B.11 can be written as

$$L_{1\rightarrow 3} = \frac{1}{4}(1 + \frac{1}{(1+\alpha^2)^{1/2}})^2 \qquad \text{(B.12)}$$

For $\alpha \ll 1$, the power loss in the path 1-3 at the signal and image frequencies is $\alpha^2/2$. The same thing applies for path 2-3 at the LO frequency. As we can see, it is important to keep the path length difference small (K=1), and the waist of the input beam large in order to minimize the overspreading of the delayed beam (and hence increasing α). For a diffraction loss less than 0.1dB ($\alpha^2/2 < 2\%$), we find that w_o must be:

$$w_o \geq (5\Delta\lambda/2\pi)^{1/2} \qquad \text{(B.13)}$$

The most appropriate way to design a dual-beam interferometer is to have the

input beams from ports 1 and 2 converge to the same minimum beam waist in the optical center of the interferometer path, neglecting the path length difference [101]. Also, the input port physical size should be larger than at least 4 times the input beam radius, in order to avoid truncation of the input fundamental-mode Gaussian beam [10]. This truncates the beam at a level of -35dB and conserves 99.97% of the incident power.

Even though the geometry of the Mach-Zender interferometer is simple, it has two main disadvantages :

1. The dependance of the reflectance of the beam splitters on frequency limits the bandwidth of the interferometer.

2. The physical size of the input window of the interferometer as seen in figure B.1 is equal to $d = \lambda_{IF}/4$ for DSB operation with K =1. In most millimeter-wave applications, the input beam will be truncated for this value of d. It is even impossible to use it at higher IF frequencies, without increasing the path difference (K =2,3,..) or reducing the waist of the beam at the center of the interferometer. The latter option will increase the diffraction loss. Other designs do exist make zero path length difference possible, but at the cost of larger size and increased complexity [101].

B.1.2 The Martin-Puplett Interferometer

While initially developed for wideband Fourier transform spectroscopy [140, 141], it is widely used in millimeter and submillimter-wave applications for LO injection or SSB filtering. It is defined as the polarization-rotating dual-beam interferometer. This is due to the fact that the two input ports are separated by using one polarization for one input port and the corresponding orthogonal polarization for the second input

port. The two signals exit the output port with same polarization. Figure B.4 shows the basic geometry of a Martin-Puplett interferometer with input and output grids to separate the two-input ports [10]. There is no need for an output grid if the receiver is sensitive to one polarization, but it is always a good practice to have one so as to send any LO noise in the orthogonal polarization, coming out at the sidebands frequencies, into a matched load at room temperature. The explanation of the MP interferometer is as follows:

The 45° grid divides the input polarization into two orthogonal polarization states. The grid is fully reflective to the polarization state parallel to its wires. The grid wires are at an angle of 35°16' to the plane of the interferometer, since the projection effect of the 45°, incidence will change the angle to 45°. Under these conditions, the 45° grid divides the power of the input beam equally between two orthogonal polarization (R=0.5), and the resulting power transmission expressions are given by:

$$P_{\hat{H}\to\hat{H}} = P_{\hat{V}\to\hat{V}} = \frac{1}{2}[1 + \cos(2\pi\Delta/\lambda)] \tag{B.14}$$

$$P_{\hat{V}\to\hat{H}} = P_{\hat{H}\to\hat{V}} = \frac{1}{2}[1 - \cos(2\pi\Delta/\lambda)] \tag{B.15}$$

where $\Delta = (2K\text{-}1)\lambda_{IF}/2$ for DSB operation. $\hat{H}$ and $\hat{V}$ are horizontal and vertical polarization, respectively.

The paths $\hat{H} \to \hat{H}$ or $\hat{V} \to \hat{V}$ are equivalent to path 2→3 in the case of the Mach-Zender interferometer (see figure B.2). The path $\hat{V} \to \hat{H}$ or $\hat{H} \to \hat{V}$ are also equivalent to path 1→3. Hence, in a Martin-Puplett, the output beams are of the same polarization as the LO input polarization. For example, if the LO is $\hat{H}$ polarized then the signal and image should be $\hat{V}$ polarized, and the resulting output beam will be $\hat{H}$ polarized for $\Delta = 2d = \lambda_{IF}(2K - 1)/2$, where K is 1,2,3,... and for $f_{LO}/f_{IF} = 2n$, where $n = 1,2,3,...$ Note that the input LO and RF beams do not need to be vertically or horizontally polarized as long as they are always orthogonal

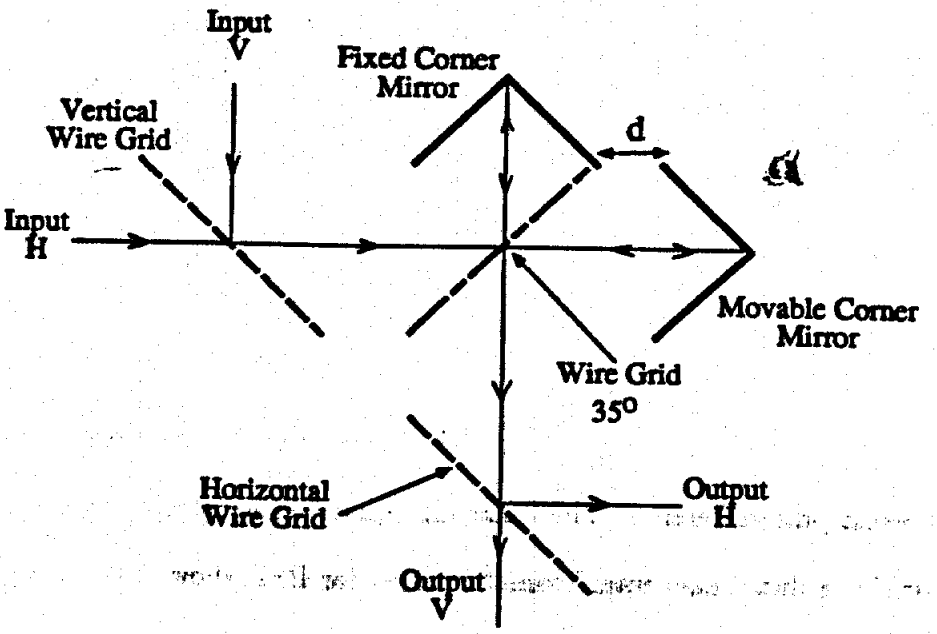

Figure B.4: The geometry of the Martin-Puplett interferometer. The vertical and horizontal wire grids could be interchanged or have the same orientation depending on how the input and output ports polarizations are defined.

to each other in polarization. For $\Delta = 2d = \lambda_{IF}(2K-1)/2$, where K is 1,2,3,.. and for $f_{LO}/f_{IF} = 2n + 1/2$, where n is an integer, we can produce circularly polarized output beams for linearly polarized input beams. Any power not exiting through a port with the correct polarization, due to loss in the path leading to that port or due to off-tuning of the MP interferometer, will exit through the other output port with the corresponding orthogonal polarization.

The wire grid in a Martin-Puplett interferometer is designed to be fully reflective over a broad brand of frequencies. This is easily achieved as long as the wire separation $g \ll \lambda_{min}$, where λ_{min} corresponds to the highest design frequency. This is one of the main advantages of the Martin-Puplett interferometer. Another advantage is the possibility of zero path-length difference without truncating the input beams. Its main drawbacks are that its alignment is critical and its size is still somewhat large for some applications. The design considerations that were mentioned in the Mach-

Zender section still apply here for the Martin-Puplett case. In some applications, a Fabry-Perot resonator is introduced in the LO path of the input beam before the interferometer in order to present a higher rejection to the LO noise in the sidebands frequencies [142].

• Instantaneous Bandwidth of Dual-Beam Interferometers

Previously, it was noted that choosing $K = 1$ in the equation of $\Delta = (2K-1)\lambda_{IF}/2$ results in the lowest diffraction loss because it corresponds to the shortest path difference. The following equation for calculating the IF instantaneous BW for a dual-beam interferometer tuned for DSB shows that $K = 1$ results also in the largest IF instantaneous bandwidth.

$$\delta_{IF} = (1/2)(8/\pi)L^{1/2}[f_{IF}/(2K-1)] \qquad \text{(B.16)}$$

where δ_{IF} is the bandwidth for loss less than L (near maxima) or transmission less than L (near minima). For $L = 0.01$ (better than 20dB rejection), $K = 1$, and $f_{IF} =$ 1.4GHz, $\delta_{IF} = 0.178$GHz (12.7%). For $K = 2$, the IF instantaneous bandwidth is reduced by a factor of 3 (figure B.5).

B.2 SSB Operation of Dual-Beam Interferometer

In the previous section, we showed the operation of a dual-beam interferometer as an LO-injector. The signal and the image frequencies share the same input port. In the case of the operation of a dual-beam interferometer as a single-sideband filter, we need to separate the image from the signal. Quasi-optical dual-beam interferometer elements need to serve the dual functions of LO injection and signal/image separation. No single optical element can perform these simultaneously so it is necessary to cascade filter elements. Before describing a geometry with two quasi-optical filters used to accomplish true SSB filtering, the basic operation of the dual-beam SSB

interferometer filter will be described:

For $\Delta = 2d = (2K-1)\lambda_{IF}/4$ and $f_{image}/f_{IF} = 4n$, where n =1,2,3,.. , figure B.6 shows the response of a dual-beam interferometer tuned for SSB operation ($K = 1$ in this case, and $R = 0.5$ for Mach-Zender). Path $1 \rightarrow 3$ (Mach-Zender) or path $\hat{V} \rightarrow \hat{H}$ (Martin-Puplett) is the signal path, and path $2 \rightarrow 3$ (Mach-Zender) or path $\hat{H} \rightarrow \hat{H}$ (Martin-Puplett) is the image path [10]. We see that we have a 3dB loss at the LO frequency in either signal or image path.

In figure B.7, a configuration of two cascaded Martin-Puplett interferometers have been used to obtain a true single sideband operation (signal/image separation and 100% LO injection) [142, 12]. Interferometer A is tuned for SSB operation ($d_A = \lambda_{IF}/8$). The signal is sent horizontally polarized from port 1 and the image vertically polarized from port 2. The signal and image are combined together in the interferometer and exit both horizontally polarized at port 3. The image port ($\hat{V}$) is terminated with a matched load at port 2. This termination should be as cold and as matched as possible in order to minimize the additive noise due to its temperature. The horizontally polarized signal and image enter now through the $\hat{H}$ port of interferometer B which is tuned for DSB operation (LO injection, $d_B = \lambda_{IF}/4$). The vertically polarized LO signal is injected through the $\hat{V}$ port of interferometer B. At the output $\hat{V}$ port of interferometer, the RF signal, the cold image load and the LO signal exit vertically polarized with ideally no attenuation through their paths.

A hybrid polarizing/Fabry-Perot interferometer has been designed for true single sideband operation but with the advantage that it has a compact size (no need to cascade two interferometers) and can couple the RF signal, the image load and the LO signal to an array of receivers (3×5 array). This is a great piece of quasi-optical design and the reader is referred to [135, 5] for more information.

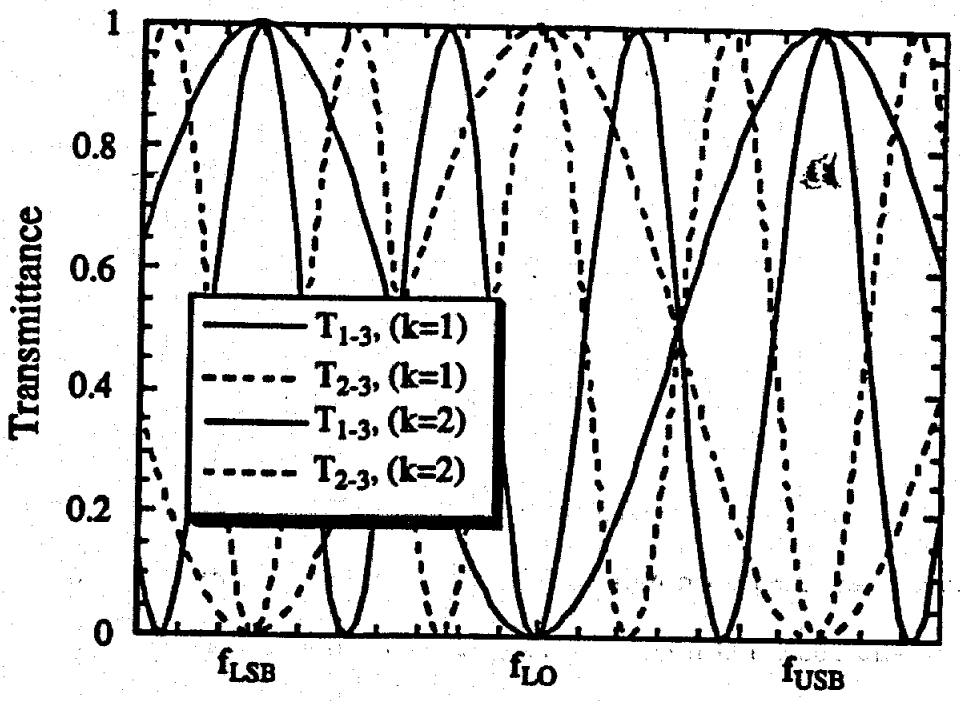

Figure B.5: The response of the dual-beam interferometer when tuned for DSB operation for $K = 1$ and $K = 2$.

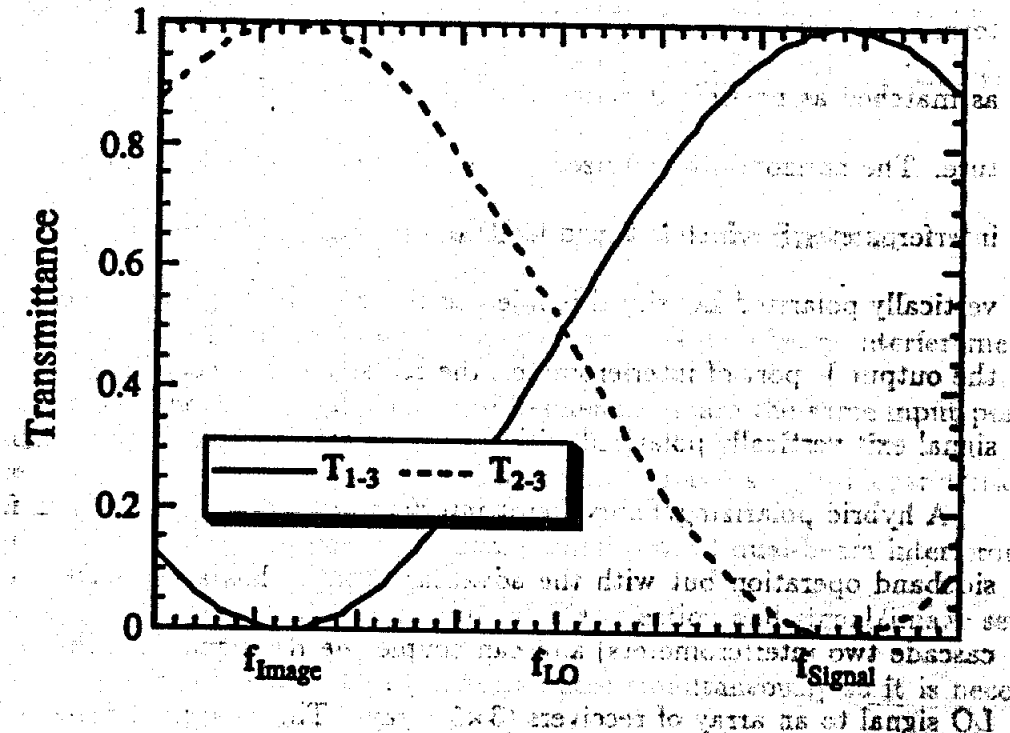

Figure B.6: The response of a dual-beam interferometer as a SSB filter, $K = 1$ ($R = 0.5$ for Mach-Zender).

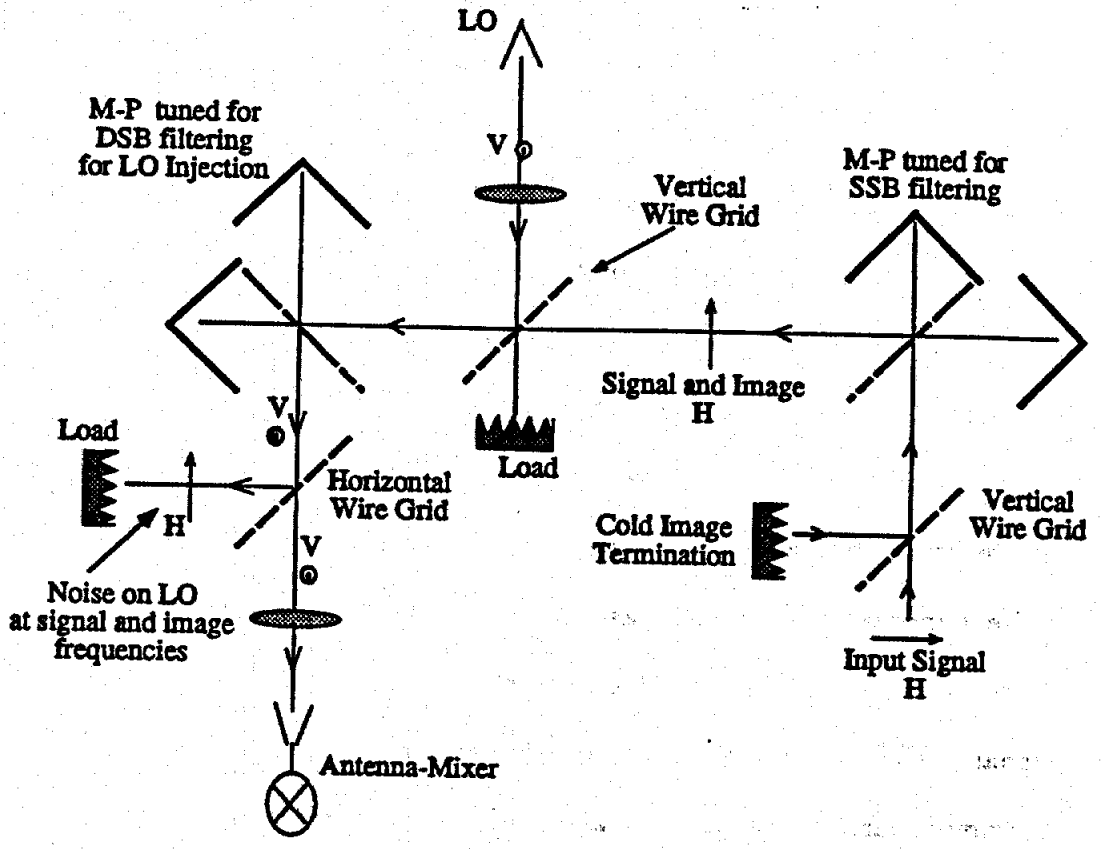

Figure B.7: True single-sideband operation using two Martin-Puplett interferometers in cascade.

APPENDIX C

Mixer Noise Temperature Calculation

In radiometry applications such as radio astronomy and noise measurements, the mixer performance is evaluated on the basis of its equivalent input noise temperature. The definition of the mixer noise temperature depends on the application. When the signal consists of an input at one frequency, the output noise is modeled as if it arises only from an additive source at the signal-frequency input and no noise at the image frequency. This yields to the definition of the *single sideband* (SSB) noise temperature. In radio astronomy, mixing happens at the signal and image frequencies. In this case, the IF output noise power from the mixer and the image and signal (RF) frequency responses are the same as in the previous SSB case; however, the noise source temperature is averaged over both sidebands, the signal and image frequencies respectively. This yields to the definition of the *double sideband* (DSB) noise temperature.

In [110, 143], the DSB and SSB performances of a mixer are related using the following equations:

$$T_M^{SSB} = T_M^{DSB}\left(1+\frac{L_s}{L_i}\right) \tag{C.1}$$

$$L_M^{SSB} = L_M^{DSB}\left(1+\frac{L_s}{L_i}\right) \tag{C.2}$$

where L_s, L_i are the signal and image conversion loss, respectively. L_M and T_M are the mixer conversion loss and equivalent input noise temperature, respectively.

In [105, 144], the various noise contributions to the mixer output noise temperature in a receiver system have been discussed. In this appendix, the mixer conversion loss and equivalent input noise temperature will be derived for a room temperature receiver where the RF and LO signals are coupled using a quasi-optical approach. Equations for the mixer noise temperature are derived for the case when the quasi-optical diplexer is used as a DSB filter and the case when the quasi-optical diplexer is used as a SSB filter (see Appendix B). Finally, a method similar to that described in [105] is presented for measuring the LO source output noise at the sideband frequencies.

C.1 DSB Noise Calculations

In figure C.1, the various contributions to the noise temperature input to the IF chain T_{in}^{IF} are shown and will be discussed starting from left to right in the figure. The signal and image noise powers coming from a load at temperature T_1 are coupled directly to the signal and image port of the quasi-optical diplexer (port 1). The quasi-optical diplexer is tuned for DSB operation. The different types of quasi-optical diplexers and the ports assignments for each type are all discussed in Appendix B. Port 3 is the output port where the RF and LO signals are combined and coupled to the receiver antenna through lens 2. Port 4 is the isolation port and is usually terminated by a load at room temperature. L_{1-3} is the loss in the signal and image path from port 1 to port 3. This loss is the same at both sideband frequencies since the interferometer is tuned for DSB operation. L_{2-3} is the loss in the LO signal path from port 2 to port 3 at both sideband frequencies.

For noise characterization, the quasi-optical diplexer can be looked at as a three-port attenuator, with two inputs (1, 2) and a single output (3). Referring to [110, 105], the noise contribution from the diplexer, at both sideband frequencies, to the output noise temperature at port 3 is :

$$T_{dipl} = T_o(1 - \frac{1}{L_{1-3}} - \frac{1}{L_{2-3}}) \tag{C.3}$$

where T_o is the ambient room temperature.

The total output noise temperature at port 3 is equal to :

$$T_3 = \frac{T_1}{L_{1-3}} + T_{dipl} \tag{C.4}$$

This temperature is attenuated through lens 2 which couples the output of port 3 to the receiver antenna. The noise temperature incident on the antenna is therefore:

$$T_4 = \frac{T_3}{L_2} + T_o(1 - \frac{1}{L_2}) \tag{C.5}$$

where L_2 is the loss of lens 2 at both sideband frequencies, and $T_o(1-(1/L_2))$ is the output noise temperature generated by an attenuator of loss L_2 and at room temperature T_o [110]. T_4 is the signal noise temperature which is input to the antenna-mixer at the USB and LSB frequencies. In the previous calculations, it is assumed that the thermal noise power generated by a load is in direct relationship with its physical temperature T. This is only valid under three assumptions [139]:

1. All the signal noise incident on the antenna is filling the beam of the antenna.
2. The detected power is limited to a narrow bandwidth Δf, such that $\Delta f \ll f$. f is the signal frequency.
3. $hf/kT \ll 1$, which is equivalent to the Rayleigh-Jeans Law.

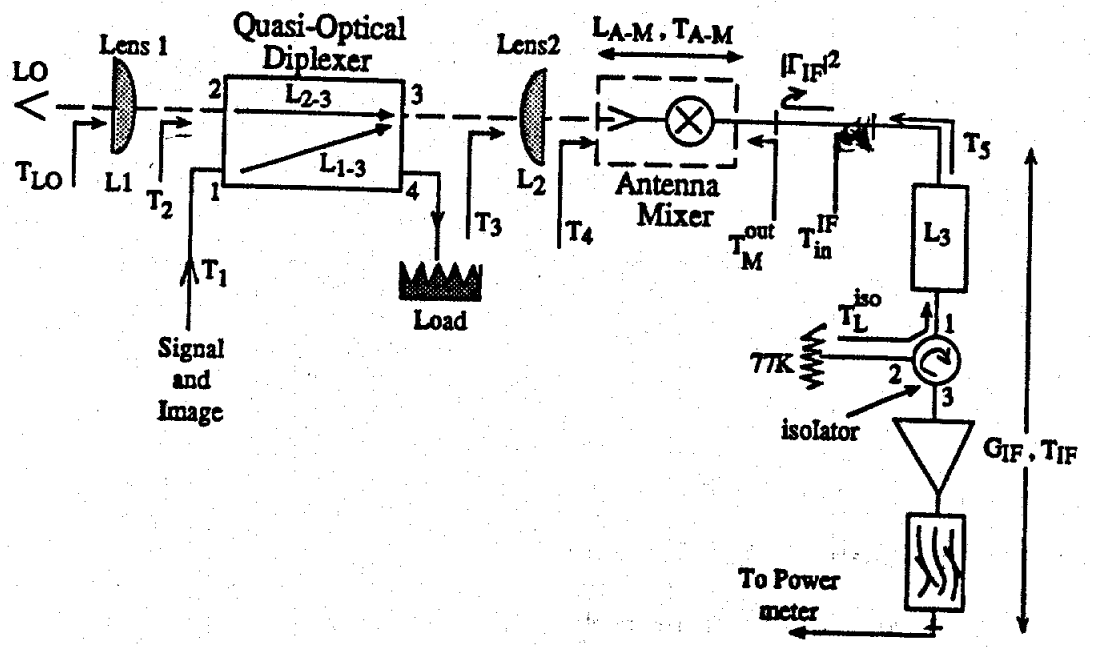

Figure C.1: A quasi-optical receiver with the quasi-optical diplexer tuned as a DSB filter.

The first assumption is satisfied for an antenna with a high Gaussian coupling-efficiency and a quasi-optical receiver system well-designed to couple with minimal loss all the power in the signal to the antenna. The second assumption is usually satisfied since the detected power is limited by the IF filter bandwidth (50-200MHz) which is negligeable compared to the square of the operating siganl frequency (millimeter-wave and submillimeter-wave frequencies). However, the third assumption is valid for microwave and millimeter-wave applications but may not be valid for submillimeter-wave applications and especially for cold signal temperatures. A better approximation [92, 145] can be used in for the effective temperature corresponding to the thermal noise generated at *submillimeter-wave frequencies* by a load of temperature T with the first two assumptions (1,2), previously noted, still satisfied :

$$T' = \frac{hf/k}{[exp(hf/kT) - 1]} \qquad (C.6)$$

where h is Planck's constant (6.63×10^{-34} Joules-sec), k is Boltzmann's constant (1.38×10^{-23} Joules/°K), f is the signal frequency in Hz (the LO frequency can be used since the USB and LSB frequencies are very close to each other at submillimeter-wave frequencies). Under Rayleigh-Jeans Law, the noise temperature of a load is equal to its physical temperature T. Using equation C.6, the actual noise temperature detected from a load with a temperature T=85K (assumed under Rayleigh-Jeans law) at 350GHz is 77K (10% error). For T=295K and f=350GHz, the error is only 3%. The actual noise temperatures are lower than the ones under the Rayleigh-Jeans Law. Hence, in equations C.3 - C.5 and for submillemeter-wave frequencies, noise temperatures T_1 and T_2 should be replaced by the corresponding effective temperatures corrected using equation C.6.

In the following equations, we characterize the antenna-mixer performance and not the mixer diode only since in our circuits, the antenna is an integral part of the mixer design. As mentioned in the beginning, for the DSB case, the IF output noise power corresponding to the *internal* noise generated by the antenna-mixer is assumed to come equally from both sidebands. The available noise temperature (power into a matched load) at the IF output of the antenna-mixer is :

$$T_M^{out} = \frac{(T_s + T_{A-M})}{L_s} + \frac{(T_i + T_{A-M})}{L_i} \qquad (C.7)$$

where T_{A-M} is the antenna-mixer DSB equivalent input noise temperature, and L_s and L_i are the antenna-mixer responses at the signal and image frequencies, respectively. Referring to C.1, we can write the previous equation as

$$T_M^{out} = \frac{(T_s + T_{A-M})}{L_{A-M}} \qquad (C.8)$$

where $1/L_{A-M} = (1/L_s + 1/L_i)$ is the DSB antenna-mixer conversion loss.

Normally, the IF output impedance of the mixer differs from 50Ω which results in a

mismatch between the antenna-mixer output and the IF chain input. This mismatch at the IF frequency is denoted in figure C.1 by the IF power reflection coefficient $|\Gamma_{IF}|^2$ and can be measured using the method described in chapter 3, section 3.2.5. The IF chain is defined from the mixer output to the input of the power meter at the other end of the chain. The IF chain is calibrated right at the mixer ouput port using the normal hot-cold load method and is characterized by an equivalent input noise temperature T_{IF} and a gain G_{IF}. It is important to have an isolator after the mixer output port in order to insure the proper operation of the IF amplifiers which need to see a source impedance of 50Ω. Port 2 of the isolator is normally connected to a load at a temperature T_{iso}^L (either room temperature T_o or a cold temperature ~80-85K, since the coaxial cable connecting the cold isolator load to the isolator port is not totally dipped in liquid nitrogen [105]). This noise temperature T_{iso}^L travels back to the mixer output port because of the low insertion loss between ports 2 and 1 of the isolator. In a normal set-up, there will be some attenuation in the path of T_{iso}^L. This attenuation L_3 includes the insertion loss between ports 2 and 1 of the isolator at the IF frequency and the loss due to the presence normally of a bias-T, an IF cable or a coupler between the mixer and the isolator. We can write the noise temperature incident on the mixer output port from the isolator direction as

$$T_s = \frac{T_{iso}^L}{L_3} + T_o(1 - \frac{1}{L_3}) \quad \text{(C.9)}$$

Part of this noise temperature T_s will be reflected back into the IF chain due the non-zero value of $|\Gamma_{IF}|^2$, and is added to the available output noise temperature T_M^{out} from the antenna-mixer port which is attenuated by a factor of $(1-|\Gamma_{IF}|^2)$. The total DSB noise temperature input to the IF chain can be expressed as

$$T_{in}^{IF} = T_M^{out}(1 - |\Gamma_{IF}|^2) + T_s|\Gamma_{IF}|^2 \quad \text{(C.10)}$$

The total output noise power available at the IF chain output which is connected to a calibrated power meter is

$$P_{out}^{IF} = G_{IF}k(T_{in}^{IF} + T_{IF})B \tag{C.11}$$

where k is Boltzmann's constant (1.38×10^{-23} Joules/°K) and B is the bandwidth of the IF chain which is normally limited by the bandpass filter in the chain [110]. Going through some algebra, we can express the previous equation as

$$P_{out}^{IF} = kB\frac{G_{IF}}{L_{rcvr}}(T_1 + T_{rcvr}) \tag{C.12}$$

where P_{out}^{IF} is the available noise power at the IF chain output corresponding to an RF load of temperature T_1 available at port 1 of the quasi-optical diplexer. Note at submillimeter-wave frequencies, we replace T_1 by T_1' using equation C.6. L_{rcvr} and T_{rcvr} are the DSB receiver conversion loss and the DSB receiver equivalent input noise temperature at port 1 of diplexer, respectively.

$$L_{rcvr} = \frac{L_{A-M}L_{1-3}L_2}{(1-|\Gamma_{IF}|^2)} \tag{C.13}$$

$$T_{rcvr} = T_{A-M}L_{1-3}L_2 + T_s(L_{1-3}L_2 - \frac{L_{1-3}}{L_{1-3}} - 1) + (T_s|\Gamma_{IF}|^2 + T_{IF})\frac{L_{A-M}L_{1-3}L_2}{(1-|\Gamma_{IF}|^2)} \tag{C.14}$$

L_{rcvr} and T_{rcvr} are measured using the normal hot-cold load method [102, 103]:

$$L_{rcvr} = G_{IF}/(\frac{P_{out,H}^{IF} - P_{out,C}^{IF}}{kB(T_{1,H} - T_{1,C})}) \tag{C.15}$$

$$T_{rcvr} = \frac{T_{1,H} - YT_{1,C}}{Y-1} \tag{C.16}$$

$$Y = \frac{P_{out,H}^{IF}}{P_{out,C}^{IF}} \tag{C.17}$$

Solving equations C.13 - C.17, we can find the expressions for the DSB antenna-mixer conversion loss L_M and the DSB antenna-mixer equivalent input noise temper-

ature T_M :

$$L_{A-M} = \frac{L_{recvr}(1-|\Gamma_{IF}|^2)}{L_{1-3}L_2} \tag{C.18}$$

$$T_{A-M} = \frac{(T_{recvr} - T_o(L_{1-3}L_2 - \frac{L_{1-3}}{L_{2-3}} - 1) - ([\frac{T_{mix}^L}{L_3} + T_o(1-\frac{1}{L_3})]|\Gamma_{IF}|^2 + T_{IF})L_{recvr})}{L_{1-3}L_2} \tag{C.19}$$

Knowing T_{recvr}, L_{recvr}, the path losses L_{1-3} and L_{2-3} in the quasi-optical diplexer, and the losses L_2 and L_3, we can solve for T_{A-M} and L_{A-M}. Note that at submillimeter-wave frequencies, $T_{1,HorC}$ and T_o in equation C.3 should be each replaced by their corrected effective temperature using equation C.6.

LO sources are not ideal sources, and they produce noise power at the the sidebands frequencies. This output noise power T_{LO} is attenuated first by L_1 (loss in lens 1 at the sidebands frequencies), second by L_{2-3} (loss in the diplexer LO response at the sidebands frequencies), and third by L_2 (loss in lens 2 at the sidebands frequencies). This noise power reaching the mixer will increase the DSB antenna-mixer equivalent input noise temperature. Hence, the corrected value of T_M should be

$$T_{A-M}^{corrected} = T_{A-M} - \frac{T_{LO}}{L_1 L_{2-3} L_2} \tag{C.20}$$

This term $T_{LO}/L_1L_{2-3}L_2$ is negligeable for the case of Gunn diode based LO sources, assuming a 20dB rejection of the sidebands in the LO path through the diplexer (L_{2-3}). However, for the case when a carcinotron is used as the LO source, the noise generated by the carcinotron in the sidebands can be as high as 50,000K [17], and even with high sidebands rejection in the LO path, the term $T_{LO}/L_1L_{2-3}L_2$ can be in the order of 100-500K. This is also true for IMPATT diode based LO sources.

C.2 SSB Noise Calculations

In the case of a quasi-optical diplexer tuned as a SSB filter as shown in Figure C.2, the diplexer has 3 input ports and two output ports because there is a need for LO injection and signal/image seperation as discussed in Appendix B. The signal port sees a noise temperature T_s. The image port is terminated by a load of temperature T_i. This image termination should be made as cold and as well matched as possible in order to mimimize the additive noise due to its temperature [12]. The LO is injected through port 2. The output port is port 3 and is coupled to the receiver antenna through lens 2. Port 4 is the isolation port and is terminated by a load. In the following calculations, we consider that there is no power from the image load appearing at the signal frequency, and vice versa. This is based on the assumption that the SSB filter has a good signal to image rejection ratio at the signal frequency and vice versa, and which is valid normally. Hence, *at the signal frequency*, we can follow the same method as in the DSB case and we can express the output noise temperature at port 3 as:

$$T_3^s = \frac{T_s}{L_{s-3}^s} + T_o\left(1 - \frac{1}{L_{s-3}^s} - \frac{1}{L_{2-3}^s}\right) \tag{C.21}$$

where $T_o(1\text{-}1/L_{s-3}^s - 1/L_{2-3}^s)$ is the diplexer equivalent input noise temperature at the signal frequency due to the loss L_{s-3}^s in the signal path and the loss L_{2-3}^s in the LO path.

At the image frequency, the output noise temperautre at port 3 is

$$T_3^i = \frac{T_i}{L_{i-3}^i} + T_o\left(1 - \frac{1}{L_{i-3}^i} - \frac{1}{L_{2-3}^i}\right) \tag{C.22}$$

where $T_o(1\text{-}1/L_{i-3}^i - 1/L_{2-3}^i)$ is the diplexer equivalent input noise temperature at the image frequency due to the loss L_{i-3}^i in the image path and the loss L_{2-3}^i in the LO

path. T_o is the ambient room temperature. Port 3 is coupled to the receiver antenna through lens 2 of loss L_2 at both sideband frequencies. The noise temperatures incident on the antenna-mixer at the signal and image frequencies are :

$$T_4^{s,i} = \frac{T_3^{s,i}}{L_2} + T_o(1 - \frac{1}{L_2}) \tag{C.23}$$

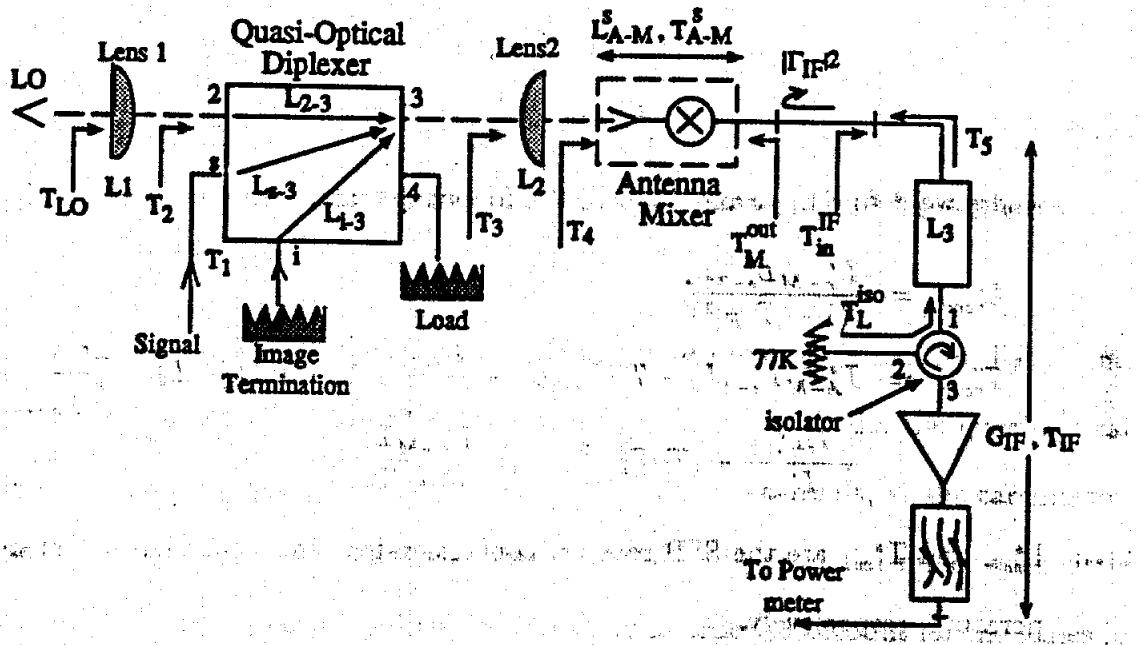

Figure C.2: A quasi-optical receiver with the quasi-optical diplexer tuned as a SSB filter.

In the SSB case, It is assumed that the signal and image antenna-mixer responses are equal, and the IF output noise power generated by the mixer comes entirely from the signal band. The total IF output noise temperature available at the mixer output, corresponding to the noise power in T_4^s and T_4^i detected by the antenna-mixer, and to the internal antenna-mixer noise power generated at the signal frequency is equal to

$$T_M^{out} = \frac{(T_4^s + T_4^i + T_{A-M}^s)}{L_{A-M}^s} \tag{C.24}$$

where T^s_{A-M} is the antenna-mixer SSB equivalent input noise temperature, and L^s_{A-M} is the antenna-mixer SSB conversion loss. Reaching this point where we have defined T^{out}_M, we can follow the same equations used for the DSB case to calculate the IF power at the output of the IF chain corresponding to a signal with a noise temperature T_s and an image termination at a temperature T_i. After going through the algebra, we can write the expression of the IF power available at the output of the IF chain as

$$P^{IF}_{out} = kB\frac{G_{IF}}{L_{recvr}}(T_s + T_{recvr}) \tag{C.25}$$

where we define L_{recvr} and T_{recvr} in the following equations:

$$L^s_{recvr} = \frac{L^s_{A-M}L^s_{s-3}L_2}{(1-|\Gamma_{IF}|^2)} \tag{C.26}$$

$$\begin{aligned} T^s_{recvr} = {} & T^s_{A-M}L^s_{s-3}L_2 + T_o(L^s_{s-3}L_2 - \frac{L^s_{s-3}}{L^s_{2-3}} - 1) + T_o(L^s_{s-3}L_2 - \frac{L^s_{s-3}}{L^i_{2-3}} - \frac{L^s_{s-3}}{L^i_{i-3}}) \\ & + \frac{T_iL^s_{s-3}}{L^i_{i-3}} + (T_s|\Gamma_{IF}|^2 + T_{IF})\frac{L^s_{A-M}L^s_{s-3}L_2}{(1-|\Gamma_{IF}|^2)} \end{aligned} \tag{C.27}$$

L^s_{recvr} and T^s_{recvr} are the SSB receiver conversion loss and equivalent input noise temperature, respectively.

Using equation C.15 - C.17 as in the DSB case, we solve for L^s_{recvr} and T^s_{recvr}. Then using equations C.26 and C.27, we can calculate the SSB antenna-mixer conversion loss L^s_{A-M} and the SSB antenna-mixer equivalent input noise temperature T^s_{A-M}:

$$L^s_{A-M} = \frac{L^s_{recvr}(1-|\Gamma_{IF}|^2)}{L^s_{s-3}L_2} \tag{C.28}$$

$$\begin{aligned} T^s_{A-M} = {} & [T^s_{recvr} - T_o(L^s_{s-3}L_2 - \frac{L^s_{s-3}}{L^s_{2-3}} - 1) - T_o(L^s_{s-3}L_2 - \frac{L^s_{s-3}}{L^i_{2-3}} - \frac{L^s_{s-3}}{L^i_{i-3}}) \\ & - \frac{T_iL^s_{s-3}}{L^i_{i-3}} - (\frac{T^D_{iso}}{L_3} + T_o(1-\frac{1}{L_3}))|\Gamma_{IF}|^2 + T_{IF})L^s_{recvr})]/(L^s_{s-3}L_2) \end{aligned} \tag{C.29}$$

Note that at submillimeter-wave frequencies, $T_{s,HorC}$, T_i, and T_o, appearing in equations C.21-C.23, should be each replaced by their corrected effective temperature using equation C.6.

In the SSB case, The LO noise power reaching the antenna-mixer *at both sideband frequencies* will increase the SSB antenna-mixer equivalent input noise temperature T^s_{A-M}. The corrected value of T^s_{A-M} is

$$T^{s,corrected}_{A-M} = T^s_{A-M} - \frac{T_{LO}}{L_1 L^s_{2-3} L_2} - \frac{T_{LO}}{L_1 L^i_{2-3} L_2} \qquad \text{(C.30)}$$

In the SSB case, the image port of the mixer is assumed noiseless. As a result, all noise powers appearing at the signal and image frequencies are added when referring them to the signal port.

C.3 Measurements of the LO noise power in the sidebands frequencies

Going back to the DSB case, and assuming we obtained a certain T_{A-M} and a certain L_{A-M} for a specific rectified current in the mixer diode, the quasi-optical diplexer is removed from the set-up of figure C.1 [105]. As a result, all the carcinotron noise power in both sidebands is allowed to go directly into the mixer with little attenuation. The LO power is readjusted slightly in order to account for the losses in the diplexer, and thereby, the antenna-mixer T_{A-M} and L_{A-M}, and the IF reflection coefficient are the same as before. The IF power measured at the output of the IF chain can be expressed as :

$$P^{IF}_{out} = G_{IF} k [(\frac{T_{LO}}{L_1 L_2} + T_o(1 - \frac{1}{L_1 L_2}) + T_{A-M}) \frac{(1 - |\Gamma_{IF}|^2)}{L_{A-M}} + |\Gamma_{IF}|^2 [\frac{T^L_{iso}}{L_3} + T_o(1 - \frac{1}{L_3})] + T_{IF}] B \qquad \text{(C.31)}$$

Using the power meter to measure P^{IF}_{out}, and knowing all the variables in equation C.31 from previous calculations and measurements, we can deduce the value of T_{LO} at the sidebands frequencies.

APPENDIX D

Fabrication of Trenches and V-Grooves in Silicon

D.1 Micromachining of V-Grooves

In the integrated receiver structure presented in chapter 3 for 90GHz, 250GHz, and 335GHz, a V-groove has been etched in the sidewall (B) below the CPS line which is integrated on the membrane (see Fig. 3.4). Figure D.1 (left) shows the etching mask for the V-groove opening and the pyramidal cavity opening next to it. This etching mask has two convex corners in it. Convex corners, in general, will be undercut by anisotropic etches at a rate determined by the magnitude of the maximum etch rate, by the etch rate ratios for various crystallographic planes, and by the amount of local surface area being actively attacked [68]. For etchants with a fast convex undercut rate such as EDP (Ethylene Diamine, Pyrocathecol, H_2O solution), the 90° corners are undercut and the V-groove is widened (Fig. D.1 (right)).

In a paper by Bean et al. [69], it is seen that corner undercutting is related to etch depth. Data relating corner undercutting to etch depths are used to design corner compensations into the mask to prevent the faceted or rounded corners [69]. However, these corner compensations are only good in the case of small etch depth in comparison to the opening in the mask.

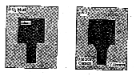

Figure D.1: The V-groove mask pattern (left). This mask pattern can result in a substantial degree of undercutting using an etchant with a fast convex undercut rate such as EDP (right).

In our case, the etching of the V-groove requires a big etch depth, approximately equal to 70% of the groove opening (1/tan(35.3°)). In addition, the etching does not stop when the V-groove apex is reached, but continues till the wafer is completely etched through, as seen in Fig. D.2. Hence, the corner compensations need to be considerably large in our case. However, the results were not good as found experimentally. Significant tips were left sticking out at each corner, and the overetching of the wafer, of course, undercut the corners.

Better results were obtained using the mask shown in Fig. D.3. The opening mask for the V-groove and the one for forming the sidewalls of this part of the horn structure were separated by a gap of 10μm. Hence, in this new mask design, we do not have any convex corners. As a result, the etchings of the V-groove and of the sidewalls are done separately initially. The solution used for etching is KOH/H$_2$O at 80°C. It is preferred over EDP because it exhibits much higher <100> to <111> etch

rate ratios than EDP and hence the etching rate through silicon is slower. Normally, during etching, there is an additional widening of the openings, due to the inherent misalignment between the wafer and the mask during exposure. Hence, the gap between the two opening masks is reduced, and the wall separating the V-groove from the pyramidal cavity is thinned down during etching. At a certain level (close to the end of etching), this wall breaks and is etched away. At the end of etching, the convex corners obtained are minimally undercut (Fig. D.4).

D.2 Micromachining of Trenches

In the 330GHz receiver design, V-trenches have been etched 50μm to 75μm away from the membrane wafer sidewalls (Fig. 3.28). The trenches are 130-140μm deep. They are fabricated with the following procedure:

1. Pattern the membrane wafer front side which is from the horn aperture side.
2. Etch away the exposed $SiO_2/Si_3N_4/SiO_2$ trilayer, while protecting the membrane from the wafer back side on which the mixer circuit are to be integrated.
3. Etch 10-15μm from the exposed silicon (20-30min in a KOH/H_2O solution at 60°C).
4. Clean wafer in a 1:1 H_2SO_4:H_2O_2 solution for 1min.
5. Pattern the wafer back side with the trenches mask using backside infrared alignment (the trenches mask pattern is aligned to the square opened in the front side of the wafer by the previous steps).
6. Etch away the exposed $SiO_2/Si_3N_4/SiO_2$ trilayer in the trenches pattern, while protecting the wafer front side.

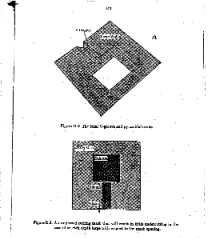

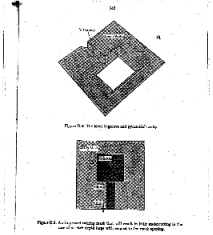

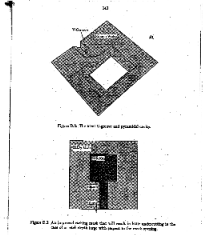

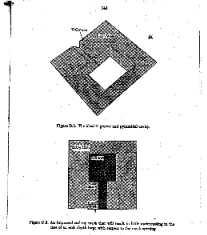

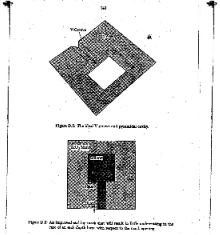

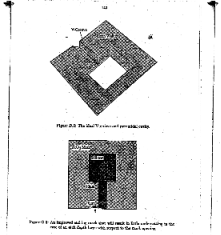

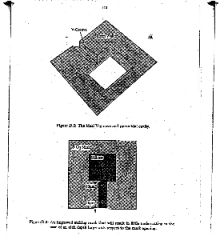

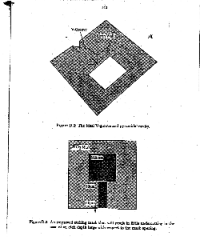

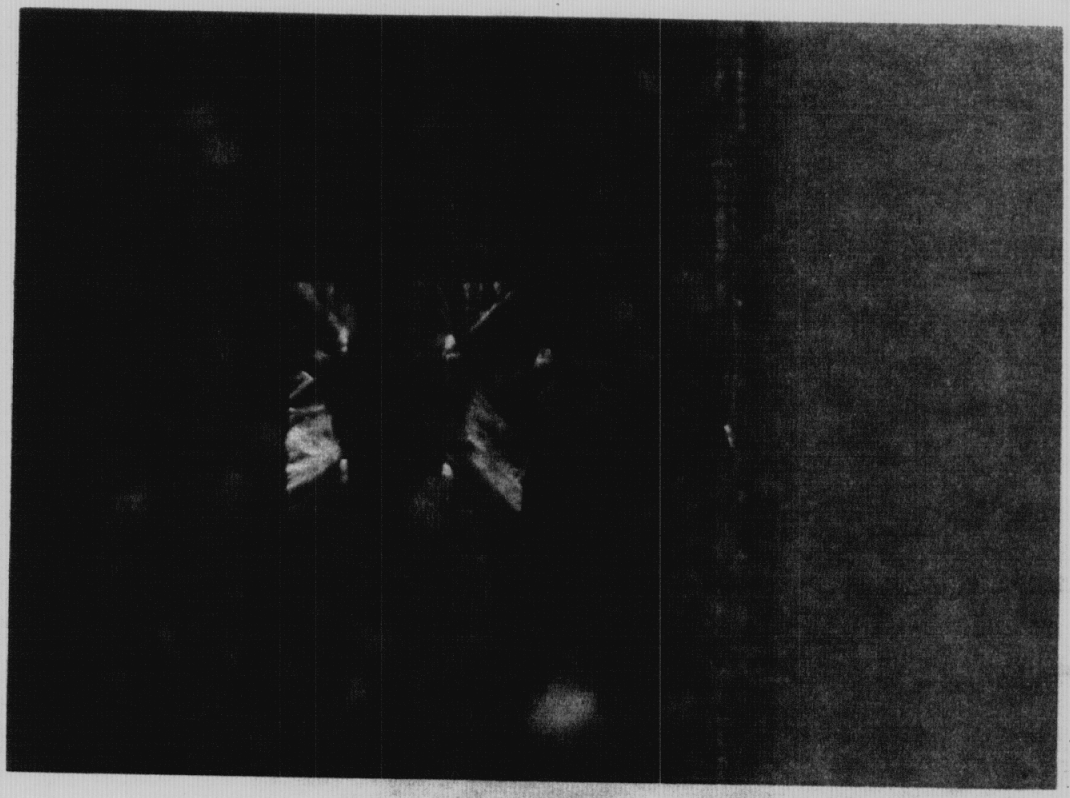

Figure D.4: The V-groove fabricated for the 330GHz receiver structure.

7. The wafer is then dipped in the 60°C KOH/H_2O solution in order to be etched from the front and back sides. Etching the trenches and etching through the wafer to reach the membrane are done almost at the same time.

After cleaning the wafer, the mixer integration on the membrane and the silicon substrate is done with the trenches present around the membrane. Even though the surface on which the mixer is integrated is not totally planar, the mixer circuitry was integrated successfully using the following lift-off process:

1. spin Shipley1470 at 5K rpm for 30sec.
2. Bake for 15min. in a 60° oven.
3. Soak in Chlorobenzene for 11min.
4. Bake for 15min in a 90° oven.
5. Develop in a 5:1 MF319:DI-H_2O solution for 2min.

The Shipley1470 [146] is suitable for this kind of process because it is a thin photoresist, unlike the Shipley1350J.

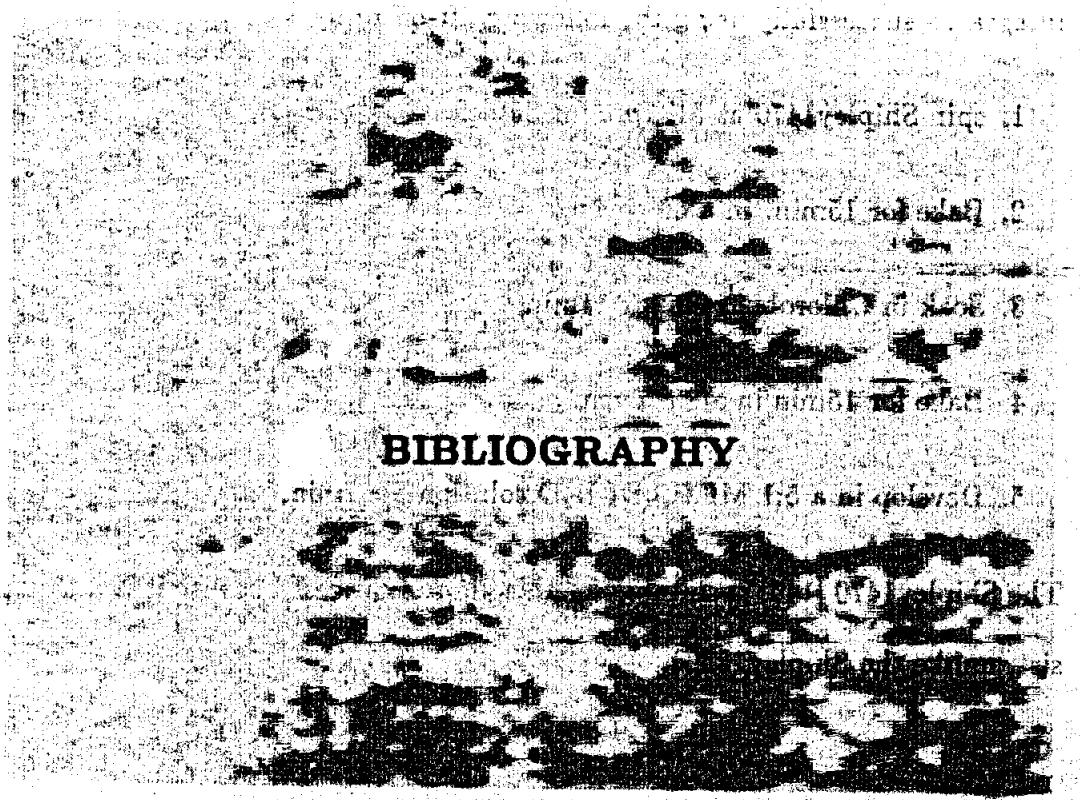

Figure D.4: The V-groove fabricated for the 330GHz resonant structure.

BIBLIOGRAPHY

[1] J. W. Waters, "Microwave Limb-Sounding of earth's upper atmosphere," *Atmospheric Research,* vol. 23, pp. 391-410, 1989.

[2] J. M. Payne, "Millimeter and Submillimeter-Wavelength Radio Astronomy," *Proc. IEEE,* vol. 77, pp. 993-1017, 1989.

[3] W. J. Wilson, R. J. Howard, A. C. Ibbott, G. S. Parks, and W. B. Ricketts, "Millimeter-Wave Imaging Sensor," *IEEE Trans. Microwave Theory Tech.,* vol. 34, pp. 1026-1035, 1986.

[4] K. Miyanchi, "Millimeter-Wave Communications," *Infrared and Millimeter Waves,* vol. 9, K.J. Button, ed., New York : Academic, 1983, pp. 1-94.

[5] N. R. Erickson, P. F. Goldsmith, G. Novak, R. M. Grosslein, P. J. Viscuso, R. B. Erickson, and C. Read Predmore, "A 15 element focal plane array for 100GHz," *IEEE Trans. Microwave Theory Tech.,* vol. 40, pp. 1-11, Jan. 1992.

[6] A. R. Webb, "Point source location using a millimeter-wave focal plane array radar," *IEE Proc. Part F, Radar and Signal Processing,* pp. 581-591, Dec. 1991.

[7] Y. Takimoto, and M. Kotaki, "Automotive anticollision radar," *Applied Microwave Magazine,* Fall 1982.

[8] T. Rose, "Intelligent Vehicle Highway Systems: Going Places Fast," *Microwave Journal,* pp. 172-178, May 1993.

[9] Special Issue on Millimeter-Wave Scattering and Propagation, *Trans Geosci. Remote Sensing,* vol. 26, May 1988.

[10] P. F. Goldsmith, "Quasi-optical techniques at millimeter and submillimeter wavelengths," *Infrared and Millimeter Waves,* vol. 6, K. J. Button, Ed., New York: Academic, 1982.

[11] P. F. Goldsmith, "Quasi-optics in radar systems," *Microwave Journal,* pp. 79-98, Jan. 1991.

[12] N. R. Erickson, "A very low-noise single-sideband receiver for 200-260GHz," *IEEE Trans. Microwave Theory Tech.,* vol. 33, pp. 1179-1188, Nov. 1985.

[13] J. W. Archer and M. T. Faber, "Low-noise, fixed-tuned, broadband mixer for 200-270GHz," *Microwave Journal*, pp. 135-142, July 1984.

[14] P.J. B. Clarricoats and A. D. Olver, *Corrugated Horns for Microwave Antennas* (IEE Electromagnetic Waves, Series 18). London: Peter Peregrinus, 1984.

[15] P. D. Potter, "A new horn with suppresses sidelobes and equal beamwidths," *Microwave Journal*, vol. 6, pp. 71-78, June 1963.

[16] A. W. Love, ed. (1976), *Electromagnetic Horn Antennas*, IEEE Press, New York.

[17] N. R. Erickson, "A 200-350GHz heterodyne receiver," *IEEE Trans. Microwave Theory Tech.*, vol. 29, pp. 557-561, June 1981.

[18] A. R. Kerr, R. J. Mattauch, and J. A. Grange, "A new mixer design for 140-220GHz," *IEEE Trans. Microwave Theory Tech.*, vol. 25, pp. 399-401, May 1977.

[19] N. Keen and G. Ediss, "Measurements of a waveguide Schottky barrier mixer at 690GHz," in *Proc. 21th European Microwave Conf.*, 1991.

[20] L. K. Seidel and T. W. Crowe, "Fabrication and analysis of GaAs Schottky Barrier diodes fabricated on thin membranes for terahertz applications," *Int. J. Infrared and Millimeter Waves*, vol. 10, no. 7, pp. 779-787, 1989.

[21] C. R. Predmore, A. V. Raisanen, N. R. Erickson, P. F. Goldsmith, and J.L. R. Marrero, "A broad-band, ultra low-noise Schottky diode mixer receiver from 80 to 115GHz," *IEEE Trans. Microwave Theory Tech.*, vol. MTT-32, pp. 498-507, May 1984.

[22] K. Mills, F. Azan, H. Perruche, P. Boireau, and J. Lacombe, "Glass reinforced GaAs beam lead Schottky diode with airbridge for millimeter wavelengths," *Electron Lett.*, vol. 20, no. 19, pp. 787-788, Aug. 1984.

[23] N. J. Cronin and V. J. Law, "Planar millimeter-wave diode mixer," *IEEE Trans. Microwave Theory Tech.*, vol. 33, pp. 827-830, Sept. 1985.

[24] J. A. Calviello, J. L. Wallace, and P. R. Bie, "High performance GaAs beam lead mixer diodes for millimeter and submillimeter applications," *Electron. Lett.*, vol. 15, pp. 509-510, Aug. 1979.

[25] W. L. Bishop, K. McKinney, R. J. Mattauch, T. W. Crowe, and G. Green, "A Novel whiskerless Schottky diode for millimeter- and submillimeter-wave application," *IEEE MTT-S Int. Microwave Symp.*, Digest, Las Vegas, NV, pp. 607-610, June 1987.

[26] D. G. Garfield, R. J. Mattauch, and S. Weinreb, "RF Performance of a Novel Planar Millimeter-Wave Diode Incorporating an Etched Surface Channel," *Trans. Microwave Theory Tech.*, vol. MTT-39, pp. 1-5, Jan 1991.

[27] J. W. Archer, R. A. Batchelor, and C. J. Smith, "Low-Parasitic, Planar Schottky Diodes for Millimeter-Wave Integrated Circuits," *IEEE Trans. Microwave Theory Tech.*, vol. MTT-38, pp. 15-22, Jan. 1990.

[28] P. H. Siegel, R. J. Dengler, I. Mehdi, W. L. Bishop, and W. Crowe, "A 200GHz Planar diode Subharmonically Pumped Waveguide Mixer with State-of-the-Art Performance," in *IEEE MTT-S Int. Microwave Symp. Digest*, pp. 595-598, Albuquerque, NM, June1992.

[29] T. Newman, W. L. Bishop, K. T. Ng, and S. Weinreb, "A Novel Planar Diode Mixer for Submillimeter-Wave Applications," *Trans. Microwave Theory Tech.*, vol. MTT-39, pp. 1964-1971, Dec. 1991.

[30] P. T. Parrish, A. G. Cardiasmenos, and I. Galin, "94GHz beam-lead balanced mixer," *IEEE Trans. Microwave Theory Tech.*, vol. MTT-29, pp. 1150-1157, Nov. 1981.

[31] P. L. Richards, T. M. Shen, R. E. Harris, and F. L. Loyd, "Quasiparticle heterodyne mixing in SIS tunnel junctions," *Appl. Phys. Lett.*, vol. 34, pp. 345-347, Mar. 1979.

[32] P. L. Richards and T. M. Shen, "Superconductive devices for millimeter wave detection, mixing, and amplification," *IEEE Trans. Electron Devices*, vol. ED-27, pp. 1909-1920, Oct. 1980.

[33] S.K. Pan, A. R. Kerr, M. J. Feldmah, A. W. Kleinsasser, J.W. Stasiak, R.L. Sandstrom, and W.J. Gallagher, "An 85-116GHz SIS receiver using inductively shunted edge junctions," *IEEE Trans. Microwave Theory Tech.*, vol. MTT-37, pp. 580-592, Mar. 1989.

[34] L. R. D'Addario, "An SIS mixer for 90-120GHz with gain and wide bandwidth," *Int. J. Infrared and Millimeter Waves*, vol. 5, no. 11, pp. 1419-1442, 1984.

[35] A. R. Kerr and S. K. Pan, "Some recent developments in the design of SIS mixers," *Int. J. Infrared and Millimeter Waves*, vol. 11, no. 10, pp. 1169-1187, 1990.

[36] E. C. Sutton, "A superconducting Tunnel Junction Receiver for 230GHz," *IEEE Trans. Microwave Theory Tech.*, vol. MTT-31, pp. 589-592, July 1983.

[37] B. N. Ellison, P. L. Schaffer, W. Schaal, D. Vail, and R. E. Miller, "A 345GHz SIS receiver for radioastronomy," *Int. J. Infrared and Millimeter Waves*, vol. 10, no. 8, pp. 937-947, 1989.

[38] T. H. Buttgenbach, H. G. LeDuc, P. D. Marker, and T. G. Phillips, "A fixed tuned broadband matching structure for submillimeter SIS receivers," *IEEE Trans. Applied Superconductivity*, vol. 2, pp. 165-175, Sept. 1992.

[39] C. E. Honingh *et al.*, "Performance of a two-junction-array SIS-mixer around 345GHz," *IEEE Trans. Microwave Theory Tech.*, vol. 41, pp. 616-623, April 1993.

[40] H. R. Fetterman *et al.*, "Far-IR heterodyne radiometric measurements with quasi-optical Schottky diode mixers," *Appl. Phys. Lett.*, vol. 33, pp. 151-154, 1978.

[41] E. N. Grossman, "The coupling of submillimeter-wave corner-cube antennas to Gaussian beams," *Infrared Phys.*, vol. 29, pp. 875-885, 1989.

[42] J. Zmuidzinas, A. L. Betz, and R. T. Boreiko, "A corner-reflector mixer for far-infrared wavelengths," *Infrared Phys.*, vol. 29, pp. 119-131, 1989.

[43] C. R. Seachore, "Integarted-circuit transducers," *Infrared and Millimeter Waves*, vol. 14, K.J. Button, Ed., New York: Academic, 1985.

[44] K. Chang, "Planar Integrated Circuits," *Infrared and Millimeter Waves*, vol. 14, K.J. Button, Ed., New York: Academic, 1985.

[45] H. Yoshinaga *et al.*, "A 94GHz-band low noise down converter," *IEEE MTT-S Int. Microwave Symp. Dig.*, Atlanta, GA, pp. 779-782, June 1993.

[46] M. W. Pospieszalski, *et al.*, "Millimeter-wave cryogenically-coolable amplifiers using AlInAs/GaInAs/InP HEMT's," *IEEE MTT-S Int. Microwave Symp. Dig.*, Atlanta, GA, pp. 515-518, June 1993.

[47] B. J. Clifton, G. D. Alley, R. A. Murphy, and I. H. Mroczkowski, "High-performance quasioptical GaAs monolithic mixer at 110GHz," *IEEE Trans. Electron Devices*, vol.28, pp. 135-157, Feb. 1981.

[48] D. B. Rutledge, D. P. Neikirk, and D. P. kasilingam, "Integrated circuit antennas", *Infrared and Millimeter Waves*, vol. 10, K. J. Button, Ed., New York: Academic, 1983.

[49] D. B. Rutledge and M. Muha, "Imaging antenna arrays," *IEEE Trans. Antenna Propagat.*, vol. 30, pp. 535-540, July 1982.

[50] G. M. Rebeiz, "Millimeter-Wave and Terahertz Integrated-Circuit Antennas," *IEEE-Proceedings*, vol. 80, pp. 1748-1770, Nov. 1992.

[51] G. M. Rebeiz, D. P. Kasilingam, P. A. Stimson, Y. Guo, and D. B. Rutledge, "Monolithic millimeter-wave two-dimensional horn imaging arrays," *IEEE Trans. Antennas Propag.*, vol. AP-28, Sept. 1990.

[52] S. S. Gearhart, *Millimeter- and Submillimeter-Wave Monolithic Integrated Antennas and Schottky Receivers*, Ph. D. dissertation, The University of Michigan, Ann Arbor, MI, 1993.

[53] G. M. Rebeiz *et al.*, "Submillimeter-wave antennas on thin membranes", *Int. J. Infrared Millimeter Waves*, vol. 8, pp 1249-1255, oct 1987.

[54] H. Ekstrom *et al.*, "348GHz endfire slotline antennas on thin dielectric membranes," *IEEE Microwave Guided Wave Lett.*, vol. 2, pp. 357-358, Sept. 1992.

[55] G. V. Eleftheriades and G. M. Rebeiz, "Design and analysis of quasi-integrated horn antennas for millimeter- and submillimeter-wave applications," To appear in the *IEEE Microwave Theory Tech.* journal, May 1993.

[56] K. S. Yngvensson *et al.*, "Endfire tapered slot antennas on dielctric substrates", *IEEE Trans. Antennas Propagat,*, vol 33, pp. 1392-1400, Dec. 1985.

[57] P.T. Parrish *et al.*, *SPIE Proc. vol 337, Millimeter-Wave Technology*, May1982.

[58] D. P. Kasilingam, *Topics in millimeter-wave imaging arrays*, Ph.D. dissertation, California Institute of Technology, Pasadena, CA, 1987.

[59] P. B. Katehi and N. G. Alexopoulos, "Substrate optimization for integrated circuit antennas," *IEEE Microwave Theory Tech.*, vol. 31, pp. 550-557, July 1983.

[60] D. P. Kasilingam and D. B. Rutledge, "Focusing properties of small lenses", *Int. J. Infrared and Millimeter Waves*, vol. 7, no. 10, pp. 1631-1647, 1986.

[61] R. C. Compton *et al.*, "Bow-tie antennas on a dielectric half-space: theory and experiment," *IEEE Trans. Antennas Propagat.*, vol. 35, pp. 622-631, June1987.

[62] G. Gauthier *et al.*, "A low-noise 86-90GHz uniplanar schottky-receiver," in *1993 MTT-S Int. Microwave Symp. Digest*, Atlanta, GA, pp. 325-328.

[63] A. Skalare *et al.*, "Double-dipole antenna SIS receivers at 100 and 400GHz," in *Proc. 3rd Int. Confer. on Space Terahertz Technology*, Ann Arbor, MI, Mar. 1992, pp. 222-233.

[64] B. K. Kormanyos *et al.*, "A planar wideband 80-200GHz subharmonic receiver," To appear in *IEEE-MTT Special Issue on Quasi-Optical Techniques*, Oct. 1993.

[65] S. S. Gearhart *et al.*, "A wide-band 760GHz planar integrated schottky receiver," *IEEE Microwave Guided Wave Lett.*, vol. 3, pp. 205-207, July 1993.

[66] M. N. Afsar, "Dielectric Measurements of Millimeter-Wave Materials," *IEEE Trans. Microwave Theory Tech.*, vol. 32, pp. 1598-1609, December 1984.

[67] C. C. Ling *et al.*, "Large Area Bolometers for THz power measurements," To appear in *IEEE Trans. Microwave Theory Tech.*, August 1993.

[68] K. E. Peterson, "Silicon as a mechanical material", *IEEE Proc.*, vol. 70, pp. 420-457, May 1982.

[69] K. E. Bean, "Anisotropic etching of silicon", *IEEE Trans. Electron devices*, vol. ED-25, pp.1185-1193, Oct. 1978.

[70] A. Reisman *et al.*, "The controlled etching of silicon in catalized ethylene-diamine-pyracatechol-water solutions," *J. Electrochemical Soc.*, vol. 126, pp. 1406-1425, 1979.

[71] Y. Guo, *Millimeter-Wave Integrated-Circuit Horn Antenna Imaging Arrays*, Ph.D. dissertation, California Institute of Technology, Pasadena, CA, 1991.

[72] C. A. Balanis, *Antennas: Theory and Design*, Harper and Row, New York, 1984.

[73] G. V. Eleftheriades, *Analysis and design of integrated-circuit horn antennas for millimeter and submillimeter-wave applications*, Ph.D. dissertation, The University of Michigan, Ann arbor, Michigan,1993.

[74] G. V. Eleftheriades, W. Y. Ali-Ahmad, L. P. Katehi and G. M. Rebeiz, "Millimeter-wave integrated horn antennas, Part I: Theory," *IEEE Trans. Antennas Propag.*, vol. AP-39, pp. 1575-1581, Nov. 1991.

[75] W. Y. Ali-Ahmad, G. V. Eleftheriades, L. P. Katehi and G. M. Rebeiz, "Millimeter-wave integrated horn antennas, Part II: Experiment," *IEEE Trans. Antennas Propag.*, vol. AP-39, pp. 1582-1561, Nov. 1991.

[76] Y. Guo, K. Lee, P. Stimson, K. A. Potter, and D. B. Rutledge, "Aperture efficiency of integrated-circuit horn antennas," *Microwave and Optical Tech. Lett.*, vol. 4, pp. 6-9, Jan. 1991.

[77] C. C. Ling, and G. M. Rebeiz, "A Wide-Band Monolithic Quasi-Optical Power Meter for Millimeter- and Submillimeter-Wave applications," *IEEE Trans. Microwave Theory Tech.*, vol. MTT-39, pp. 1257-1261, August 1991.

[78] W. Y. Ali-Ahmad and G. M. Rebeiz, "92GHz dual-polarized integrated horn antennas," *IEEE Trans. Antennas Propagat.*, vol. 39, pp. 820-825, July 1991.

[79] N. Amitay, V. Galindo and C. P. Wu, *Theory and Analysis of Phased-Array Antennas*, Wiley-Interscience, New York, 1972.

[80] G. V. Eleftheriades, W. Y. Ali-Ahmad, and Gabriel M. Rebeiz, "A 20dB quasi-integrated horn antenna," *IEEE Microwave and Guided Wave Lett.*, vol. 2, pp. 73-75, Feb. 1992.

[81] G. A. Ediss, "Dual-mode horns at millimeter- and submillimeter-wavelengths," *Proc. Inst. Elec. Eng.*, pt. H., vol. 132, pp. 215-218, June 1985.

[82] Selectilux HTR-3 Photosensitive Polyimide, Ciba-Geigy Corporation, 16033 South Twelfth Place, Phoenix, AZ 85044, Tel: (602) 460-1311.

[83] K. C. Gupta, R. Bahl, and I. J. Bahl, *Microstrip Lines and Slotlines,* Artech House, Inc., Norwood, MA, 1979.

[84] D. N. Held and A. R. Kerr, "Conversion loss and noise of microwave and millimeter-wave mixers: Part I-Theory," *IEEE Trans. Microwave Theory Tech,* vol. 26, pp. 49-54, Feb. 1978.

[85] D. N. Held and A. R. Kerr, "Conversion loss and noise of microwave and millimeter-wave mixers: Part II-Experiment," *IEEE Trans. Microwave Theory Tech,* vol. 26, pp. 55-61, Feb. 1978.

[86] P. H. Siegel, A. R. Kerr, "The Measured and Computed Performance of a 140-220 GHz Schottky Diode Mixer," *IEEE-Trans. Microwave Theory Tech.,* vol. MTT-32, pp. 1579-1590, Dec. 1984.

[87] R/T Duroid, Rogers Corporation, Chandler, AZ.

[88] P. A. Stimson *et al.*, "A planar quasi-optical SIS receiver," *IEEE-Trans. Microwave Theory Tech.,* vol. MTT-41, pp. 609-615, April 1993.

[89] R. E. DeBrecht, "Coplanar balun circuits for GaAs FET higher-power push-pull amplifiers," in *IEEE G-MTT Int. Microwave Symp. Digest,* pp. 309-311, 1973.

[90] D. M. Pozar, *Microwave Engineering,* Chapter 6, Addison-Wesley Publishing Company, Inc., 1990.

[91] K. McKinney, *Design and fabrication of a planar mixer diode for application at 100GHz,* M.Sc. thesis, The University of Virginia, Charlottesville, VA, 1986.

[92] R. T. Newman, Jr., *A planar diode submillimeter-wave mixer design and evaluation,* Ph. D. dissertation, The University of Virginia, Charlottesville, VA, 1991.

[93] W. L. Bishop, University of Virginia, private communication.

[94] S. Ramo, J. R. Whinnery, and T. VanDuzer, *Fields and Waves in Communication Electronics,* Second edition, John Wiley and Sons, Inc., New York, 1984.

[95] R. A. Chipman, *Transmission Lines,* Schaum's Outline Series, McGraw-Hill, Inc., 1968.

[96] M. Dye, *Design of a 75-110GHz MMIC mixer incorporating the surface channel Schottky-diode,* Masters Thesis, The University of Virginia, Charlottesville, VA, May 1990.

[97] J. A. Wells and N. J. Cronin, "Frequency dependant simulation of planar millimeter-wave mixer diodes," in *17th Int. Conf. on Infrared and Millimeter Waves Digest,* Pasadena, CA, 1992, pp. 214-215.

[98] A. R. Kerr, "A technique for determining the Local Oscillator Waveforms in a Microwave Mixer," *IEEE Trans. Microwave Theory Tech.*, vol. 23, pp. 828-830, Oct. 1975.

[99] *Diode Mixer Analysis Program*, provided by Prof. S. A. Maas, University of California, Los Angeles.

[100] P. F. Goldsmith, *Designing Quasioptical Systems*, Millitech Corp., South Deerfield, MA.

[101] N. R. Erickson, "A directional filter diplexer using optical techniques for millimeter to submillimeter wavelengths," *IEEE Trans. Microwave Theory Tech.*, vol. 25, pp. 865-866, Oct. 1977.

[102] J. M. Kenney, "The simultaneous measurement of gain and noise using only noise generators," *IEEE Trans. Microwave Theory Tech.*, vol. MTT-16, pp. 603-607, Sept. 1968.

[103] A. R. Kerr, "Low-noise, room temperature and cryogenic mixers for 80-120GHz," *IEEE Trans. Microwave Theory Tech.*, vol. MTT-23, pp.781-787, Oct. 1975.

[104] Emerson and Cuming Corporation, Canton, MA.

[105] P. H. Siegel, A. R. Kerr, and W. Hwang, *Topics in the optimization of millimeter-wave mixers*, NASA Technical Paper 2287, March1984.

[106] A. R. Kerr, "Shot-noise in resistive-diode mixers and the attenuator noise model," *IEEE Trans Microwave Theory Tech.*, vol. MTT-27, pp. 135-140, Feb. 1979.

[107] Cochise Instruments Inc., Hereford, Arizona.

[108] D. K. Cheng, *Field and Wave Electromagnetics*, Second edition, Addison-Wesley, 1989.

[109] M. N. Afsar, "Precision Millimeter-Wave Measurements of Complex Refractive Index, Complex Dielectric Permittivity, and Loss Tangent of Common Polymers," *IEEE Trans. Instrumentation Meas.*, vol. IM-36, pp. 530-536, June 1987.

[110] S. A. Maas, *Microwave Mixers*, second edition, Artech House, Norwood, MA, 1986.

[111] M. T. Faber and J. W. Archer, "Millimeter-Wave Shot-Noise Limited, Fixed-Tuned Mixer," *IEEE Microwave Theory Tech.*, vol. 33, pp. 1172-1178, Nov. 1985.

[112] R. J. Mattauch, T. W. Crowe, and W. L. Bishop, "Frequency and Noise limits of Schottky Barrier Mixer Diodes," *Microwave Journal*, pp. 101-116, March 1985.

[113] R. E. Collin, *Antennas and Radiowave Propagation,* McGraw-Hill, Inc., 1985.

[114] Type TH4213 Carcinotron, 300-365GHz, Thomson, CSF, Rutherford, NJ.

[115] E. Hecht, *Optics,* Second edition, Reading, MA: Addison-Wesley, 1987.

[116] Model PM103 power meter, Thomas Keating, Ltd., Billingshurst, West Sussex, England.

[117] R. S. Tahim, G. M. Hayashibara, and K. Chang, "Design and performance of W-band broad-band integrated circuit mixers," *IEEE Trans. Microwave Theory Tech.,* vol. MTT-31, pp. 277-283, March 1983.

[118] Millitech Corporation, *Millimeter and Submillimeter Components Catalog,* Southdeer-field, MA, 1989.

[119] A. R. Kerr, private communication.

[120] J. W. Archer, "All Solid-State Low Noise Receivers for 210-240 GHz," *IEEE Trans. Microwave Theory Tech.,* vol. MTT-30, pp. 1247-1252, August 1982.

[121] E. E. M. Woestenburg and L. Nieuwenhuis, "Low-noise 320-360GHz cryogenically cooled waveguide Schottky diode mixer," *Electron. Lett.,* vol. 22, no. 24, pp. 1305-1307, Nov. 1986.

[122] C. J. Alder *et al.,* "Microwave and millimeter-wave receivers with integral antenna," *Proc. Inst. Elec. Eng,* pt. H, vol. 138, pp. 253-257, June 1991.

[123] E. Garcia, B. R. Jacobson, and Q. HU, "Fabrication of high-quality superconductor-insulator-superconductor junctions on thin SiN membranes," *Appl. Phys. Lett.,* vol. 63, pp. 1002-1004, August 1993.

[124] C. C. Ling, *An Integrated 94GHz Monopulse Tracking Receiver,* Ph. D. dissertation, The University of Michigan, Ann Arbor, MI, 1993.

[125] H. Zebcker *et al.,* "Imaging radar polarimetry from wave synthesis," *J. of Geophysical Research,* vol. 92, No. B1, pp. 683-701, January 1987.

[126] F. T. Ulaby and C. Elachi, Editors, *Radar Polarimetry for Geoscience Applications,* Artech House, Norwood, MA, 1990.

[127] K. D. Stefan, N. Camilleri, and T. Itoh, "A quasi- optical polarization-duplexed balanced mixer for millimeter-wave applications," *IEEE Trans. Microwave Theory Tech.,* vol. MTT-31, pp. 164-170, Feb. 1983.

[128] C.Y. Chi and G. M. Rebeiz, "A quasi-optical amplifier," *Microwave Guided Wave Lett.,* vol. 3, pp. 164-166, June 1993.

[129] Y.-S. Kim and K. S. Yngvensson, "Characterization of tapered slot antenna feeds and feed arrays," *IEEE Trans. Antennas Propagat.,* vol. 38, pp. 1559-1564, Oct. 1990..

[130] W. Y. Ali-Ahmad and G. M. Rebeiz, "An 86-106GHz quasi-integrated low-noise Schottky receiver," *IEEE Trans. Microwave Theory Tech.*, vol. 41, pp. 558-564, April 1993.

[131] R. Moore, *Traveling-Wave Engineering*, McGraw-Hill, New York, 1960.

[132] G. Chin, "Optically pumped submillimeter laser receivers: Astrophysical observations and recent technical developments," *IEEE-Proceedings*, vol. 80, pp. 1788-1799, Nov. 1992.

[133] P. F. Goldsmith, "A quasioptical feed system for radioastronomical observations," *Bell Syst. tech. J.*, vol 56, pp. 1483-1501, 1977.

[134] P. F. Goldsmith, "Diffraction loss in dielectric-filled Fabry-Perot interferometers," *IEEE Trans. Microwave Theory Tech.*, vol. 30, pp. 820-823, May 1982.

[135] N. R. Erickson, "A new quasi-optical filter: the reflective polarizing interferometer," *Int. J. Infrared and Millimeter Waves*, vol. 8, no. 9, pp. 1015-1025, 1987.

[136] J. M. Payne and M. R. Wordeman, "Quasi-optical diplexer for millimeter wavelengths," *Rev. Sci. Instrum. 49*, pp. 1741-1743, 1978.

[137] R. Ulrich, "Far infrared properties of metallic mesh and its complementary strructure," *Infrared Physics*, vol. 7, pp. 37-55, 1967.

[138] N. Marcuvitz, *waveguide handbook*, chapter 5, Mc-Graw Hill, New York, 1951.

[139] F. T. Ulaby, R. K. Moore, and A. K. Fung, *Microwave Remote Sensing*, Vol. I, Artech House, Inc., Norwood, MA, 1986.

[140] D. H. Martin and E. Puplett, "Polarized interferometric spectrometry for the millimeter and submillimeter spectrum," *Infrared Physics*, Vol. 10, pp. 105-109, 1969.

[141] D. H. Martin, "Polarizing (Martin-Puplett) Interferometric Spectrometers for the Near- and Submillimeter Spectra," *Infrared and Millimeter Waves*, vol. 6, K. J. Button, Ed., New York, Academic 1982.

[142] P. F. Goldsmith, Cornell University, private communication.

[143] S. Weinreb and A. R. Kerr, "Cryogenic cooling of mixers for millimeter and centimeter wavelengths," *IEEE J. Solid-State Circuits*, vol. SC-8, pp. 58-63, Feb. 1973.

[144] M. T. Faber and J. W. Archer, "Computer-Aided Testing of Mixers between 90GHz and 350GHz," *IEEE Microwave Theory Tech.*, vol. 33, pp. 1138-1145, Nov. 1985.

[145] D. S. Saxon, *Elementary Quantum Mechanics,* Holden-Day, San Fransisco, CA, 1968.

[146] Shipley Company, Inc., Newton, MA.